INNOVATIVE MODULAR AND ARRAYED COIL SYSTEMS FOR ULTRAHIGH EFFICIENCY IN INDUCTIVE HEATING AND AUTOMATED METAL DETECTION

A DISSERTATION SUBMITTED TO

THE GRADUATE SCHOOL OF ENGINEERING AND SCIENCE

OF BILKENT UNIVERSITY

IN PARTIAL FULFILLMENT OF THE REQUIREMENTS FOR

THE DEGREE OF

DOCTOR OF PHILOSOPHY

IN

ELECTRICAL AND ELECTRONICS ENGINEERING

By

Veli Tayfun Kılıç

December 2016

INNOVATIVE MODULAR AND ARRAYED COIL SYSTEMS FOR ULTRAHIGH EFFICIENCY IN INDUCTIVE HEATING AND AUTOMATED METAL DETECTION

By Veli Tayfun Kılıç

December 2016

We certify that we have read this dissertation and that in our opinion it is fully adequate, in scope and in quality, as a dissertation for the degree of Doctor of Philosophy.

Hilmi Volkan Demir(Advisor)

Ayhan Altıntaş

Oğuz Gülseren

Hatice Özlem Aydın Çivi

Birsen Saka Tanatar

Approved for the Graduate School of Engineering and Science:

Ezhan Karaşan
Director of the Graduate School

ABSTRACT

INNOVATIVE MODULAR AND ARRAYED COIL SYSTEMS FOR ULTRAHIGH EFFICIENCY IN INDUCTIVE HEATING AND AUTOMATED METAL DETECTION

Veli Tayfun Kılıç
Ph.D. in Electrical and Electronics Engineering
Advisor: Hilmi Volkan Demir
December 2016

Induction systems have become increasingly more important and popular in our modern world and their application areas have widely expanded because of their high levels of safety and controllability. Today one important application of these induction systems is the inductive heating, which now finds use not only in conventional applications of point-source heating but also in new areas including all-surface heating with some degree of flexibility in localization. The efficiency of such emerging systems, especially in planar structures across an entire surface, however, has thus far been limited compared to conventional inductive heating. In this thesis, to address these problems, we show a new class of strongly coupled planar coils that enhance magnetic coupling in square lattice stacking by design and with phase difference application in operation. These coils can be tiled in two-dimensional arrays in a modular fashion or to cover an arbitrarily large continuous surface. In a proof-of-concept realization, we experimentally demonstrated that these proposed outer squircle-inner circular coils outperform the conventional coils of circular shape. Using square-arrayed coil architecture, here we also present all-surface induction systems achieving uniform and enhanced heating speed for all loading positions no matter what the misalignment of the heated vessel with respect to the coils is. In addition, to solve the problems of automatically detecting metals over the whole surface together with determining their exact positions, we introduce a new method that relies on simultaneous wireless measurement and tracking of inductance-resistance of the coils at multiple frequencies to identify those coupled with the metal targets to be detected in the system. While pinpointing the location of the targeted metals, the proposed technique also identifies their material types. For future ubiquitous all-surface systems, this approach allows for automated sensing of metal vessels and powering the loaded coils for the highest possible performance independent of the

specific location of each vessel with respect to coils. These findings indicate that the proposed innovative modular and arrayed coils enable, for the first time, full degree of flexibility in localized inductive heating with space-invariance in all-surface heating.

Keywords: Coils, coil arrays, electromagnetic induction, energy efficiency, inductive power transmission, inductive heating, all-surface heating, metal detection, wireless sensing.

ÖZET

ÇOK YÜKSEK VERİMLİLİKTE İNDÜKTİF ISITMA VE OTOMATİK METAL ALGILAMA İÇİN YENİLİKÇİ MODÜLER VE DİZİ BOBİN SİSTEMLERİ

Veli Tayfun Kılıç
Elektrik ve Elektronik Mühendisliği, Doktora
Tez Danışmanı: Hilmi Volkan Demir
Aralık 2016

Yüksek seviyede güvenlilik ve kontrol edilebilirlik özelliklerinden dolayı indüksiyon sistemlerin günümüz modern dünyasında önemi artmakta ve bu sistemler daha popüler hale gelirken kullanım alanları da genişlemektedir. Bu tür indüksiyon sistemlerin önemli uygulamalarından biri ısıtmadır. İndüktif ısıtmanın geleneksel ısıtmanın yanısıra lokal ısıtmadan bir derece daha esnek olan tüm yüzey gibi yeni uygulamaları vardır. Ancak, geliştirilmekte olan bu sistemlerin, özellikle de tüm yüzeyde kullanılan düzlemsel yapıların, verimlilikleri geleneksel indüktif ısıtıcılara göre oldukça kısıtlıdır. Bu tezde, bu sorunlara yönelik, aralarında kuplajı yüksek tutulan düzlemsel yapıda yeni bobin sınıfları tarafımızca gösterilmektedir. Bu bobinlerin aralarındaki manyetik etkileşme tasarımda karesel istiflenmeleri ve çalışma esnasında faz farkı uygulanması ile arttırılmaktadır. Bu bobinler iki boyutlu olarak modüler tarzda veya herhangi büyüklükteki ve kesintisiz bir yüzeyi kaplayacak şekilde döşenebilir. Kavramın ispatı gerçekleştirilirken, deneyler önerilen dış kısmı karesel-iç kısmı çembersel bobinlerin çember şeklindeki geleneksel bobinleri performansta geçtiğini gösterdi. Kare-dizi bobin mimarisi ile, bu tüm-yüzey indüksiyon sistemleri ile kap bobine göre tam hizalanmamış olsa dahi kabın bütün konumları için sabit ve yüksek hızda ısıtılması başarıldığı gösterildi. Buna ek olarak, metallerin yüzeyin tamamında otomatik olarak algılanması ve kesin konumunun belirlenmesi sorunlarının çözümüne yönelik, metallerle eşleşmiş bobinlerin algılanması ve tanımlanması için çoklu frekanslarda indüktans-rezistans değerlerinin eş zamanlı ve temassız ölçümüne dayanan yeni bir yöntem sunuldu. Önerilen bu yöntem ile metallerin konumları tam olarak saptanırken, aynı zamanda malzeme tipleri de tanımlanabilmektedir. Gelecekte her yerde kullanılabilecek tüm-yüzey sistemler için bu yaklaşım metal kapların otomatik olarak algılanmasını ve yüklü bobinlerin her bir kabın bobine göre konumundan bağımsız olarak en yüksek performansla

sürülmesini sağlayacaktır. Bulgularımız göstermektedir ki, önerilen bu yenilikçi modüler ve dizi bobinler, ilk defa olarak, tüm-yüzey ısıtmada konumdan bağımsız olarak tam bir esneklikle indüktif ısıtmaya olanak sağlamaktadır.

Anahtar sözcükler: Bobinler, bobin dizileri, elektromanyetik indüksiyon, enerji verimliliği, indüktif güç iletimi, indüktif ısıtma, tüm yüzey ısıtma, metal algılama, kablosuz algı.

Acknowledgement

I would like to express my deepest gratitude to my supervisor Prof. Dr. Hilmi Volkan Demir for his guidance and support throughout my Ph.D. study. He was always helpful and kind to me and I am indebted to him for allowing time whenever I need and listening my problems, even if he was very busy.

I would like to thank Prof. Dr. Ayhan Altıntaş and Prof. Dr. Oğuz Gülseren for their contributions and guidance as my thesis monitoring committee members during my research efforts and for giving very useful comments during our meetings. I would also like to thank Professors Birsen Saka Tanatar and Hatice Özlem Aydın Çivi for serving on my thesis committee.

I would like to thank former and recent members of Demir Research Group. I would especially like to thank Emre Ünal, Özgün Akyüz, Birsen Bilgili, Sayim Gökyar, Akbar Alipour, Kıvanç Güngör, Talha Erdem, Burak Güzeltürk, Yusuf Kaleştemur, Sedat Nizamoğlu, Evren Mutlugün, Emre Sarı, Rohat Melik, Nihan Koşku Perkgöz, Pedro L. Hernandez, Ozan Yerli, Onur Akın, Mustafa Akın Sefunç and Can Uran for their friendships and collaborations.

I would like to specially thank Emre Ünal for his assistance during my whole Ph.D. study. He is a very hardworking engineer everyone will definitely want to work with. I am very happy to know and work with him. I would like to thank Berkay Bozok for his assistance in part of our study. It was a pleasure to work with him.

I would also like to thank Arçelik Company and Industry Theses Program SANTEZ 1463-STZ-2012-2 for their supports. I am very happy to work with Arçelik R/D Department and Dishwasher Division. I extend my special thanks to Namık Yılmaz and Erdal Gönendik for their assistances in early and later stages of my Ph.D. study.

I cannot pass without mentioning some of my colleagues' names. I am really

grateful to my office friends: Ahmet Dündar Sezer and Serkan Sarıtaş for letting me use their office, our wonderful late night studies and beautiful friendship and also to my friends from the department: İsmail Uyanık, Ali Nail İnal, Deniz Kerimoğlu, Ali Alp Akyol, Hasan Hamzaçebi, and Burak Alptuğ Yılmaz for their supports and friendships.

I would like to thank my former company MİKES and my current employee TÜBİTAK-İLTAREN for their supports. I express my gratitudes to my former and current colleagues, especially my friends in RF/Microwave Design Group at MİKES and in RF Systems Group at İLTAREN, for always being nice to me.

I would also like to thank Bilkent University EEE Department and especially Professor İhsan Doğramacı, the Founder of our University (I pray for him) for providing such good circumstances during both my undergraduate and graduate study.

I would like to acknowledge TÜBİTAK (The Scientific and Technological Research Council of Turkey) - BİDEB for their financial support during my Ph.D. study.

I am very proud to dedicate my thesis to my mother Necla Kılıç, my father Samet Kılıç and my brother İsmail Kılıç for their endless love and endless support in my whole life. The words are not enough to describe my love and acknowledgement to them.

I am very grateful to my love for her support and patiently being on my side during my difficult times. I am very happy to know her.

Contents

List of Figures

List of Tables

Chapter 1

Introduction

This thesis introduces wireless induction systems for high efficiency in inductive heating. In the thesis, new coil and system designs have been proposed and investigated for efficiency enhancement using planar architectures in induction systems.

Electricity is the most commonly used power source in today's world. It has been utilized widely for almost all of the areas in our lives, such as in street lightning, industrial production, communication systems, and recently cars. Conventionally, electrical power is distributed via cables. However, with the developments in technology, the necessity for wireless devices and applications increases. Cellular phone, which is now an indispensable part of our modern daily life, is an example of wireless device. Wireless induction system is one of the ways to transfer and distribute energy without using wire.

Consumer electronics is another application area of electricity. Because it is a clean source, electricity is being used in household applications increasingly more frequently. Heating and cooking systems can be listed among these applications. Although all of them use electricity as a power source, different types of electrical heating exist, including resistive heating and inductive heating [6]. Resistive heating is the traditional electrical heating process in which the heat is obtained

via current flow through a material that has substantial resistance. This is the most common and simple technique. However, it is neither safe nor efficient. On the other hand, recently inductive heating systems have become popular especially in European and East Asian countries, where other power sources such as gas are more limited. This is because of the advantages of inductive heating systems that include safety, cleanliness, quick warming, high efficiency and controllability [6]-[7]. For comparison purposes, efficiencies of some cooking methods are given in Table 1.1.

Table 1.1: Efficiency of cooking methods [5].

Method	Efficiency
Induction	90%
Halogen	58%
Electric (Resistive)	47%
Gas	40%

The advantages of inductive heating systems stem from the fact that heating is produced directly on the vessel floor [7]. In induction cookers, a coil is powered up and the generated magnetic flux is coupled to a vessel. Related with this alternating magnetic flux, current is produced on the vessel floor and this in turn leads to the vessel's heating. Unlike conventional resistive heating systems, in inductive heating systems the heat is not transferred but the magnetic flux is. Therefore, the heat dissipation and the resulting energy loss is low in induction systems. This is the reason why inductive heating hobs are more efficient than traditional resistive heating systems. In addition, in an induction hob, the vessel starts to heat up when the coil is powered up. There is no need to wait the oven's heating up. Thus, it is true to state in general that induction systems have the property of quick warming. Moreover, inductive heating systems are safe because only the vessel heats up and, when it is removed, there will be no heating even if the oven is on. Also, it is nonhazardous to human body due to the human body's magnetic properties.

Despite all of the advantages of inductive heating systems, there are some

challenges that are waiting to be addressed. Firstly, conventional inductive heating hobs do not operate as a whole plane. For efficient heating, vessel should be placed on specific locations that are close to the coil's top. In addition, conventional inductive heating systems do not efficiently heat vessels made of non-magnetic materials, such as aluminum and copper [5]. Furthermore, due to high switching frequency it is not possible to avoid switching losses in the power stage of inductive heating systems. We believe that efficiency of induction systems can be enhanced by new designs of coil and system architectures.

Although there have been some previous reports related to these problems, they do not completely overcome the aforementioned issues. In this thesis, we have been interested in these problems. To heat vessels efficiently all over the hob's surface, a new class of small size coils with outer squircle-inner circular shape have been designed. This unique coil architecture enables high interaction and high efficiency in all-surface inductive heating together with easy manufacturing. With experiments and simulations, using two side-by-side placed coils and a plate, it was observed that the system's efficiency can be increased overall by more than 30% by using the proposed outer squircle-inner circular coils instead of conventional circular coils and by applying phase difference to the coils. We have three patent applications [8]-[10] and one paper publication, which appeared in IEEE Transactions on Industrial Electronics, [11] related to these studies. Also, by going one step further, efficiency enhancement of a system with the proposed outer squircle-inner circular coils have been shown for four coils tangentially placed in a two-dimensional (2D) square lattice.

In addition, to model an all-surface induction hob we placed nine of manufactured coils having outer squircle-inner circular shape in a 2D 3×3 square lattice. System heating speed and efficiency were measured for various plate positions. Independent from the plate position, almost equal heating speeds were measured for the similar dissipated energies in the system. Also, with three-dimensional (3D) electromagnetic (EM) simulations, these results were verified. Therefore, the inductive system made of the proposed outer squircle-inner circular coils has been proved to be useful for quick and efficient heating in total active surface induction hobs. Related to this study we prepared another manuscript that is in

submission [12].

Another problem that we studied in this thesis is metal detection in inductive heating systems. This is a challenge especially for all-surface induction heaters. In all-surface induction hobs, for efficient and safe heating, vessel size and position should be identified together with its material. It is necessary to power up only the corresponding coils underneath the vessel. To address these requirements, we proposed and demonstrated a simple and robust solution that is based on measuring the inductance-resistance of coils in an induction heater. With experiments we investigated the inductance and resistance of a coil loaded by vessels made of different materials and having various positions at different frequencies. It was shown that, in a coupled system, partial area of the coil covered by the vessel can be accurately determined and the vessel material can be uniquely identified from the variations in the inductance and the resistance of the coil, i.e., from the variations in amplitude and angle of the coil's impedance. Part of our study has been published in Sensors Journal [13] and part of it has been submitted to AIP Advances journal [14].

The rest of the thesis is organized as follows. In the next chapter, we first briefly explain the theory. Inductive heating and wireless energy transfer of induction systems are described. In the third chapter our study on newly designed small size coils with outer squircle-inner circular shape is presented. Heating experiments of two side-by-side placed outer squircle-inner circular coils and conventional circular coils are described. The measurement and simulation results are given in detail. In addition, our further measurements with four of the coils are reported. In the fourth chapter, our additional study of all-surface induction hobs including heating experiments and simulations of array of the designed outer squircle-inner circular coils aligned in a 2D square lattice is described. Measurement and simulation results are compared for the loading plate's various positions. In the fifth chapter, our works on metal detection are explained. A method based on measuring inductance and resistance values of a loaded coil at different frequencies is proposed to uniquely identify vessel's material while determining its size, shape and position on an all-surface induction hob. Experiments and simulations conducted with vessels made of different materials and located at different positions

above a designed outer squircle-inner circular and conventional circular coil are given. Finally, in the sixth chapter, conclusions of this thesis are provided and explained one by one.

Chapter 2

Theory, Modeling and Methodology

The theory behind wireless induction systems relies on the Faraday's law of induction, which is one of the Maxwell's equations. In 1831, in his experiments Michael Faraday observed that in a circuit current flow is generated by changing the external magnetic flux across the circuit [15]. Faraday's law of induction is one of the fundamental principles in electromagnetics in terms of explaining the relationship between the electric and magnetic fields. It is applicable at every point in space and its time-domain expression is given by

$$\nabla \times \vec{E}(\vec{r},t) = -\frac{\partial \vec{B}(\vec{r},t)}{\partial t} \tag{2.1}$$

Here $\vec{E}(\vec{r},t)$ and $\vec{B}(\vec{r},t)$ represent the electric field intensity (V/m) and the magnetic flux density ($Tesla$ or Wb/m^2), respectively. This law basically indicates that a time-varying magnetic field creates a specially varying electric field and vice versa. If we take integral of equation (2.1) over a surface S, then the following is obtained

$$\int_S [\nabla \times \vec{E}(\vec{r},t)] \cdot d\vec{S} = \int_S [-\frac{\partial \vec{B}(\vec{r},t)}{\partial t}] \cdot d\vec{S} \tag{2.2}$$

and, by Stoke's theorem, this can be expressed as

$$\oint_C \vec{E}(\vec{r},t) \cdot d\vec{l} = \int_S [-\frac{\partial \vec{B}(\vec{r},t)}{\partial t}] \cdot d\vec{S} \tag{2.3}$$

Here, C is the closed contour that bounds the surface S and its direction is found by the right hand rule. Note that for a time-changing magnetic field the right hand side of equation (2.3) is nonzero. Thus, the closed loop integral of electric field (left hand side of the equation) is also nonzero. This is different from the electrostatic case.

In electromagnetics, there are two ways of creating electric ($\vec{E}$) field. The first one is the time-varying magnetic field, which creates a looping electric field. Charge also creates electric field, but not looping. On the other hand, in electrostatic and magnetostatic cases, $\frac{\partial}{\partial t} = 0$. Therefore, in the static cases, only charges can generate electric field and its integral over a closed curve is zero. For stationary circuits, equation (2.3) can be arranged into

$$\oint_C \vec{E}(\vec{r},t) \cdot d\vec{l} = -\frac{d}{dt} \int_S \vec{B}(\vec{r},t) \cdot d\vec{S} \tag{2.4}$$

Here, if we define

$V = \oint_C \vec{E}(\vec{r},t) \cdot d\vec{l}$ to be emf (electromotive force) induced on the contour C (in Volts) and
$\Phi = \int_S \vec{B}(\vec{r},t) \cdot d\vec{S}$ to be total magnetic flux passing through surface S (in Weber),

then equation (2.4) turns into

$$V = -\frac{d\Phi}{dt} \tag{2.5}$$

Equation (2.5) is another form of the Faraday's law of electromagnetic induction and it states that the electromotive force induced on a closed and stationary circuit equals to the total magnetic flux change rate through that circuit in amplitude. Also, minus sign in the equation indicates that the produced emf opposes the change of the magnetic flux, which is known as Lenz's law [15]. If the circuit is a wound coil of wire, composed of N identical loops, then each loop is exposed to the same magnetic flux Φ and the resulting total induced voltage is

$$V = -N\frac{d\Phi}{dt} \tag{2.6}$$

Some applications of the electromagnetic induction include inductors, induction motors, transformers, inductive heating systems and wireless power transmission.

Since it is a well-known device and has a similar operation principle with inductive heating and energy transfer systems, investigating a transformer is a good idea. Simple structure of a transformer and its input-output relationships are given in Figure 2.1.

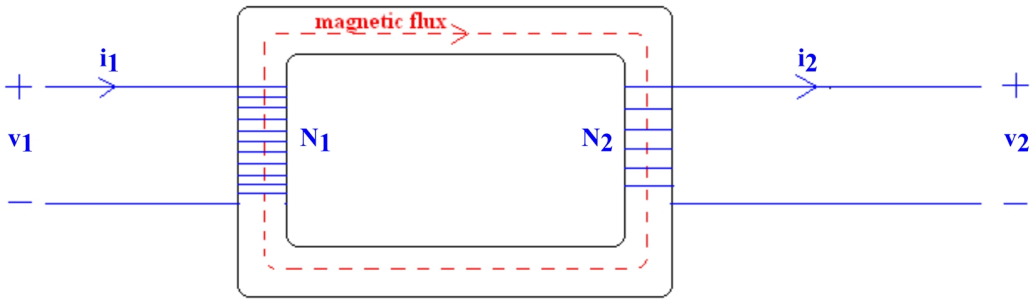

Figure 2.1: Simple structure of a transformer together with the input-output parameters.

A transformer can be defined as a device that transforms current, voltage and impedance from one side to the other [15]. It operates with alternating currents (a.c.). Relations between its primary and the secondary sides illustrated in Figure 2.1 can be defined as

$$N_1 i_1 - N_2 i_2 = R\Phi \tag{2.7}$$

where R is the reluctance of the magnetic circuit and Φ is the magnetic flux flowing in the ferromagnetic core, which is represented with dashed red curve in the figure. Reluctance of a transformer depends on its geometry and core material. In an ideal transformer, it is assumed that permeability of the core material is infinite and all the flux lies inside the core. Therefore, for an ideal transformer, $R = 0$ is assumed and equation (2.7) simply becomes

$$N_1 i_1 - N_2 i_2 = 0 \tag{2.8}$$

Thus,

$$\frac{i_1}{i_2} = \frac{N_2}{N_1} \tag{2.9}$$

Also, we have the following relations:

$$\frac{v_1}{v_2} = \frac{N_1 \frac{d\Phi}{dt}}{N_2 \frac{d\Phi}{dt}} \rightarrow \frac{v_1}{v_2} = \frac{N_1}{N_2} \tag{2.10}$$

$$Z_{1eff} = \frac{v_1}{i_1} = \frac{(\frac{N_1}{N_2})v_2}{(\frac{N_2}{N_1})i_2} = (\frac{N_1}{N_2})^2 \frac{v_2}{i_2} = (\frac{N_1}{N_2})^2 Z_L \tag{2.11}$$

where Z_{1eff} and Z_L are the effective load impedance seen by the primary side and the load impedance at the secondary side, respectively.

In a transformer, current in the primary coil i_1 generates a magnetic flux, whose direction is found by the right hand rule. This magnetic flux is captured by and flows in the core material. In the second coil to oppose this magnetic flux an inductive current i_2 is generated. As can be seen from Figure 2.1, currents i_1 and i_2 are in the same direction because of opposite magnetic fluxes. This phenomenon is in accordance with the Lenz's law.

Operation principle of transformers is very similar to that of inductive heating and power transfer systems. However, in these systems instead of the core material magnetic flux generated by a transmitter is coupled to a receiver through air. Also, in inductive heating systems there is no secondary coil. Magnetic flux is captured by and inductive current is produced on a ferromagnetic metal material (a pot or a vessel).

As indicated in Faraday's law of induction, an electromotive force (emf) is induced as a result of the magnetic flux change. When this induced emf results in current flow in conducting material itself (due to finite conductivity of the material), then this is referred to as eddy current. Eddy currents are a special form of the inductive currents that oppose the magnetic flux change and are normal to magnetic flux but occur in conducting core material. Inductive heating systems use these eddy currents to heat up vessels, which thus are critical in inductive heating systems. On the other hand, in transformers and other applications, eddy currents cause power loss. To decrease eddy current power losses, in transformers laminated cores are used.

In the inductive heating systems, due to finite conductivity (nonzero resistivity) of its material, the induced eddy current on the bottom surface of a vessel encounters a resistance and produces heat energy. This heat dissipation is simply given by

$$P = i^2 R \tag{2.12}$$

where i is the eddy current and R is the effective resistance of the pot.

In direct current (d.c.) case, resistance of a material depends on its resistivity and its geometrical parameters. Current in the material is assumed to flow uniformly, i.e., the current density is constant, across a cross-section that is normal to the current flow. On the other hand, in alternating current (a.c.) case, resistance of a material depends on its resistivity, its geometrical parameters and also on its skin depth. Current density in the conductor material is then not constant. An alternating electric current in a conductor has a tendency to flow in regions close to walls of the conductor. This tendency is called skin effect. According to skin effect, an alternating current flows mostly in the regions close to skin of the conductor. Current density is maximum near the surface and decreases exponentially with the depth (towards inside from the conductor surface). This relation is formulated in equation (2.13)

$$\vec{J} = \vec{J}_s e^{\frac{-d}{\delta}} \tag{2.13}$$

where $\vec{J}$ is the current density at a depth d away from the conductor surface, $\vec{J}_s$ is the current density on the conductor surface, i.e., $\vec{J}$ at $d = 0$, and δ is the skin depth. As can be seen in equation (2.13), the skin depth is the depth at which the current density drops to $1/e$ of its maximum value, which is found on the conductor's surface [6, 16]. General expression of the skin depth for an electrically conducting material is given by

$$\delta = \sqrt{\frac{2\rho}{\omega}} \tag{2.14}$$

where ρ is the resistivity of the conductor, ω is the angular frequency and μ is the permeability of the conductor. Since effective cross-section of the conductor, across which the current is assumed to flow, decreases with the increasing skin effect, the skin effect results in the effective resistance of the conductor to be

increased. Therefore, the effective resistance and thus the heat energy is inversely proportional to the skin depth. This means that as the skin depth decreases the effective resistance and the heat energy increase [6]. Resultantly, at higher frequencies, the produced heat energy in the pot is larger because of thin skin depth. This is the reason of why researchers want to work at higher frequencies in inductive heating systems but there exist some drawbacks of operating at high frequencies such as increased switching loss.

Skin effect is useful for heating up a vessel. On the other hand, it causes unwanted energy losses in coils. To mitigate skin effect and to decrease losses in a coil, Litz wire is being used [17, 18]. Litz wire consists of many insulated parallel thin strands. Magnetic flux exposes uniformly to each thin wire strands and so currents with almost equal magnitudes are generated and flow on all of the strands. Therefore, skin effect and heat loss are eliminated. Since skin depth decreases with frequency, in high frequency applications litz wires consisting of more and thinner strands are preferred.

2.1 Wireless Inductive Heating Systems

Because of their advantages over conventional heating systems, inductive heating systems are becoming more popular in today's world. Details about the problems observed in inductive heating systems, literature works and our idea are described in the following pages.

2.1.1 Architecture and Working Principle

As an example, photograph of an induction hob manufactured by Arcelik Company is illustrated in Figure 2.2.

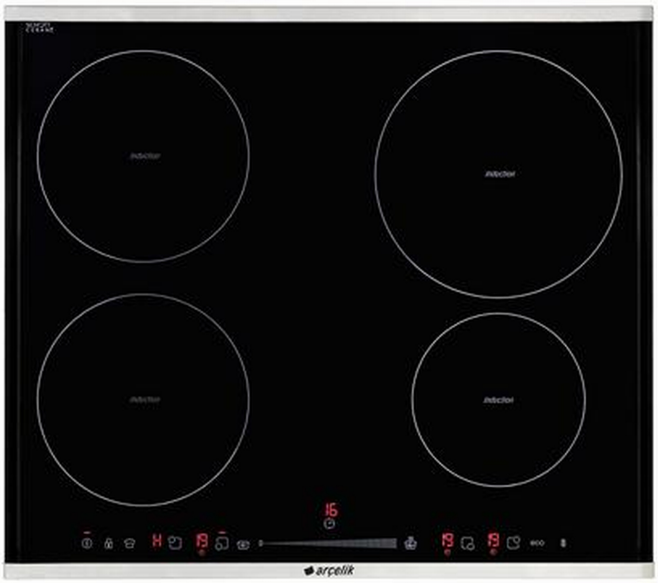

Figure 2.2: Photograph of an induction hob manufactured by Arcelik Company [1].

Wireless inductive heating systems consist of three main parts that are power source circuit, control hardware circuit and heating circuit [19]. Power circuits generate high frequency power signals that power up the coils. Due to high operation frequency, switching power losses become larger. To decrease these losses newly developed inverter topologies have been proposed [20, 21]. On the other hand, control circuits decide which coils to be activated. Control circuits regulate connections between the coils and the power supply circuit.

In our study, we focus on the heating circuit of an induction hob. Heating circuit is responsible to heat up the vessel. Its architecture is simply illustrated in Figure 2.3.

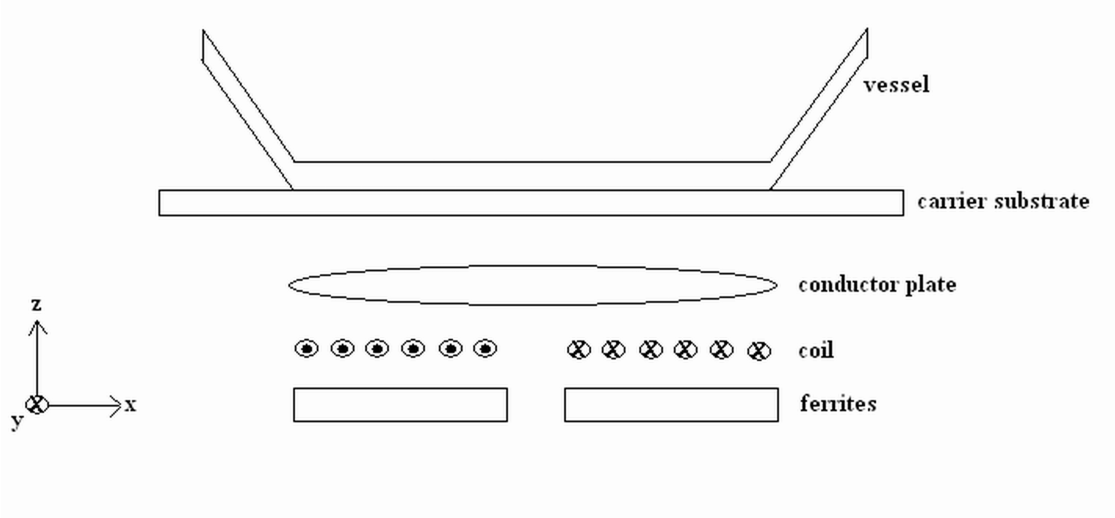

Figure 2.3: Simple architecture of the heating circuit in an induction hob.

As it is seen in the figure, heating circuit of an induction hob consists of four parts, which are coils, ferrites, conductor plates, and a carrier substrate. In the figure, at the top, vessel is illustrated, too, but it is not a part of the cooker. Parts of the heating circuit are described briefly in the following paragraphs one by one. Subsequently, working principle of the heating circuit is explained.

Coil: Coils are placed between the ferrites and the conductor plate. They are driven by the power source circuit with an alternating current and they generate alternating magnetic fields, which heat up the vessel. Via their produced fields, coils couple to other elements, i.e., to ferrites, to conductor plate and to vessel [22]. Heating coils (both in coupled and uncoupled systems) are simply represented with a series R-L circuit, i.e., $Z_{coil}(\omega) = R_{coil} + j\omega L_{coil}$ [20, 21]. Here, R_{coil} and L_{coil} are equivalent resistance and equivalent inductance of the coil, respectively, and they can be written as $R_{coil} = \Delta R + R_0$ and $L_{coil} = \Delta L + L_0$ where ΔR and R_0 represent equivalent resistance enhancements due to power transferred to the load and losses in the wire, respectively. Also, L_0 and ΔL represent self-inductance of the coil and contribution of the load to the equivalent inductance, respectively [7, 23, 24]. In the coil three types of loss are observed, which are conduction (ohmic) loss, skin effect loss and proximity effect loss. However, in

high frequencies losses due to skin effect and proximity effect dominate the conduction loss. To mitigate skin effect and proximity effect losses multi-stranded Litz wires are used in coils [17, 23, 25].

Vessel: Vessel is placed above the carrier substrate. Alternating fields generated by the coil reach and couple to the vessel. Resultantly, eddy currents are induced on the vessel. Via these induced eddy currents, the vessel is heated up. Vessels made of ferromagnetic materials ($\mu_r \gg 1$) such as iron, are the most proper materials to be used in inductive heating systems [5]. In addition, vessels made of a material with high magnetic permeability and high electrical conductivity such as steel, are also good examples to be used for inductive heating appliances [2]. On the other hand, it is not easy to inductively heat the vessels made of a material with low magnetic permeability and high electrical conductivity such as aluminum (Al) and copper (Cu) [16, 2]. To heat up these vessels, coils should be driven with large currents. However, this causes buoyancy of the vessel as a result of repulsion force between the coil and the vessel [3]. In all the cases, to heat up a vessel, its thickness should be larger than the permeable depth of the vessel material at operation frequency.

Ferrites: Ferrites are placed below the coils. They consist of ferromagnetic materials that have high magnetic permeability and low electrical conductivity [25]. Ferrites improve system heating efficiency by redirecting and focusing magnetic fields below the coils onto the vessel [3]. This can be explained with the image theory, where to estimate fields above the ferrites, the ferrite plane that can be thought as a perfect magnetic conductor-PMC, is replaced with imaginary currents [26, 27].

Carrier substrate: Carrier substrate is located below the vessel. Indeed, in an induction hob the top surface that is seen, is the carrier substrate. It is generally made of materials that are poor in heat conduction such as glass, ceramic or glass-ceramic [28]. Therefore, carrier substrate makes surface of the hob nonhazardous while carrying the vessel.

Conductor plate: As we explained previously, it is not easy to heat a vessel made of a material with low magnetic permeability and high electrical conductivity such as aluminum and copper. Large currents are required to heat up these kinds of vessels. However, larger currents generate magnetic flux with higher density and this results in large repulsion force between the vessel and the coil. Resultantly, buoyancy is exerted on the vessel. To heat up vessels made of nonmagnetic and highly conductive materials with decreased buoyancy, conductor plate is placed between the coil and the vessel. Conductor plates are generally made of aluminum since aluminum has low magnetic permeability and high conductivity [2, 3]. Because of its low magnetic permeability, magnetic flux generated by the coil is unlikely absorbed by the conductor plate and due to its high conductivity induced current on the conductor plate does not encounter strong resistance, which helps for increasing the efficiency and decreasing the buoyancy. Conductor plate changes magnetic field distribution in the system. Therefore, induced current distribution on the vessel changes, too. These changes are mainly because of the eddy currents induced on the conductor plate. Resultantly, coupling between the vessel and the coil, thus heating efficiency of the system, increases. In other words, with usage of a conductor plate, vessels made of materials having low magnetic permeability and high conductivity can be heated up with low magnitude currents, which results in buoyancy decrease exerted on the vessel [2, 3, 4]. Conductor plate should be thicker than the permeable (skin) depth of the material that it is made of, for magnetic fields do not pass through it. However, high induced current creates a heating problem in conductor plates. To solve this issue, conductor plates with different architectures were reported in literature. We investigated them later in the chapter.

Working principle of the heating hob illustrated in Figure 2.3 can be described briefly as follows. The coil is powered up with an alternating current that is supplied by the power circuit. This alternating current flows in the coil windings and based on the right hand rule a magnetic flux is produced. In Figure 2.3 we illustrate the current flow in the coil. It is in the counterclockwise direction. For clarity, current directions are illustrated in Figure 2.4, too. The generated flux by the coil couples to the ferrites, to the conductor plate and to the vessel.

However, flux in below side is redirected upwards by the ferrites, which can be explained with the image theory. Resultantly, total upward directed magnetic flux is coupled to the conductor plate and to the vessel. Due to this coupled magnetic flux, induction currents are generated both on the conductor plate and on the vessel. These induced eddy currents are in the opposite direction with the coil currents and they oppose the magnetic flux generated by the coil. For instance, in our case coil current is assumed to be in the clockwise direction, which is represented in Figure 2.4. Due to finite conductivity of the materials, heat is produced both in the conductor plate and in the vessel. Here, it is important to note that the magnetic field and the eddy current distributions on the bottom surface of the vessel depend on the induced eddy currents on the conductor plate. In other words, the eddy current distribution on the vessel is different in systems with and without a conductor plate. The heat generated on the conductor plate is unwanted and it can be hazardous for the system. On the other hand, the heat generated on the vessel is the main task in inductive heating systems, which yields cooking a food in the vessel.

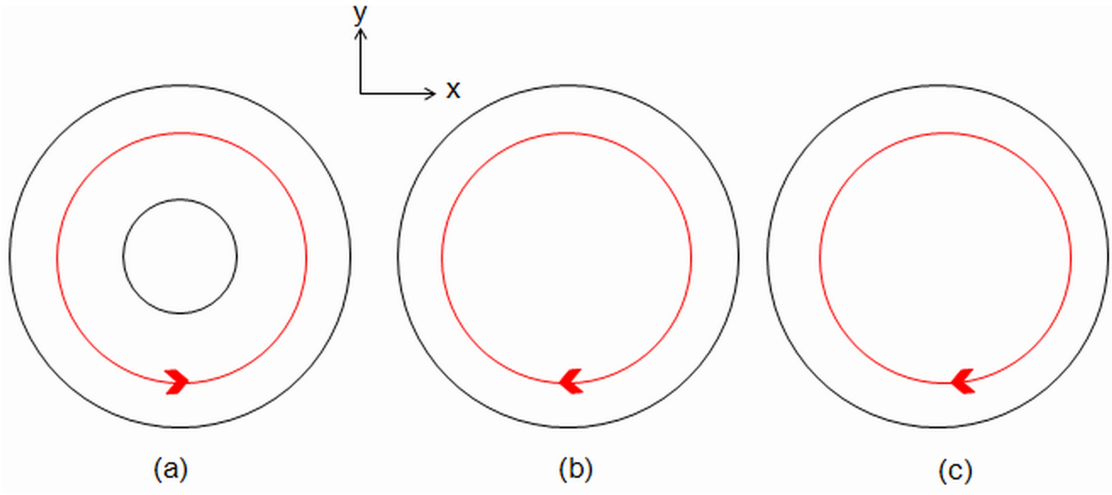

Figure 2.4: Current directions (a) on the coil, (b) on the conductor plate, and (c) on the vessel.

2.1.2 Literature Review

In literature there are lots of previous reports about inductive heating systems. Some of these studies focus on developing power circuit and switching unit. Half-bridge inverter is one of the recent topics proposed for reducing losses in power circuit of an induction hob [20, 21, 29]. Also, in some studies by sensing a vessel and adjusting frequency of the supply circuit, system efficiency enhancement is intended [23, 30, 31]. In these studies a vessel is sensed and based on its material, i.e., being magnetic or nonmagnetic, and its distance to the coil, operating frequency of the system is adjusted.

Moreover, vessel design is a topic in some other studies [16, 32]. In these studies vessels with floor consists of multiple layers have been investigated. These layers are made by a magnetic material such as iron and by a nonmagnetic but highly conductive material such as aluminum. Magnetic flux produced by a coil is captured in the magnetic material layer and eddy currents are induced there. The resulted heat is transferred to the conductive layer and uniformly distributed over the vessel. Therefore, with such designs, efficient and uniform heating of the vessel is aimed together with the vessel's being light and resistive to rusting.

Furthermore, coil is one of the topics interested by researchers and engineers. Different coil architectures have been investigated starting from the early 20^{th} century (such as Tesla's coil). In recent years, with the development of inductive heating systems, coils attract much more attention. Impedance of coils [33, 34] and coupling between them [25] have been studied both theoretically and experimentally. Also, loss mechanisms such as proximity and skin effects have been analyzed in literature [17, 18, 35, 36].

In addition, in literature there are reported works that investigate the ferrite plane [26, 27]. They explain usage of the ferrite plane in heating hobs and demonstrate that heating efficiency can considerably be enhanced by using ferrites.

Finally, besides all these works, there exist published documents in literature that are about induction heaters with a conductor plate [2, 3, 4]. These patents

are useful in terms of defining properties and missions of a conductor plate together with investigating different shaped conductor plates. As we explained in the previous section, heating of a vessel made of nonmagnetic materials with high conductivity such as aluminum and copper, is not easy in an induction hob. To heat such vessel large input power is required but this may cause buoyancy problem. To increase heating efficiency and decrease buoyancy exerted on the vessel, a conductor plate is placed between the coil and the vessel. In these systems, buoyancy decrease is proportional to the conductor plate area that intersects the magnetic flux produced by the coil. However, due to the induced eddy currents the conductor plate heats up, too. Therefore, there is a trade-off between buoyancy decrease and the conductor plate's heating. Also, vessel heating efficiency in the system is another concern that changes with the conductor plate. To this end, different shaped conductor plates were examined in literature. Architectures of some of these conductor plates are illustrated in Figure 2.5.

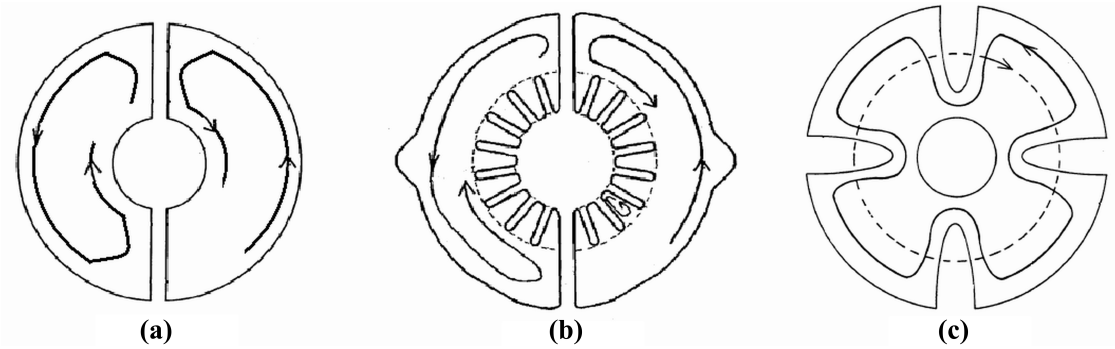

Figure 2.5: Some of the conductor plate examples proposed and exist in literature. Here, the curved lines with arrows indicate induced eddy currents on the conductor plate and the dashed curve in (c) represent current on the inductor coil [2, 3, 4].

In these architectures clarities divide the plate into pieces and they prevent continuous circulating current flow. In addition, comb shaped slots in inner and outer circumferences make the current flow path to be longer and prevent current flow. Therefore, comb shaped slots prevent too much heating of the conductor plate without causing an excessive amount of reduction in efficiency enhancement,

i.e., buoyancy decrease, in the system.

2.2 Numerical Electromagnetic Simulation Tool - CST

In our induction system analysis we have used software simulation tool CST (Computer Simulation Technology). CST is a simulation tool that enables solutions for three-dimensional (3D) electromagnetic (EM) problems such as design, analysis and modeling of electromagnetic components, devices, media, etc., in a wide range of operational frequency. CST Studio involves various modules to solve different types of electromagnetic problems. For instance, CST MWS (Microwave Studio) is a tool offered and usually used for high frequency 3D EM simulations. Another module that is used for solution of the static and low frequency problems is CST EM Studio. It is useful for the applications of coils and magnet designs, sensors, electromechanical components, motors-generators-transformers, inductive heating and wireless power transmission systems, etc. With its user interface and operations via script files CST is an easy tool to use.

In our simulations we used CST EM Studio. In Figure 2.6, a view of CST EM Studio user interface is represented.

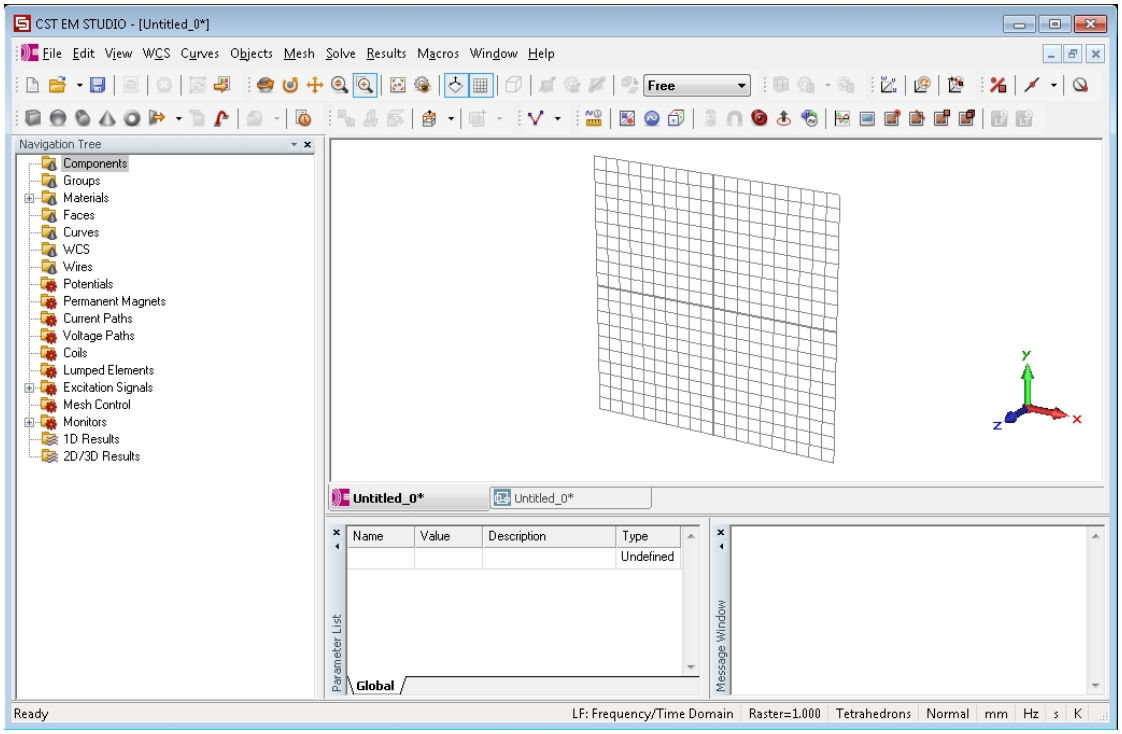

Figure 2.6: User interface of CST EM Studio.

CST Studio basically uses FIT (Finite Integration Technique) to solve EM problems. In FIT, Maxwell equations in their integral forms are discretized to be solved in computers. As always, solutions satisfy the boundary conditions. Similar to other solution techniques such as FDTD and FEM, in FIT, domains are divided into spatial grids and discretized equations are solved iteratively in these grids. These iterative computations continue until the desired error limit is reached. In our simulations, since we obtained solutions at specific frequencies instead of all the frequencies in a wide range, we used frequency domain solver rather than time domain solver. In addition, since coils have complex 3D rotating structures, we used tetrahedral meshing in the simulations.

2.3 Experimental and Measurement Devices in Our Laboratory

In our projects, we conducted experiments in addition to numerical simulations. We investigated designed coils, components and systems both experimentally and with 3D EM simulations. Also, performance of these devices and systems were analyzed with measurements and again with simulations. To realize all these experimental studies and measurements, we have very good laboratory environment and equipments in Bilkent University. Some of the pieces of equipment that are used in our projects include: oscilloscope - Agilent Technologies (DSOX3012A, 100MHz, 2 Channels); LCR meter - Agilent Technologies (4263B, 100 Hz to 100 kHz); current clamp (Fluke i30); thermal camera (FLIR A655sc); function generator - Stanford Research Systems (DS345); and high voltage power supply - Stanford Research Systems (PS 350, 5000 V/25 W).

Chapter 3

Outer Squircle-Inner Circular Coil Architecture for Enhanced Induction over Large Areas

As we briefly mentioned in the introduction chapter, with the aim of efficient all-surface inductive heating we designed and investigated a class of small-sized coils with outer squircle-inner circular geometries. We have comparative measurements and three-dimensional (3D) electromagnetic (EM) simulations of the proposed outer squircle-inner circular coils and conventional circular shape coils. We have three patent applications [8]-[10] and the paper published in IEEE Transactions on Industrial Electronics [11] together with the manuscript ready for submission [12]. The following part is not restricted to but includes data and information reported in these papers [11, 12] and partially taken from them.

3.1 Motivation

One of the problem observed in induction heaters (and also in other types of cookers) is efficient heating of different shaped and sized vessels. In conventional

induction cookers specific heating regions exist on the surface. When a small-sized vessel (e.g., a coffee pot) is placed, which does not cover the coil beneath the surface, power transfer efficiency from the coil to the vessel substantially degrades. This can be explained with the flux produced from uncovered area of the coil. In addition, for efficient energy transfer, a vessel should ideally be placed right in the middle of the coil. These situations restrict users in terms of both the usage area and the number of vessels that can be inductively heated simultaneously.

To inductively heat different sized vessels, concentric coils have been previously proposed and widely exploited [37]-[39]. Although these coils enable more efficient heating of vessels in varying sizes than conventional coils, complete flexibility is still not possible. For efficient inductive heating, vessels having similar sizes with the inner and/or outer coils should be used. Also, vessels should be placed again right on top of the coil. With the aim of enabling complete flexibility in terms of size, location and number of simultaneously cooking vessels, arrays of small coils are used in induction cookers. Such systems have been studied for various perspectives both theoretically and experimentally [28, 35], [39]-[42]. In these previous reports, arrays of coils only with traditional shapes including circular, elliptical, square and rectangular coils have been investigated to date. Although circular shaped coils can be stacked into a more compact array by hexagonal placement, coil-to-coil interaction and coupling between these coils in the array are not strong enough as a result of the large curvatures on their outer rims. On the other hand, although they provide long interaction sides, square and rectangle shaped coils require longer wires unnecessarily than the curved coils to occupy the same area. In addition, because of their sharp corners, square and rectangular coils are not easy to produce and their couplings at the corners can be undesirable.

Different than the previous studies, we propose and demonstrate a new class of coil architecture that features squircle windings at the outer rim with fully rounded corners and long straight sides evolving into circular windings at the inner rim. This coil structure uniquely allows for strong coupling in arrays and easy manufacturing at the same time. Also, the proposed outer squircle-inner circular

coils are immune to phase noises because they exhibit high efficiencies with and without phase differences. Here we present the design and characterization of our proposed outer squircle-inner circular coils and compare their efficiency with the conventional circular coils experimentally. Further, we demonstrate the relative efficiency improvements by applying the signal to the coupled coils with 0° and 180° phase differences. The demonstrated outer squircle-inner circular coils prove to be beneficial to address the aforementioned problems of an induction cooker with large areas.

3.2 Double Coils Measurements

3.2.1 Coil Architecture and Experimental Setup

Figure 3.1 shows schematics of the manufactured coil structures, the conventional circular coil as a reference structure in Figure 3.1(a) and the proposed outer squircle-inner circular coil structure in Figure 3.1(b) as the new architecture to be studied. Also, manufactured coils are illustrated in Figure 3.2.

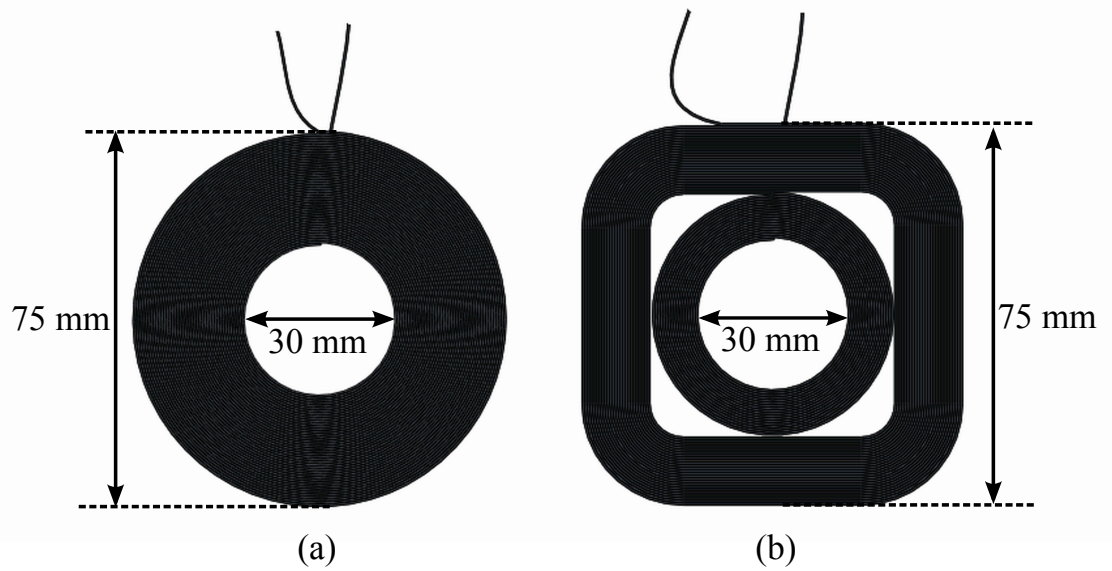

Figure 3.1: Top-view illustration of coil structures: (a) the conventional circular and (b) the proposed outer squircle-inner circular coil architectures.

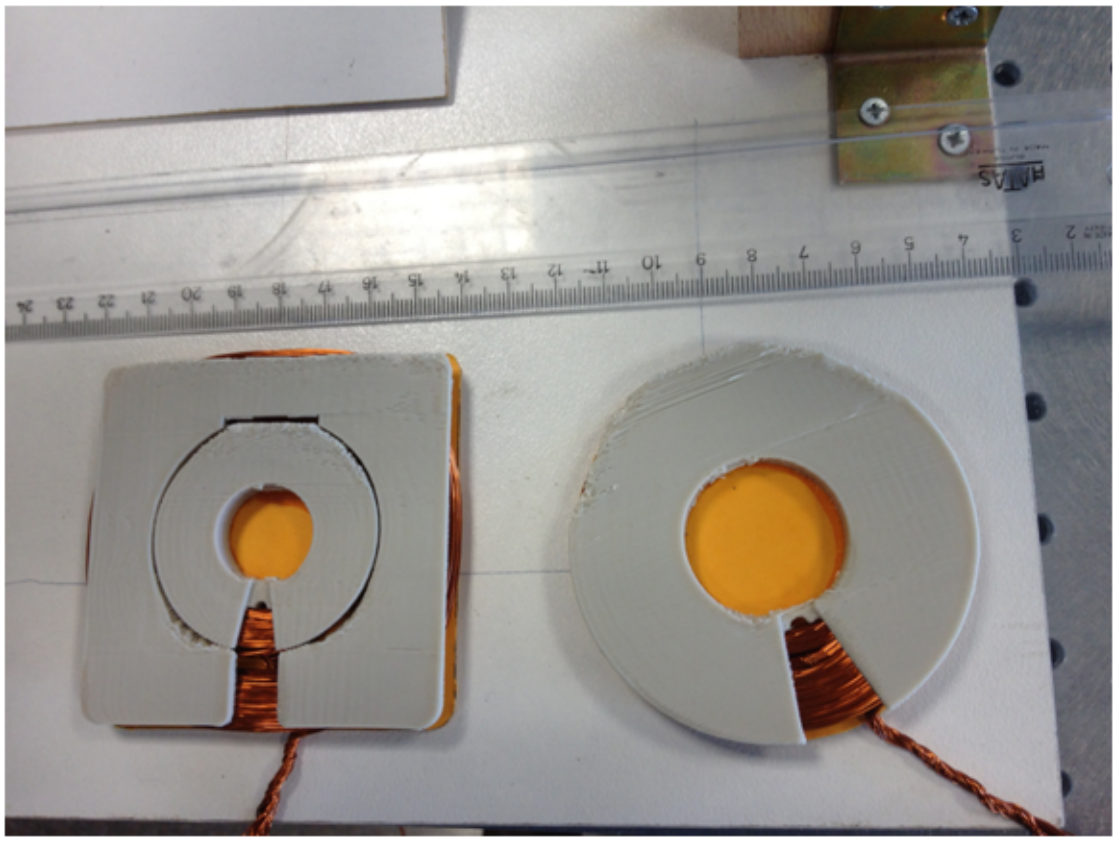

Figure 3.2: Manufactured coils from top view, where outer squircle-inner circular coil is on the left and circular coil is on the right. Here a ruler is placed next to the coils to clearly indicate geometrical parameters of the coils.

The inner diameter and the outer projection side length of these structures are fixed to 30 and 75 mm, respectively. These lengths are selected to coincide with the minimum vessel dimensions accepted by some manufacturers. In our outer squircle-inner circular coils, the straight parts constitute 35 mm of the side length. While the total turns of both of the manufactured coils are 44. In the newly designed coil there exist 18 circular turns inside and 26 squircle turns outside, adding up to a total of 44 turns, and these turns are connected to each other such that continuous current circulates in the same direction both inside and outside. In both coils, each turn is composed of 13 copper wires with 0.25 mm diameter. These parameters are optimized with full electromagnetic solutions by considering available resistance and inductance values for the power supply circuit

together with current flow capacity in the coils.

The proposed coil architecture provides a stronger coupling when two or more of these coils are placed side by side in square lattice. This is because of long tangential sides of the squircle geometry. Also, their rounded corners are unique for all-surface applications because they decrease destructive interaction (e.g., between the corners of diagonally located coils, which have currents in the same directions in the case of side by side opposite phase application). Additionally, in the proposed coil architecture, we observed that squircle turns instead of the circular windings toward the inner rim does not make a difference in terms of the resulting coil's energy transfer efficiency and mutual couplings after a certain number of squircle turns. Therefore, circular winding is effectively an adapter for the inner turns because production of square-shaped coils becomes difficult as their side lengths reduce, especially when thick wires are used. These circular turns at the inner rim favorably also reduce production cost by decreasing the amount of copper wire used.

We can briefly explain our simulations for optimum outer squircle and inner circular turn numbers as such: To understand the effect of outer squircle turn number on the coils coupling, we systematically studied power transfer efficiencies of the proposed coil architecture with carefully varied outer squircle and inner circular turn numbers. In order to do so, we investigated systems similar to that commonly used in typical induction hobs as we also constructed in our experimental setup. In the first system, two identical coils were placed side by side and a plate having cylindrical shape with 180 mm diameter and 1 mm thickness was located 14 mm above the coils. On the other hand, in the second system, instead of two identical coils, a single individual coil was used. To be similar to our experiments, coils were simulated to be driven at currents of 2.5 A amplitude and 50 kHz frequency. Since the proposed coils are designed for the enhancement of constructive coupling observed in the case of applying phase difference, 180° phase difference was used between the currents of the two side-by-side coils. Simulations were systematically repeated for two different loads, which are stainless steel (AISI 430) and aluminum plates. Simulations were further carried out using the proposed coil(s) having different outer squircle and inner circular turn

numbers while the total turn number was kept constant. In each case, we calculated the enhancement in power transfer due to coupling between the coils. The enhancement is given by equation (3.1)

$$E = \frac{P_{transfer,coupled} - P_{transfer,uncoupled}}{P_{transfer,uncoupled}} \tag{3.1}$$

where E represents the enhancement ratio, $P_{transfer,coupled}$ and $P_{transfer,uncoupled}$ are the power transfer values in the case of coupled coils and uncoupled coils, respectively. Power transfer from the uncoupled coils was found by simply doubling the transferred power from a single coil, which was calculated in the single coil simulation. In Figures 3.3 and 3.4, the enhancement as a function of the squircle turn number of the coils is shown for the stainless steel and aluminum plates, respectively, where the enhancement ratios are normalized with respect to their maximum levels.

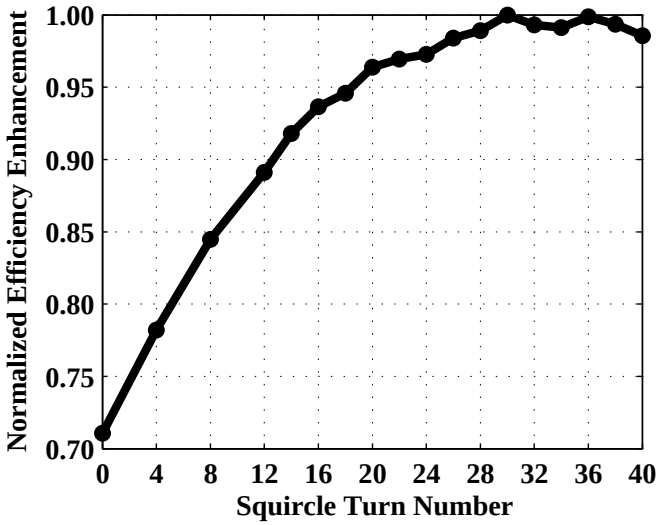

Figure 3.3: Normalized power transfer efficiency enhancement as a function of the outer squircle turn number of the proposed coil architecture calculated for the stainless steel (AISI 430) plate (for the total turn number kept fixed at 44).

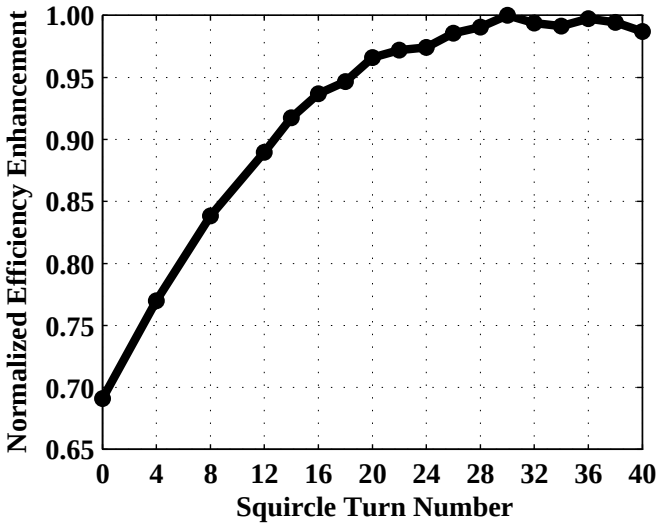

Figure 3.4: Normalized power transfer efficiency enhancement as a function of the outer squircle turn number of the proposed coil architecture calculated for the aluminum plate (for the total turn number kept fixed at 44).

In these figures, it is seen that efficiency enhancement is almost constant after 26 outer squircle turns. In other words, after 26 outer squircle turns, inner turns' being squircle or circular does not considerably change the coupling between the side-by-side placed coils. Thus, since the circular turns are easier to make and use less wire, in our proposed coil architecture we selected to employ 26 outer squircle turns (and hence 18 inner circular turns).

In addition, we conducted self-inductance and frequency dependent resistance measurements of either type of coils for frequency range from 20 kHz to 100 kHz. In our measurements we have used an LF-RF network analyzer. The measurement results are given in Figures 3.5 and 3.6 for the proposed outer squircle-inner circular and the circular coil, respectively.

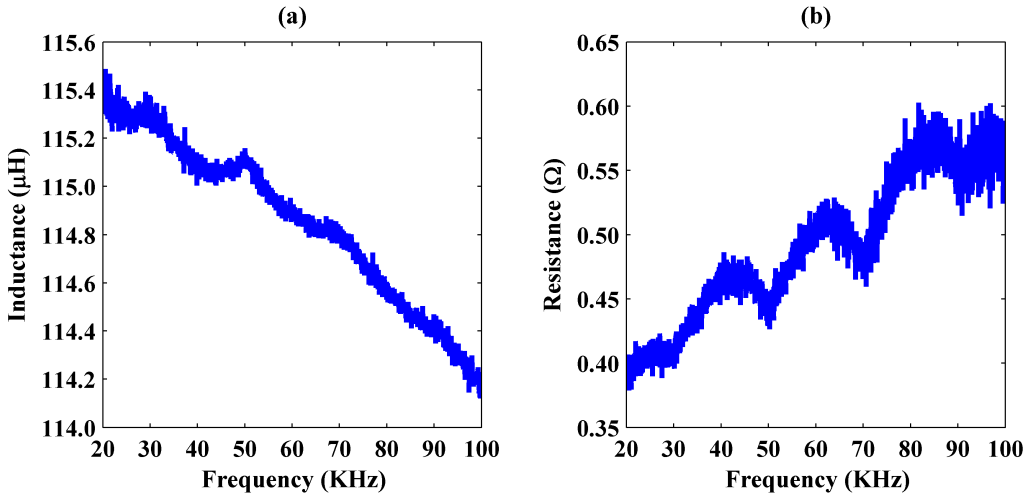

Figure 3.5: (a) Self-inductance and (b) resistance of the outer squircle-inner circular coil for frequency range from 20 kHz to 100 kHz measured by an LF-RF network analyzer.

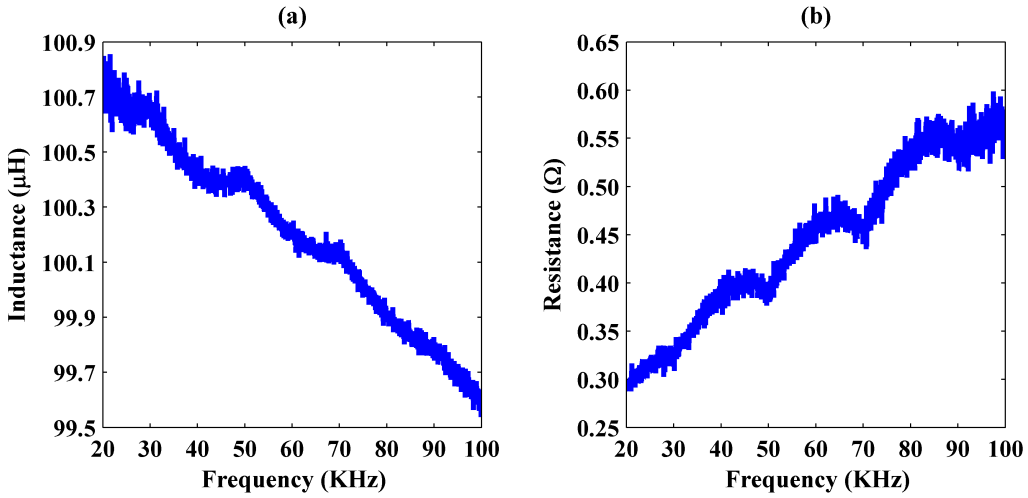

Figure 3.6: (a) Self-inductance and (b) resistance of the circular coil for frequency range from 20 kHz to 100 kHz measured by an LF-RF network analyzer.

In these figures it is seen that the resistance values of the coils are both small

and they are very close to each other. For instance, at 50 kHz, which is the frequency that we conducted heating measurements, self-resistances of the outer squircle-inner circular and the circular coil are 0.44 Ω and 0.39 Ω, respectively. These resistance values are considerably smaller than the increase in the system's equivalent resistance due to plate's loading, which indicates the power transferred to and dissipated in the plate. The increase in the constructed system's equivalent resistance and the transferred power to the plate are calculated and given in Appendix. On the other hand, measured inductance values of the coils are slightly different. This difference might be expected from different shapes of the coils and yields high efficiency of the proposed outer squircle-inner circular coil architecture. In the appendix, again we reported how much of the efficiency enhancement is because of individual coils and how much of it is due to coupling between side by side coils. However, in the figures it is clearly seen that the self-inductance of a outer squircle-inner circular coil is higher than that of a circular coil. This is expected from the fact that in squircle geometry more wire is used compared to circular geometry.

For comparison purpose, we also calculated inductance values of the individual coils with 3D full electromagnetic simulations at various frequencies. The results are illustrated in Figure 3.7. It is seen that the calculated inductance values are very close to those measured with LF-RF network analyzer, where self-inductance of an outer squircle coil is higher than that of a circular coil.

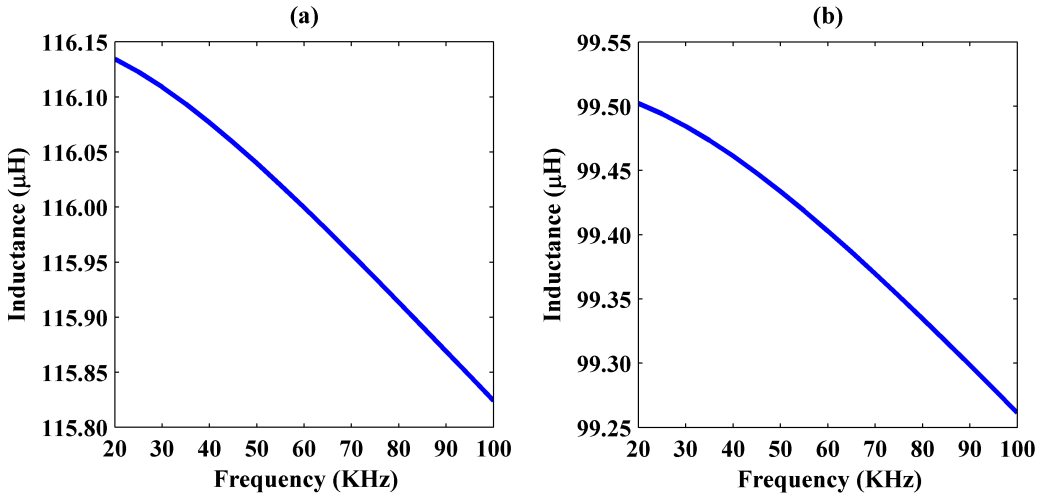

Figure 3.7: Self-inductance of the (a) outer squircle-inner circular coil and (b) circular coil for frequency range from 20 kHz to 100 kHz calculated in 3D electromagnetic simulations.

For heating measurements, we constructed a simple proof-of-concept demonstrator system. Figure 3.8 shows the cross-sectional view of our constructed heating system. In this system, we placed two identical coils side by side and a ferrite plane covering area below the coils completely. Locating ferrites below the coils is a well-known method [3, 18, 26, 27, 42, 43], in which ferrites improve heating efficiency by directing magnetic fields below the coils towards the upper half space where the heating object is located.

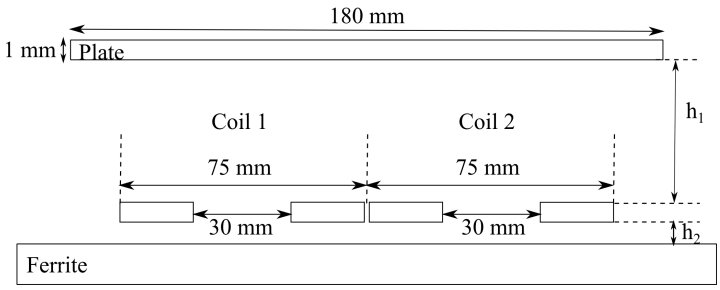

Figure 3.8: Side-view of our constructed heating test system.

In this model system, we denote the distance between the coils top plane and the ferromagnetic stainless steel plate (AISI 430) having diameter of 180 mm and a thickness of 1 mm to be h_1 = 14 mm (due to the upper peripherals and Silargan glass) and the distance between the coils back plane and the ferrite top plane to be h_2 = 1 mm (due to the substrate layer below the coils used in production). Also, to prevent infrared reflections from the steel plate that spoil thermal camera images, top surface of the plate is covered by a nylon tape (nylon 6/6) of 0.80 mm in thickness.

After tuning the system's resonance frequency by using a shunt capacitor, a driving sinusoidal signal at a resonance frequency of 50 kHz was applied by using a signal power generator. The converter and the power generator that we used in our measurements for driving coils are represented in Figure 3.9. The power generator has maximum output power of 5000 W. Because of its high power, power generator has 3 phase input at 120 V_{rms}. In our setup, AC/AC converter converts its 3 phase 220 V_{rms} input to 120 V_{rms}. Here it is important to note that although power generator has maximum power of 5000 W at its output, due to matching and heating we mostly could not reach this power at the input.

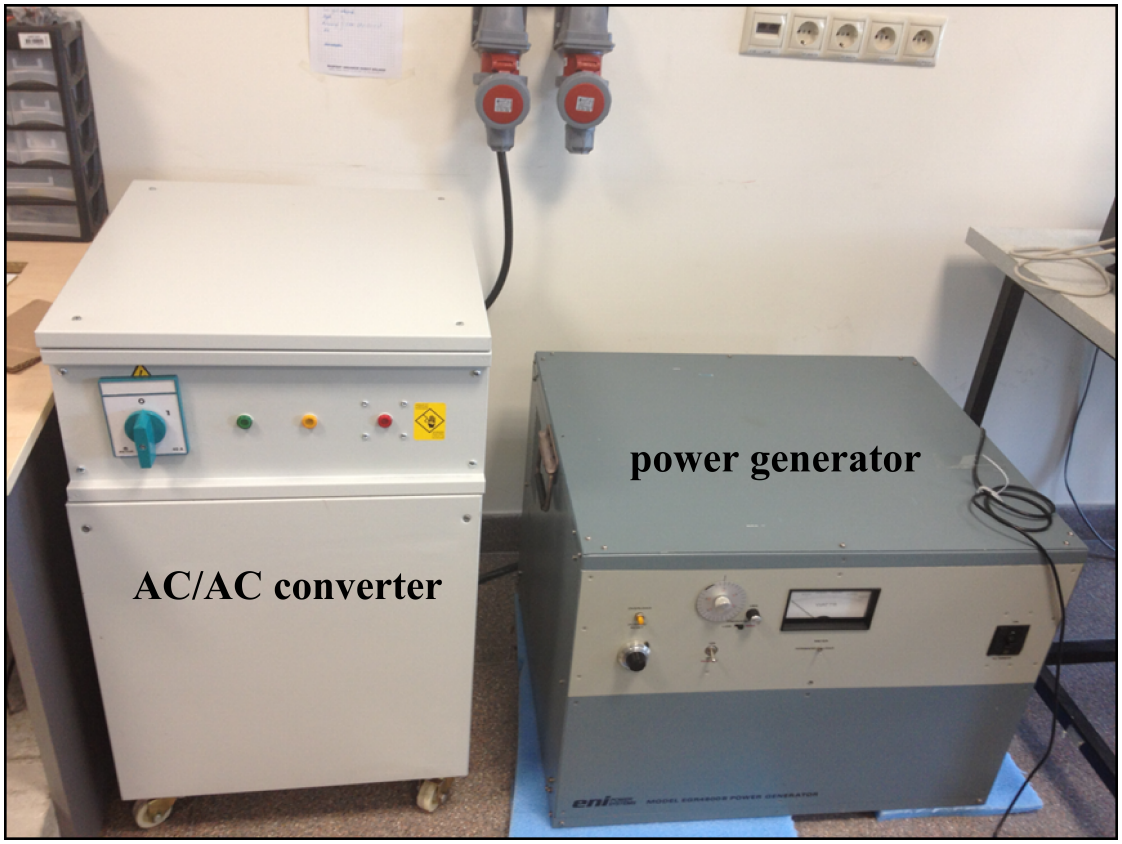

Figure 3.9: AC/AC converter and power generator.

The applied current and voltage signals were measured instantaneously monitoring both their amplitudes and the phase between them by a means of oscilloscope (Agilent DSOX3012A) with a current clamp (Fluke i30) and a voltage probe. The real power supplied to the system was calculated by using equation (3.2). Similarly, equivalent resistance and inductance values of the structures were calculated with equations (3.3) and (3.4), respectively.

$$P_{rms} = |V_{rms}||I_{rms}|cos(\phi) \tag{3.2}$$

$$R_{eq} = \frac{|V_{rms}|}{|I_{rms}|}cos(\phi) \tag{3.3}$$

$$L_{eq} = \frac{1}{\omega}\frac{|V_{rms}|}{|I_{rms}|}sin(\phi) \tag{3.4}$$

Here P_{rms} is the real rms power (W), R_{eq} is the equivalent resistance (Ω) and L_{eq} is the equivalent inductance (H). V_{rms} and I_{rms} are the rms voltage (V) and

current (A), respectively. Also, ω and ϕ are the angular frequency and phase difference between voltage and current, respectively. Total energy dissipated by the system was calculated by integrating instantaneously measured power over time. Its relation is given in equation (3.5)

$$E_{total} = \int P_{rms} \cdot dt \tag{3.5}$$

where E_{total} is the total energy (J) dissipated by the system and P_{rms} is the instantaneously measured true power (W). Therefore, changes of the equivalent resistance and inductance values are investigated together with the energy dissipated by the system. Moreover, the energy transferred to and dissipated from the stainless steel plate and the nylon tape were calculated by using equations (3.6) and (3.7), respectively.

$$Q_{total-plate} = Q_{heating-plate} + Q_{cooling-plate} \tag{3.6}$$

$$Q_{total-tape} = Q_{heating-tape} + Q_{cooling-tape} \tag{3.7}$$

Here $Q_{total-plate}$ and $Q_{total-tape}$ are the total dissipated energies on the plate and the tape, respectively. While heating, because of the temperature difference, there also occurs heat flow from the plate and the tape to the surrounding medium. Therefore, the total dissipated energies were calculated as a sum of the energy that increases the material's temperature and the heat that is transferred from the material to the medium (here it is air). Energies that increase the plate and tape's temperature were calculated by using equation (3.8)

$$Q_{heating} = d \cdot V \cdot C \cdot \Delta T \tag{3.8}$$

where $Q_{heating}$ is the heating energy (J), d is the material density (7.74 x 10^{-6} kg/mm^3 for the stainless steel and 1.15 x 10^{-6} kg/mm^3 for the nylon 6/6), V is the volume of the material (V = π x 90mm x 90mm x 1mm for the cylindrical steel plate and V = π x 90mm x 90mm x 0.8mm for the rounded nylon tape), C is the specific heat of the material (460 $J \cdot kg^{-1}/^{\circ}C$ for the stainless steel and 1700 $J \cdot kg^{-1}/^{\circ}C$ for the nylon 6/6) and ΔT is the temperature increase ($^{\circ}C$). Similarly, the energy transferred from the plate and tape to the surrounding medium was calculated by using equation (3.9)

$$Q_{cooling} = \int (h \cdot A \cdot \Delta K) dt \tag{3.9}$$

where $Q_{cooling}$ is the transferred energy (J), h is the heat transfer coefficient (25 $\mathrm{W/m^2 \cdot {}^\circ}K$ for the stainless steel and 0.25 $\mathrm{W/m^2 \cdot {}^\circ}K$ for the nylon 6/6), A is the surface area (A = π x 90mm x 90mm + 2 x π x 90mm x 1mm for the steel plate and A = π x 90mm x 90mm + 2 x π x 90mm x 0.8mm for the nylon tape), and ΔK is the temperature difference ($^\circ C$) between the materials (plate and tape) and the surrounding medium. The transferred heat energy is the integral of the transferred power from the material to the medium over time.

Since the plate is heated up starting from regions above the coils, temperature distribution over the tape observed at time instants is not uniform. We calculated average temperature by simply taking integral of the temperature distribution over the tape's top surface using the thermal camera's calibrated image and divided the result by the top surface area. In our measurements, a thermal camera (FLIR A655sc) that detects infrared radiation (heat) and creates clear images based on capturing temperature difference profile is used. In equation (3.8), the temperature change ΔT is considered as the change in the calculated average temperature. Similarly, in equation (3.9) the temperature difference ΔK is taken as the difference between the calculated average temperature and the ambient temperature. In these calculations, because the steel plate's and the tape's thicknesses are so small (1.8 mm in total), the temperature gradient from the plate's bottom surface to the tape's top surface is ignored.

Our measurement setup is illustrated in Figure 3.10, where measurement tools are pointed out with red arrows.

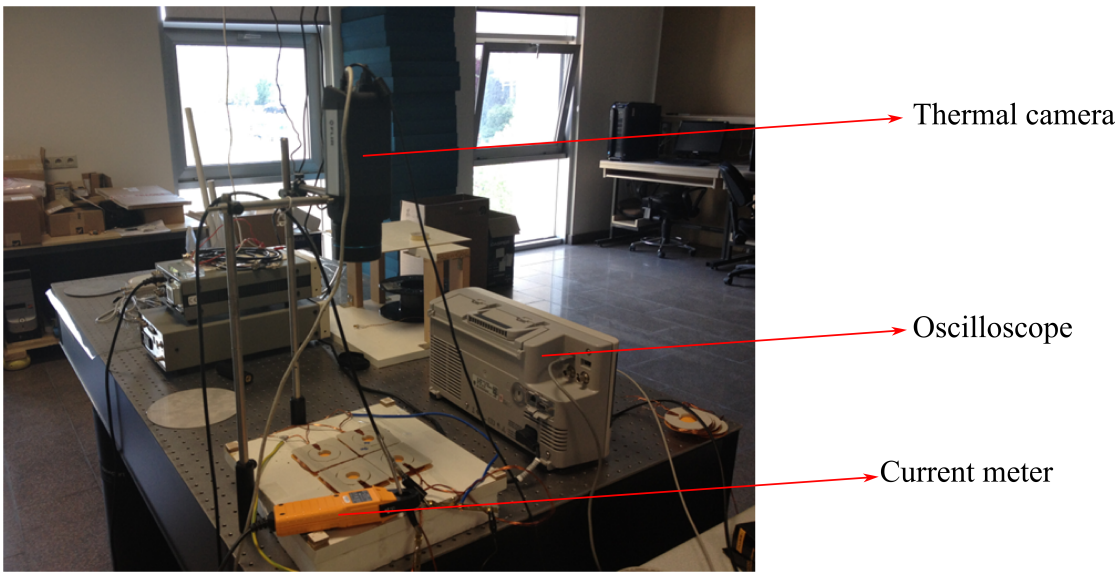

Figure 3.10: Measurement setup and measurement tools used in heating experiments.

3.2.2 Results and Discussion

For a comparative study, measurements were repeated with the proposed outer squircle-inner circular and the conventional circular coils. Also, to investigate its effect on the system's heating efficiency, phase difference was applied between adjacent coils and measurements were again repeated. Since two coils are connected in parallel, we applied 0° and 180° phase differences. The 0° phase difference means that coils' currents flow in the same direction. The 180° phase difference thus corresponds to the coils' currents flowing in the reverse directions. In practice, 0° and 180° phase differences can be applied simply by reversing the polarity of the terminals of the coils.

Figure 3.11 shows thermal images taken at 0, 30 and 60 s after power is switched on for the outer squircle-inner circular coil. Here the plate's temperature distribution changing with time is clearly seen. In Figure 3.11(a), due to 0° phase difference, coils couple destructively around their close edges and constructively around their far sides. As a result, temperature of the plate is higher

in regions above the far sides of the coils than those above the close sides. On the other hand, in Figure 3.11(b), due to 180° phase difference, fields interfere constructively at the close sides of the coils. Therefore, the plate is heated up starting from regions above the close edges of the coils.

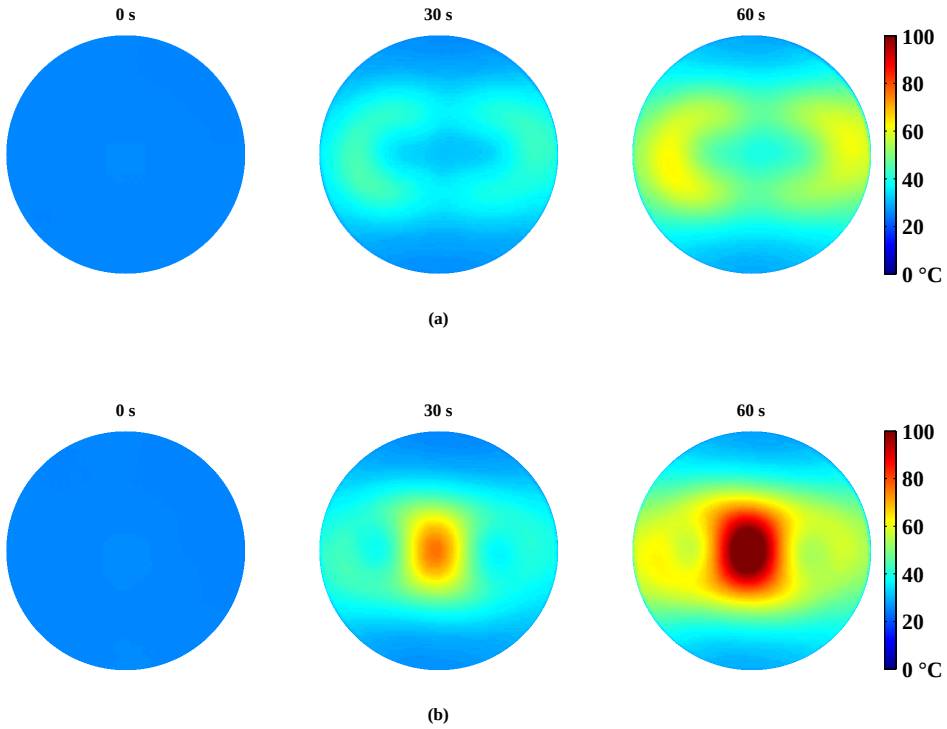

Figure 3.11: Temperature distributions on the stainless steel plate at various time instants (0, 30 and 60 s) after power is switched on. Here the plate is placed above a pair of the outer squircle-inner circular coils driven with (a) 0° phase difference and (b) 180° phase difference.

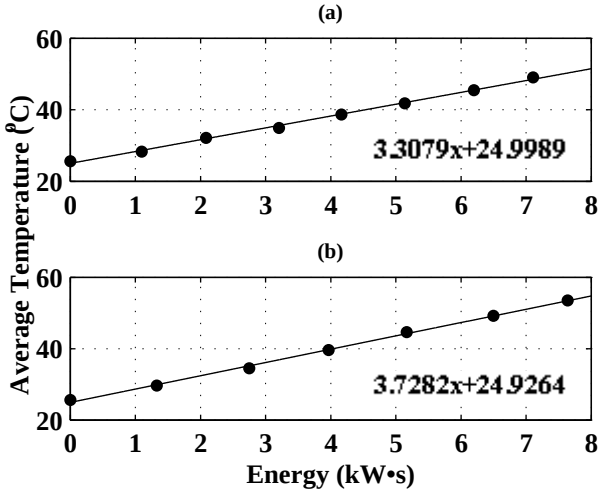

Figure 3.12: Average temperature increase over the plate as a function of the energy supplied to and dissipated in the system. Here the plate was placed above a pair of the outer squircle-inner circular coils driven with (a) 0° phase difference and (b) 180° phase difference.

Figure 3.12 shows the average temperature as a function of the total real energy supplied to and dissipated in the system at different time instants of 10 s intervals, running up to a total energy level of 8 $kW \cdot s$ (0, 10, 20, 30, 40, 50, 60 and 70 s for the 0° phase difference in part (a) and 0, 10, 20, 30, 40, 50 and 60 s for the 180° phase difference in part (b)). Fitting curves indicate that the temperature increases linearly at a rate of approximately 3.31 $°C/(kW \cdot s)$ for the 0° phase difference and 3.73 $°C/(kW \cdot s)$ for the 180° phase difference. In other words, with 1000 $W \cdot s$ input energy dissipated in the system, the plate's temperature increases by 3.31 $°C$ and 3.73 $°C$ on average when the proposed outer squircle-inner circular coils are driven with the 0° and 180° phase differences. This is a useful figure of merit for efficiency comparisons.

Another figure of merit that we used in our study for efficiency is the ratio of the energy transferred to and dissipated on the plate/tape ($Q_{total-plate} + Q_{total-tape}$) to the total energy dissipated in the system (E_{total}). In the system, when 0° phase difference exists between the coils, using equation (3.8), we found the heating energies dissipated on the stainless steel plate and the nylon tape over 70 s to be

equal to 2130.86 $W \cdot s$ and 936.04 $W \cdot s$, respectively. Similarly, with equation (3.9), energies transferred from the plate and the tape to the air medium were calculated to be 547.45 $W \cdot s$ and 5.47 $W \cdot s$, respectively. In addition, the total real energy supplied to the system over 70 s was 7109.93 $W \cdot s$. Therefore, in total 0.509 ((2130.86 + 936.04 + 547.45 + 5.47) / 7109.93) ratio of the real energy supplied to the system was transferred to and dissipated on the plate/tape. Similarly, in the system, when the coils were driven with 180° phase difference, the total energy dissipated on the plate/tape and the real energy supplied to the system over 60 s were found to be 4289.15 $W \cdot s$ and 7637.50 $W \cdot s$, respectively. Resultantly, 0.562 (4289.15 / 7637.50) ratio of the real energy supplied to the system was transferred to the plate/tape.

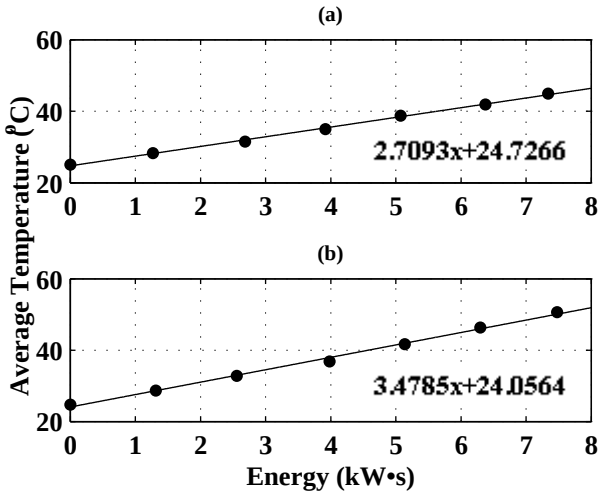

Figure 3.13: Average temperature increase over the plate as a function of the energy supplied to and dissipated in the system. Here the plate was placed above a pair of the circular coils driven with (a) 0° phase difference and (b) 180° phase difference.

We replaced the outer squircle-inner circular coils with the conventional circular coils and measurements were repeated with the 0° and 180° phase differences between coils. Again, in Figure 3.13 dots represent the data points of the calculated average temperatures and the total real energies supplied to and dissipated

in the system at time instants (0, 10, 20, 30, 40, 50 and 60 s) of which thermal images were captured. Also, in the figure the fitting curves give slopes of approximately 2.71 $°C/(kW \cdot s)$ and 3.48 $°C/(kW \cdot s)$ for the 0° and 180° phase differences, respectively. These results (shown in Figure 3.13) are tabulated in Table 3.1 together with those of outer squircle-inner circular coils (given in Figure 3.12).

Table 3.1: Comparison of proposed outer squircle-inner circular and conventional circular coils.

Coils	Phase	Temperature Increase Rate ($°C/(kW \cdot s)$)	Energy Transfer Ratio
Outer squircle-inner circular	0°	3.31	0.509
	180°	3.73	0.562
Circular	0°	2.71	0.409
	180°	3.48	0.524

As shown in Table 3.1, the results are consistently better for the outer squircle-inner circular coils than the circular coils. This means that the proposed coils lead to higher heating efficiency than the conventional circular coils. In addition, applying the 180° phase difference increases the efficiency. The outer squircle-inner circular coil reaches the highest heating rate of all when driven with the 180° phase difference. The energy transfer ratio found for the outer squircle-inner circular coil with the 180° phase difference is 37.4% higher than the ratio calculated for the circular coil with the 0° phase difference.

The high efficiencies in Table 3.1 obtained with the outer squircle-inner circular coil also imply that the proposed outer squircle-inner circular coils are less sensitive to phase differences than conventional circular coils. This might be due to unusual geometry of the outer squircle-inner circular coils. Long tangential sides in squircle geometry increase interaction between adjacent coils.

In Figure 3.14 temperature distributions on the plate with equal amount of real energies supplied to the systems are illustrated. As in previous figures, in

Figure 3.14 temperature of the plate was higher above the far sides of the coils than above the close sides when 0° phase difference exists between coil currents. On the other hand, temperature of the plate was the highest at its center when the coils were driven with opposite phases. In all of these thermal camera snapshots, the temperature of the plate was higher for the newly designed outer squircle-inner circular coils than the conventional circular coils.

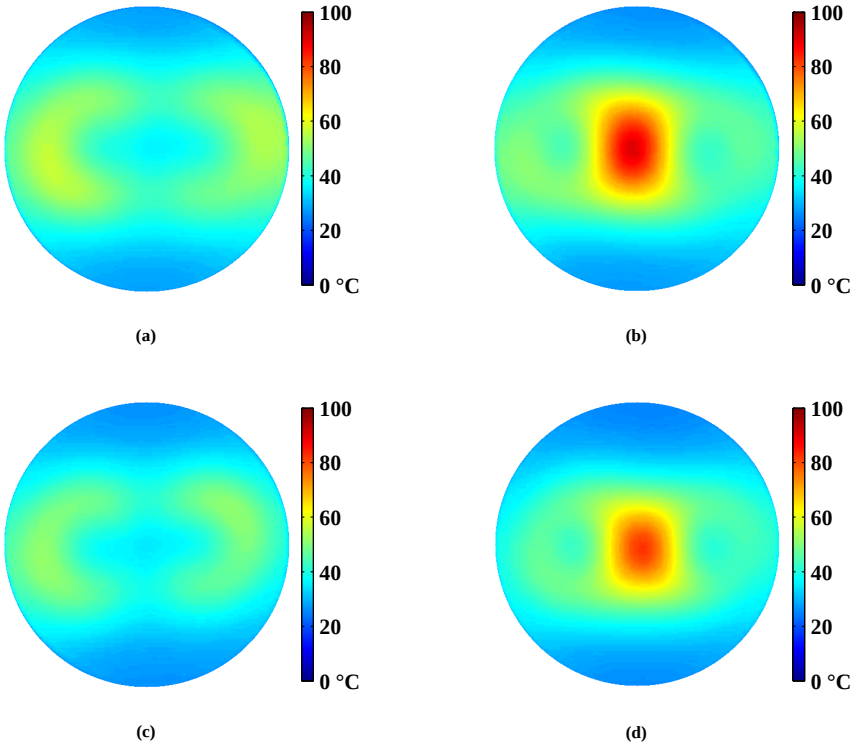

Figure 3.14: Temperature distributions on the stainless steel plate with a total supplied real energy of approximately 5 $kW{\cdot}s$: for the outer squircle-inner circular coil pair driven with (a) 0° and (b) 180° phase difference and the conventional circular coil pair driven with (c) 0° and (d) 180° phase difference.

In addition, for comparison purposes, temperature increase of the plate for all systems is presented in Figure 3.15 across a fixed line that passes through the center of the plate. This line can be visualized as a horizontal line that passes through the middle of the plate and the coils' heating areas in Figure 3.14. Also,

temperature increase is the difference between the plate temperature after 5 $kW{\cdot}s$ total real energy was supplied to the system and its initial temperature when no energy was supplied. In Figure 3.15 legends S0 and S180 represent systems in which the outer squircle-inner circular coil pair was driven with the 0° and 180° phase differences, respectively. Similarly, legends C0 and C180 denote the systems where the circular coil pair was driven with the 0° and 180° phase differences, respectively. To visually aid the reader, the temperature profiles were plotted to have their central point at the position 0 mm.

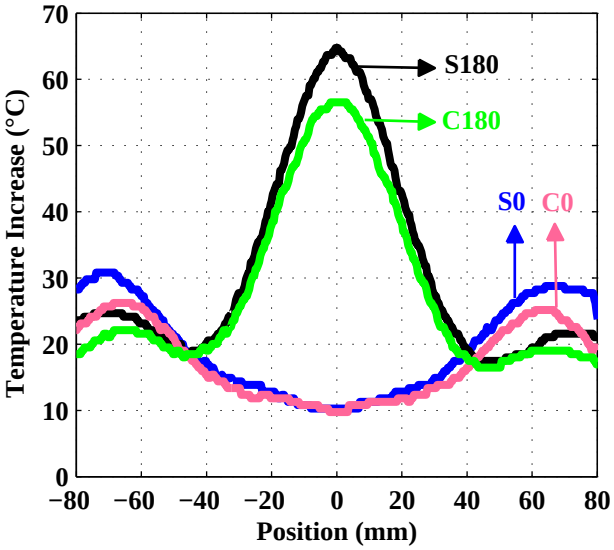

Figure 3.15: Temperature increase on constant line that passes through the middle of the plate. Here approximately 5 $kW \cdot s$ total real energies are supplied to the systems.

In Figure 3.15 pairwise comparisons of profile S0 with profile C0, and S180 with C180 indicate that the temperature increase in the plate is higher in systems where newly designed outer squircle-inner circular coils were used instead of the conventional circular coils. Since the total real energy supplied to the system is constant, similar trends were observed for the energy transfer ratio. These results agree well with our previous results given in Table 3.1.

Furthermore, to investigate the availability of the proposed outer squircle-inner circular coil for the power supply circuitry used to drive conventional coils, equivalent resistance and inductance values of the designs were calculated using equations (3.3) and (3.4), respectively. For this, voltage and current signals applied to the system were measured instantaneously over time. In Figure 3.16 measured electrical parameters including applied voltage, rated current and true power levels are presented as a function of the supplied real energy. In these and following figures, data points are denoted with markers and curves show the first order (in Figure 3.16(a)) and the second order (in Figures 3.16(b) and 3.16(c)) fittings. As in Figure 3.15, here S0 and S180 again represent the systems where the outer squircle-inner circular coil pair is driven with the 0° and 180° phase differences, respectively. Similarly, C0 and C180 correspond to the systems where the circular coil pair is driven with the 0° and 180° phase differences, respectively.

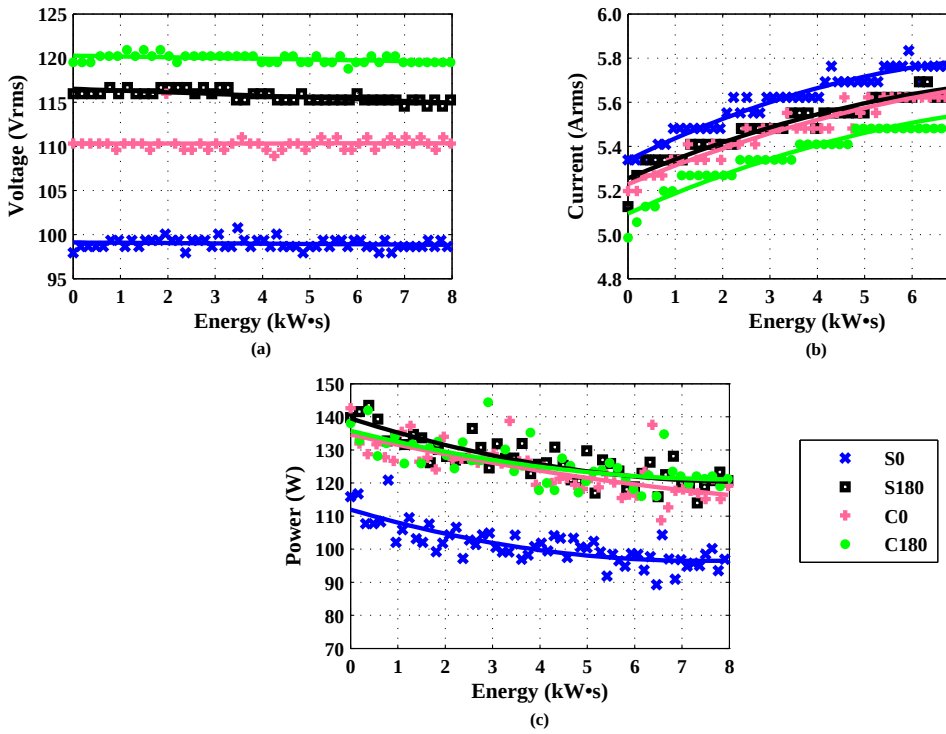

Figure 3.16: Measured electrical parameters (a) applied voltage, (b) rated current, and (c) true power levels as a function of the real energy supplied to the system.

In our system, supply circuit behaves as a voltage source (see Figure 3.16(a)). For fair comparison, input currents are set to similar values but with energy the rated current values increase. This is explained with the decrease in system impedance. In addition, the power supplied to and dissipated in the system decreases with energy, too. In Figure 3.16, despite their similar rated current values, the dissipated power is noticeably lower in the system, where the outer squircle-inner circular coil pair is driven with the 0° phase difference, than those in the other systems. These changes are related with variations in the resistance and the inductance. Resistance and inductance values of the system are important not only for the power transmission but also the vessel detection. Results are shown in Figure 3.17 and Figure 3.18.

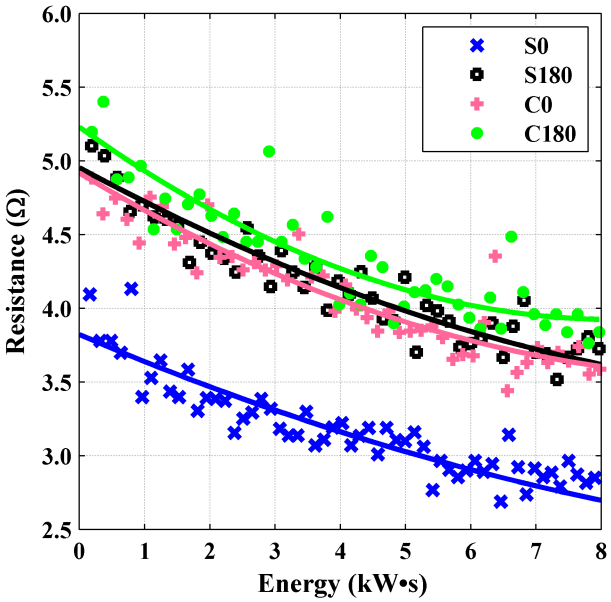

Figure 3.17: Systems equivalent resistance as a function of the supplied real energy.

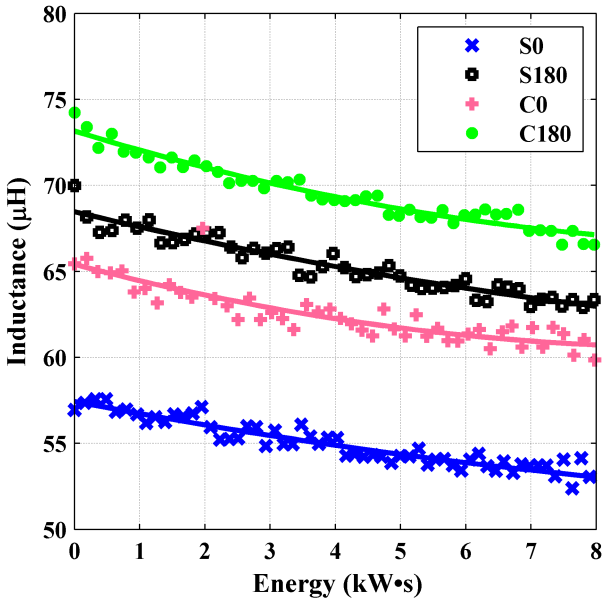

Figure 3.18: Systems equivalent inductance as a function of the supplied real energy.

In Figure 3.17 equivalent resistances of the system have close values. Especially, the system using newly designed outer squircle-inner circular coil pair driven with the 180° phase difference has very similar equivalent resistance values to those systems where the circular coils are used. This is valuable because the new coil design having resistance values close to those of the conventional coil systems is desired for power circuitry.

The low resistance values in the system where the outer squircle-inner circular coils have 0° phase difference lead to a decrease in the supply power (see Figure 3.16(c)). Resultantly, in Figure 3.12, a slower enhancement in average temperature over time was observed in the 0° phase difference measurement. For example, in the system where the outer squircle-inner circular coils had 0° phase difference, the average temperature reached 50 $°C$ around 75 s but in the system where the designed coils were driven with the 180° phase difference the average temperature reached 50 $°C$ in 52 s. Slow heating of the plate causes increased heat loss from the plate to the medium ($Q_{cooling}$ in equation (3.9)). The low

value of the temperature increase rate in Table 3.1 for the outer squircle-inner circular coils having 0° phase difference with respect to the energy transfer ratio is because of this high amount of heat loss to the medium.

Moreover, in Figure 3.18, equivalent inductance values are lower in the systems represented with S0 and S180 than those of C0 and C180, respectively. However, similar to the resistance trends, inductance values of the systems are still close to each other. Again, this is good for the power circuitry and vessel detection.

In the figures, equivalent resistance and inductance of the systems decrease with energy. Although electrical resistivity and magnetic permeability of the stainless steel and iron compounds increase with temperature (down to the Curie point) [44, 45], this reduction can be explained with decreased coupling. Flux generated by the coils decreases as their temperature increases. This results in reduction in the system's equivalent inductance. Similarly, because coupling decreases, the total power dissipation in the system reduces, too. This might be the reason of the observed decrease in the system's equivalent resistance.

The system was further analyzed with three-dimensional (3D) numerical simulations. The magnetic flux produced by the coils and the resulting induced eddy currents on the plate were calculated. In the simulations, pairs of the proposed outer squircle-inner circular and the circular coils were placed side by side and a steel plate having cylindrical shape with 1 mm thickness and 180 mm diameter was located 14 mm above from the coil. The rated current values initially supplied to the coils in measurements were around 5 A (see Figure 3.16(b)). Since coils were connected in parallel, currents flowing on each of the coil were approximately 2.5 A. Therefore, in the simulations each coil was driven by separate current sources alternating at 50 kHz frequency with 2.5 A amplitude and 0° and 180° phase differences. Magnetic flux distribution normal to the plate's bottom surface (14 mm above from the coils) and amplitude distribution of the induced eddy currents tangential on the plate's bottom surface are shown in Figure 3.19.

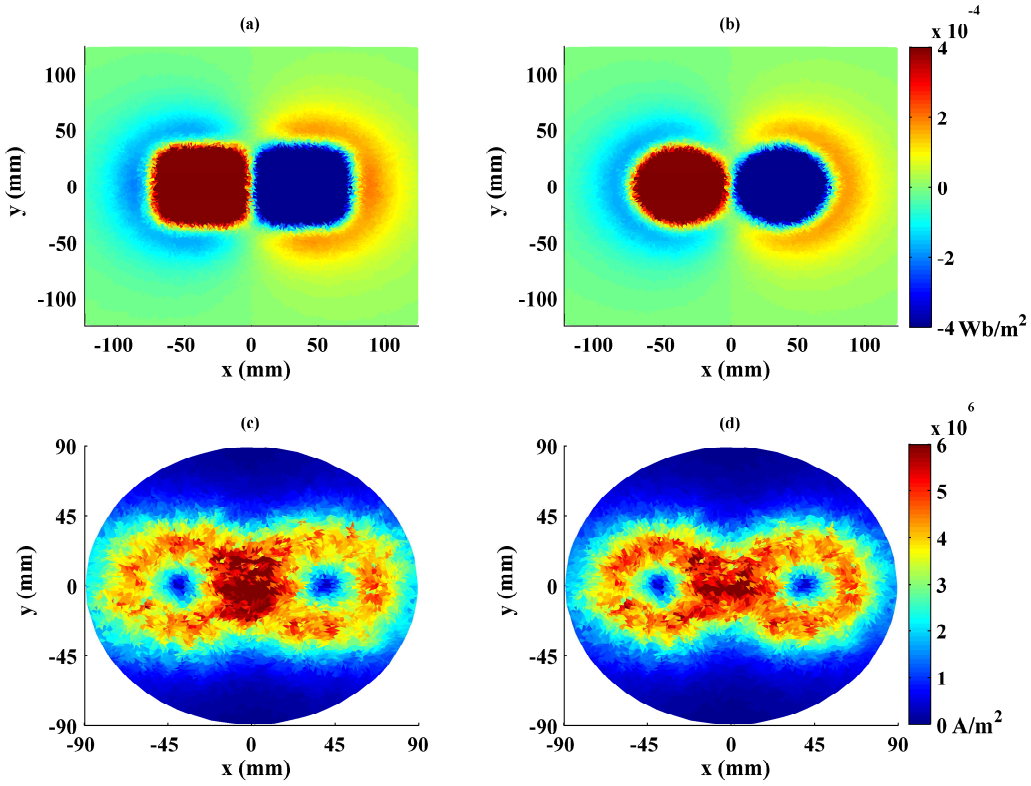

Figure 3.19: Magnetic flux distributions normal to the plate's bottom surface 14 mm above from pairs of (a) outer squircle-inner circular and (b) circular coils and tangential current intensity distributions on the plate's bottom surface with pairs of (c) outer squircle-inner circular and (d) circular coils . Here 180° phase difference exists between the coils. Note that axis scaling in the subfigures is not all the same.

In the figure, because the coils are driven with 180° phase differences, the magnetic fluxes are in reverse directions (see Figures 3.19(a) and 3.19(b)). Therefore, the induced eddy currents are in reverse directions, too. For instance, current induced on one side is in clockwise direction and on the other side it is in counterclockwise direction. At the center, these induced eddy currents are in the same direction, both in +y direction in the figures. Therefore, the induced eddy currents couple constructively at the plate's center. This is clearly seen in current density distributions in Figures 3.19(c) and 3.19(d). In addition, the magnetic

fluxes have distributions with shapes similar to those of the coils, i.e., squircle shape in (a) and circular shape in (b). The reverse directed magnetic fluxes around these shapes are because of magnetic fields' curling. However, these curled magnetic fluxes have smaller magnitudes than fluxes that directly hit the plate's bottom surface. Therefore, the induced eddy currents on the plate's bottom surface are mostly induced by the magnetic fluxes directly impingent on the plate. In systems where the proposed outer squircle-inner circular coils are used, the magnetic fluxes and the induced eddy currents have longer tangential sides that increase the interaction than those in systems where the circular coils are used. Long tangential sides of the magnetic fluxes that increase the interaction and the high current densities at the plate's center in the system where the proposed outer squircle-inner circular coils are used are clearly seen in the figure.

In the simulations, contributions of the plate to system's equivalent resistance were calculated, too. This is important because for a constant current there is a linear relation between the plate's contribution to the resistance value and the power transferred to and dissipated in the plate. Increase in the system's equivalent resistance with the plate's placement, where a pair of the outer squircle-inner circular coils are driven by currents having 180° phase difference, was calculated as 4.721 Ω. On the other hand, in the system where the circular coils are driven by currents having 0° phase difference, increase in the system's resistance with the plate's placement was found as 3.499 Ω. Therefore, the transferred power to the plate calculated in the system where the proposed outer squircle-inner circular coils have 180° phase difference is 34.9% higher than that found in the system where the circular coils have 0° phase difference. This enhancement is close to the value that we experimentally accomplished in the measurements (37.4%).

System simulations were obtained with plates made of different materials, having various sizes and being located at different distances from the coils. These loading parameters were selected to cover the entire range specific to induction heating hob systems. In all these simulations, the highest efficiency was found out in the systems where the proposed outer squircle-inner circular coils were used and driven with 180° phase difference. The proposed outer squircle-inner

circular coils were thus found to exhibit better performance than that of conventional circular coils for all possible loading conditions common to induction heating application. All the simulation results that we obtained are given and explained in detail in Appendix A.

3.2.3 Summary

In this study, a newly proposed architecture of outer squircle-inner circular coils is presented. Energy transfer and heating efficiencies are measured and results are compared with those of conventional circular coils. Also, the effect of phase difference application between the coils on heating efficiency is investigated with comparative 0° and 180° phase difference measurements. In experiments, the proposed outer squircle-inner circular coils exhibit higher heating efficiencies than those obtained with the conventional circular coils, with an overall enhancement of 37.4% in the system efficiency. In addition, driving coils with the 180° phase difference is shown to further increases efficiency. Therefore, the highest efficiency is obtained in the case where the outer squircle-inner circular coil pair is driven with the 180° phase difference, reaching a maximum level of. Equivalent inductance and resistance of the systems were measured, too. Systems with the proposed outer squircle-inner circular coils sustain similar inductance and resistance values with those of the conventional circular coil systems, which is favorable for power circuitry and vessel detection. Measurement results were also verified with 3D numerical simulations. The finding of this study are beneficial for induction cooking ovens in terms of efficient heating of different sized vessels and full coverage of the oven surface. Also, another important advantage is relative adaptability to phase difference applications.

3.3 Four Coils Measurements

In the previous section we have investigated power transfer and heating efficiency of systems where pair of the outer squircle-inner circular and conventional circular

coils were placed side-by-side and 0° and 180° phase differences were applied between them. Measurement and simulation results demonstrate that the highest heating and power transfer efficiencies are obtained in the system where a pair of the outer squircle-inner circular coils are driven with the 180° phase difference. However, in all-surface heating application there are multiple coils placed in an array. In that case, efficiency enhancement with the outer squircle-inner circular coils' coupling that are driven by the 180° phase difference is expected to be much higher than that observed in the system where a pair of the outer squircle-inner circular coils are used and driven by currents having 180° phase difference. To be able to observe the enhancement with usage of the multiple coils we located four coils (instead of two) in the system and obtained the same measurements within the previous section. The same plate within the previous measurements, i.e., cylindrical shape stainless steel (AISI 430) plate having 180 mm diameter and 1 mm thickness, was used. Measurements were repeated with the outer squircle-inner circular and the conventional circular coils. Study in this section is beneficial in terms of investigating enhancement in coupling between coils, which improves systems heating and power transfer efficiencies, together with the phase difference effect in multiple coil system. This section might also be considered as a preliminary for the next chapter in which a heating system composed of nine of the designed outer squircle-inner circular coils aligned tangentially in a two-dimensional lattice is studied.

3.3.1 Experimental Setup

In our measurements we placed four of the outer squircle-inner circular and the conventional circular coils tangentially in a two-dimensional (2D) square lattice. In square lattice, center points of the coils form a square shape. The constructed setup with four of the outer squircle-inner circular coils is illustrated in Figure 3.20. In the system, coils are placed tangentially with no distances between, i.e., their sides are in contact. Alignment of the coils are clearly seen in Figure 3.20(a). Also, in the system ferrite layers are located below the coils and the metal plate is placed above the coils.

(a) (b)

Figure 3.20: Measurement setup and alignment of the coils (a) without metal plate, (b) with metal plate.

3.3.2 Results and Discussion

Heating experiments were conducted with the outer squircle-inner circular and the conventional circular coils. 0° and 180° phase differences were applied between the consecutive coils in the system. Temperature distributions on the stainless steel plate at various time instants (0, 60 and 120 s) after power is switched on are illustrated in Figure 3.21, for the system in which four of the outer squircle-inner circular coils are driven with currents such that 0° (in Figure 3.21(a)) and 180° (in Figure 3.21(b)) phase differences exist between consecutive coils.

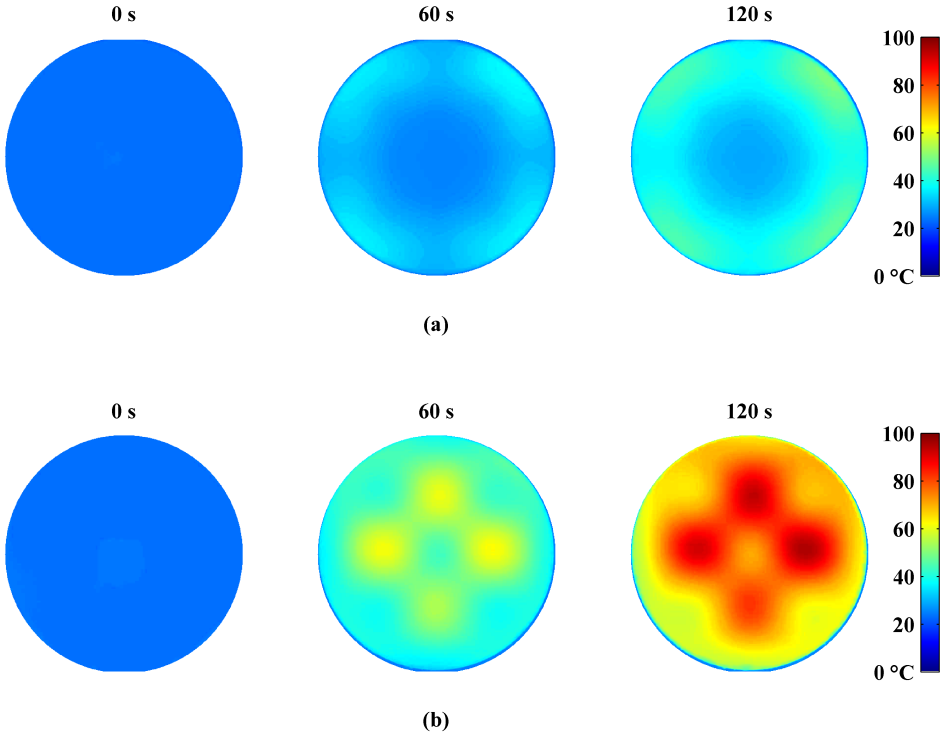

Figure 3.21: Temperature distributions on the stainless steel plate at various time instants (0, 60 and 120 s) after power is switched on. Here the plate is placed above four of the outer squircle-inner circular coils driven with (a) 0° phase difference and (b) 180° phase difference.

In the case, where the 0° phase difference exists between the consecutive coils, steel plate heats up starting from the regions above the corners of the coils. It is similar to the plate's heating in Figure 3.11(a), where the plate is placed above a pair of the outer squircle-inner circular coils and heats up starting from regions above the far edges of the coils. In Figure 3.21(a), since each coil is placed in a 2D square lattice to be tangential with other two coils and they all have the 0° phase difference between, hot spots arise in regions above the corners of the coils that are the farthest from each other. On the other hand, in the system where 180° phase difference exists between the consecutive coils, the plate heats up starting from regions above the close edges of the consecutive coils. Since 180° phase difference

exists between the consecutive coils, they constructively interfere with each other in regions above their close edges. Resultantly, in Figure 3.21(b) four regions of high temperatures arise with time. It is similar to that observed in Figure 3.11(b). In addition, in the figure undesirable coupling between diagonally located coils is easily seen. More clearly, the low temperature at the center corresponds to the area where four diagonally located coils are being closest. It is one of the reasons why we propose novel coil architecture with squircle turns at the outer rim. In Figure 3.21, small variations in temperature distributions that violate the absolute symmetry are because of experimental errors, i.e., the manufactured coils' being different from each other and their various distances to the plate.

The same measurements were obtained with the conventional circular coils. Temperature distributions on the plate at different time instants (0, 60 and 120 s) after power is switched on are shown in Figure 3.22. As expected, in the system, where 0° phase difference exists between the consecutive coils, plate heats up starting from the regions above the corners of the coils, whereas in the case of 180° phase difference application to consecutive coils plate's temperature is the highest in the regions above the adjacent coils' close edges.

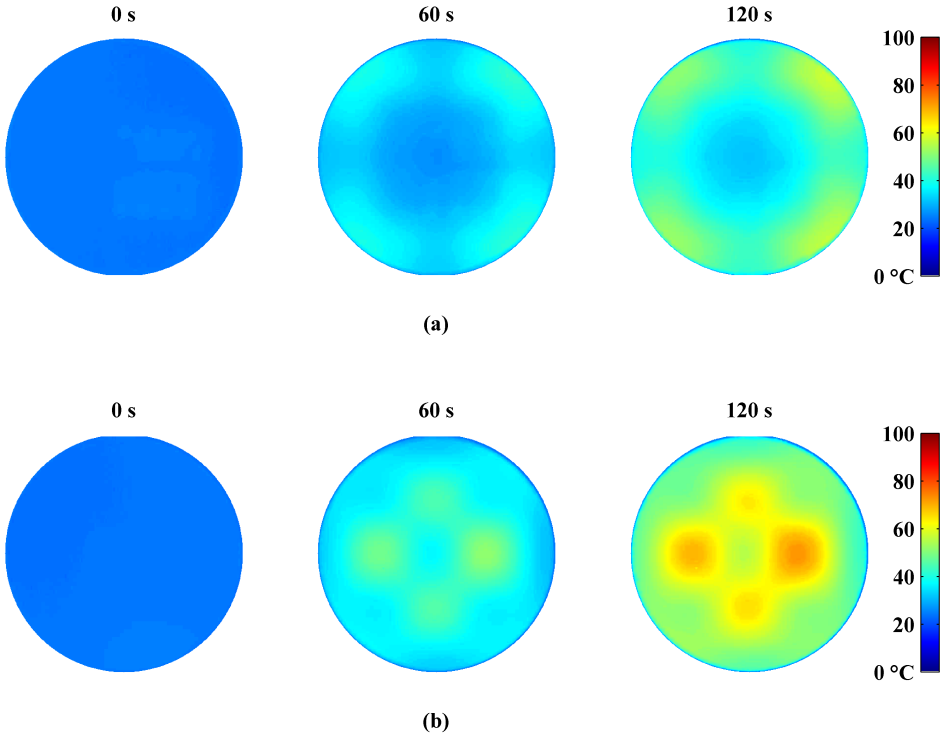

Figure 3.22: Temperature distributions on the stainless steel plate at various time instants (0, 60 and 120 s) after power is switched on. Here the plate is placed above four of the circular coils driven with (a) 0° phase difference and (b) 180° phase difference.

In Figures 3.21(a) and 3.22(a), plate's heating is considerably slower than that observed in Figures 3.21(b) and 3.22(b), respectively. One of the reason for heating enhancement is 180° phase difference application. However, another reason for the plate's heating being very slow in Figures 3.21(a) and 3.22(a) than that in Figures 3.21(b) and 3.22(b), respectively, is that the load plate having 180 mm diameter does not completely cover the four outer squircle-inner circular and the four circular coils. Corners of the coils that are the farthest from each other are uncovered but in 0° phase difference application plate heats up starting from regions above these corners. Therefore, in heating experiments of the system, where four coils are driven by 0° phase difference, it might be better to use

larger plates. On the other hand, in system measurements where 180° phase difference exists between the consecutive coils, plate covers the regions at which coils interfere constructively. In regions that are not covered by the plate, i.e., regions above the corners of the coils, heating is very slow. Therefore, in heating experiments of the system, where four coils are driven by 180° phase difference, using a plate with 180 mm diameter does not create a problem.

We investigated heating of the plate not just as a function of time but also as a function of energy supplied to and dissipated in the system. Figure 3.23 shows the average temperature as a function of the total real energy supplied to and dissipated in the system at different time instants of 10 s intervals, running up to a total energy level of 15 $kW \cdot s$ (0, 10, 20, 30, 40, 50, 60, 70, 80, 90 and 100 s for the outer squircle-inner circular coils in part (a) and circular coils in part (b)). Fitting curves indicate that temperature increases linearly at a rate of approximately 2.81 $^{\circ}C/(kW \cdot s)$ for the outer squircle-inner circular coils and 1.78 $^{\circ}C/(kW \cdot s)$ for the circular coils. In other words, with 1000 $W \cdot s$ input energy dissipated in the system, the plate's temperature increases by 2.81 $^{\circ}C$ on average when four of the proposed outer squircle-inner circular coils are driven with the 180° phase difference. Similarly, with 1000 $W \cdot s$ input energy, the plate's temperature increases by 1.78 $^{\circ}C$ on average when four of the conventional circular coils are driven with the 180° phase difference. Heating enhancement obtained in four coils measurements for the proposed outer squircle-inner circular shape coils compared to the circular coils is higher than heating enhancement obtained in measurements of pairs of the coils. It is an expected result. However, average temperature increase speeds of 2.81 $^{\circ}C$ and 1.78 $^{\circ}C$ for the four of the outer squircle-inner circular coils and the circular coils are considerably lower than temperature increase speeds of 3.73 $^{\circ}C$ and 3.48 $^{\circ}C$ that were calculated for pairs of the outer squircle-inner circular coils and the circular coils, respectively. This might be due to the fact that the load plate with 180 mm diameter completely covers two side-by-side placed coils, whereas it does not completely cover four of the side-by-side placed coils.

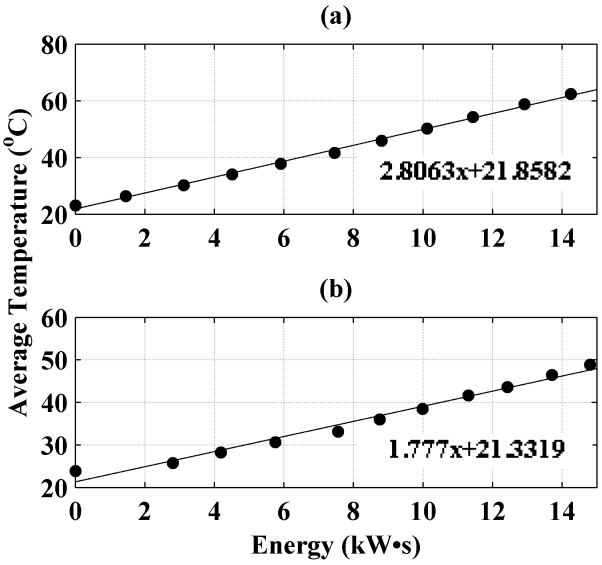

Figure 3.23: Average temperature increase over the plate as a function of the energy supplied to and dissipated in the system. Here the plate was placed above (a) four of the outer squircle-inner circular coils driven with 180° phase difference and (b) four of the circular coils driven with 180° phase difference.

In Figure 3.24 temperature distributions on the plate with equal amount of energies supplied to and dissipated in the systems are represented. In the first system (Figure 3.24(a)), four outer squircle-inner circular coils are driven with the 180° phase difference and in the second system (Figure 3.24(b)) four circular coils are driven with the 180° phase difference.

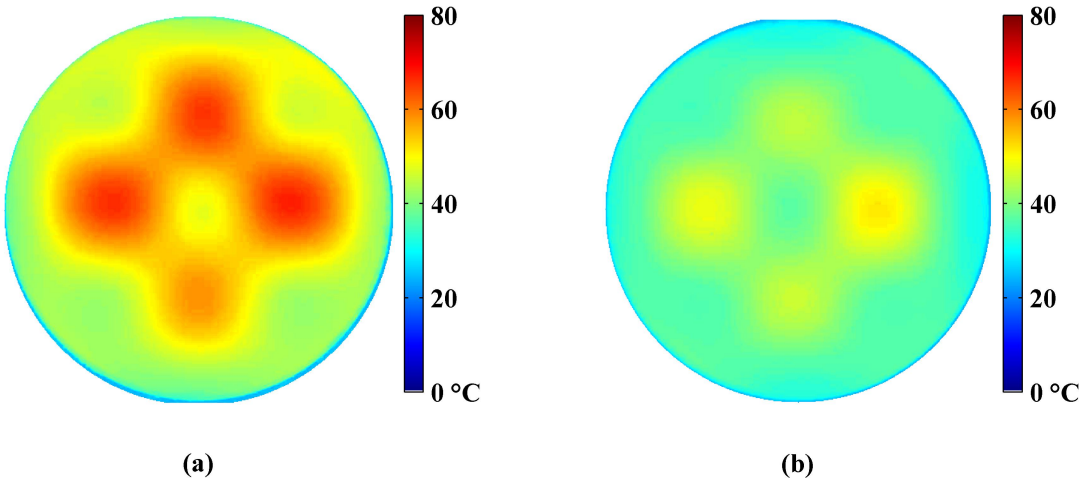

Figure 3.24: Temperature distributions on the stainless steel plate with a total supplied real energy of approximately 10 $kW \cdot s$: for (a) four of the outer squircle-inner circular coils placed tangentially in 2D square lattice and driven by the 180° phase difference and (b) four of the circular coils placed in 2D square lattice and driven by the 180° phase difference.

In addition, for comparison purposes, temperature increase of the plate for the systems is presented in Figure 3.25 and Figure 3.26 across horizontal and vertical fixed lines those pass through the center of the plate. Temperature increase is the difference between the plate temperature after 10 $kW \cdot s$ total real energy was supplied to the system and its initial temperature when no energy was supplied. In the figures, labels S180 and C180 correspond to the systems in which four outer squircle-inner circular coils are driven with the 180° phase difference and four circular coils are driven with the 180° phase difference, respectively.

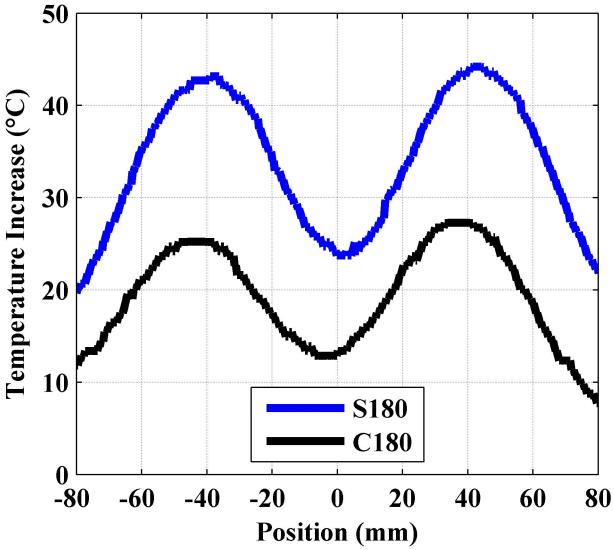

Figure 3.25: Temperature increase on constant horizontal line that passes through the middle of the plate. Here approximately 10 $kW \cdot s$ total real energies are supplied to the systems.

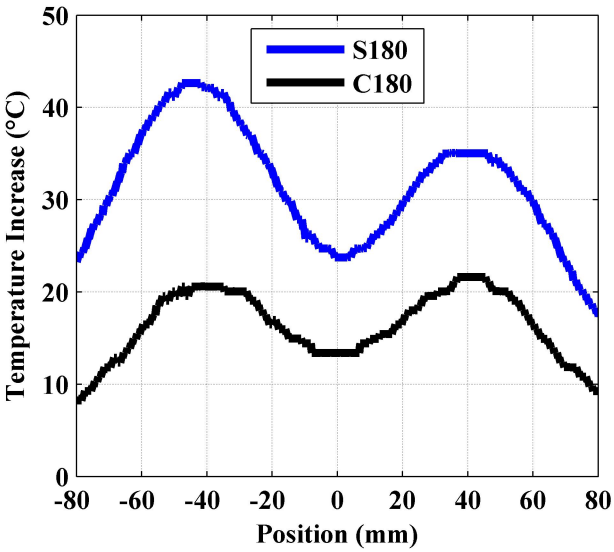

Figure 3.26: Temperature increase on constant vertical line that passes through the middle of the plate. Here again approximately 10 $kW \cdot s$ total real energies are supplied to the systems.

In the figures, it is clearly seen that the temperature increase on the plate is higher in systems where newly designed outer squircle-inner circular coils were used instead of the conventional circular coils. Since the total real energy supplied to the system is constant, similar trends are expected to be observed for the energy transfer ratio.

3.3.3 Summary

In this section, heating efficiency of the system composed of a stainless steel (AISI 430) plate having cylindrical shape with 180 mm diameter and 1 mm thickness, ferrite layers and four outer squircle-inner circular coils aligned tangentially in a 2D square lattice is measured for 0° and 180° phase differences between adjacent coils. Experiments were repeated with four circular coils, which are again placed side-by-side in a 2D square lattice. Heating efficiency and speed of the systems were comparatively measured. In 180° phase difference applications, plate heats up starting from regions above close sides of the coils. On the other hand, in 0° phase difference applications, temperature of the plate is highest in the areas above the furthermost corners of the coils. In both phase difference applications, temperature of the plate at its center is low. In 180° phase difference applications this is because of undesirable coupling between diagonal coils. To decrease such undesirable destructive coupling we proposed to use coils with outer squircle geometry.

In system measurements, heating efficiency enhancement ratio obtained with four outer squircle-inner circular coils with respect to four circular coils is higher than heating efficiency enhancement ratio obtained with a pair of the outer squircle-inner circular coils with respect to a pair of the circular coils. It is an expected result because in the system, where four coils are aligned in a 2D square lattice and 180° phase difference is applied between the consecutive coils, each coil interfere constructively with other two coils those are next to it. Since the outer squircle-inner circular coils have longer tangential sides than the circular coils, their interactions and couplings are higher.

On the other hand, in four coils experiments, temperature increase speed calculated as a function of real power supplied to and dissipated in a system was found to be lower than that calculated in double coil measurements. One of the reason of this unexpected result is that in four coils experiments used plate with 180 mm diameter does not completely cover the coils.

Chapter 4

Space-Invariant All-Surface Inductive Heating at a Constant Speed Enabled by Tangent Squircle Coils in Square Lattice

As we briefly described in the introduction chapter, to model an all-surface inductive heating system we placed nine of the manufactured outer squircle-inner circular coils in a two-dimensional (2D) 3×3 array and obtained heating measurements with a plate positioned at different locations on the hob surface. In addition, we conducted three-dimensional (3D) electromagnetic (EM) simulation to verify and explain the measurement results. About this work, we prepared a manuscript that is in submission [12]. The manuscript summarizes the results and constructs the frame of this chapter.

4.1 Motivation

In all-surface induction hobs, an array of small coils is used. Working principle of all-surface induction relies on detecting a vessel and powering only the corresponding coils loaded by the vessel. For driving these coils in an efficient way, different control topologies have been reported [46]-[48]. However, most of these all-surface designs [28, 49] employ arrays of the conventional circular coils. Coils with different shapes including square and rectangular coils have also been considered for all-surface inductive heating [39]. As we have demonstrated and explained in detail in the previous chapter, interaction between coils having rounded shapes is not as strong as that between square or rectangular coils [11]. Although such strong interaction between side-by-side placed coils is highly desired for efficient all-surface heating, destructive coupling between diagonally located coils is undesired. As a result, space variance of heating on an all-surface induction hob remains unelucidated today.

In the previous literature, to the best of our knowledge, there have been no reports investigating the inductive heating of a load placed at various locations on a hob surface. To this end, we systematically studied an all-surface inductive heating system and comparatively measured the heating efficiency and speed of the system for all possible loading positions. With our proposed system design, space-invariant all-surface inductive heating at an almost constant speed and efficiency level is demonstrated.

Here we designed, constructed and characterized our all-surface inductive heating system made of squircle coils tangentially placed in a 2D square lattice. We experimentally compared the heating speed of this system in time and as a function of dissipated energy for a plate placed at various locations on the surface. This system is proved to heat loads all over its surface with a constant speed independent from the load position.

4.2 Design and Experimental Setup

We used coils that we prepared in the outer squircle-inner circular architecture. In the system, we aligned the coils in a square lattice creating a 180° phase difference between consecutive coils during system construction by simply reversing tips of the coils and allowing current flows to be in opposite directions. As a result, in operation, in one coil current flow is in clockwise direction and in the neighbor coil it is in counterclockwise direction, or vice versa. Figure 4.1 shows our 3×3 tangent coil array structure in square lattice alignment from perspective view together with its geometrical parameters.

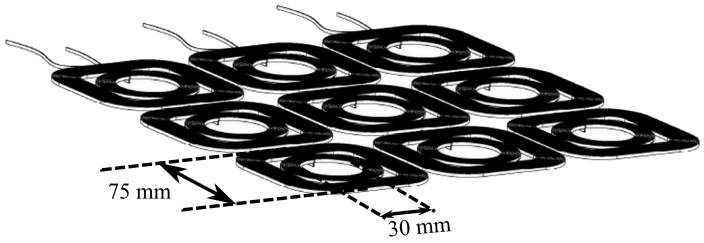

Figure 4.1: Perspective view of the 3×3 tangent outer squircle-inner circular coil array structure in square lattice alignment and the coil's geometrical parameters.

Figure 4.2 shows a photograph of a single coil unit from top view. In this coil, after 26 turns, squircle windings at the outer rim evolve into fully circular inner turns, which is the same structure as in Figure 3.1(b) in the previous chapter where the phase difference effect between only two and four of them is investigated [11]. Here we built 9 of these coils to study the space variance of inductive heating in an array. For this purpose, 9 of these units are placed tangentially in 2D square lattice to construct the 3×3 coil array structure. Here, with long tangential sides the outer squircle windings enhance couplings between side-by-side placed coils in the array. Side-by-side placement of coils in close packing increases constructive coil interactions, especially when 180° phase difference is applied. However, in the square lattice diagonal coils have in-phase currents both for 0° and 180° phase difference applications. Rounded corners of the squircle geometry thus make diagonal coils farther away from each other and decrease

their destructive coupling. In the manufacturing stage, the outer squircle-inner circular shape planar coils are sandwiched between two mica layers. Since mica is resistant to high temperature, it is commonly used in such heating applications. The upper mica layer can be seen in the figure. In our prototype, the mica layer has a thickness of 0.40 mm. Also, there are ferrite sticks placed symmetrically around the coil center with 45° angular intervals between two consecutive sticks below the bottom mica layer, which are used for efficiency enhancement. Ferrites speed up the vessel heating by reversing the magnetic flux produced by the coils in lower half space [27, 43].

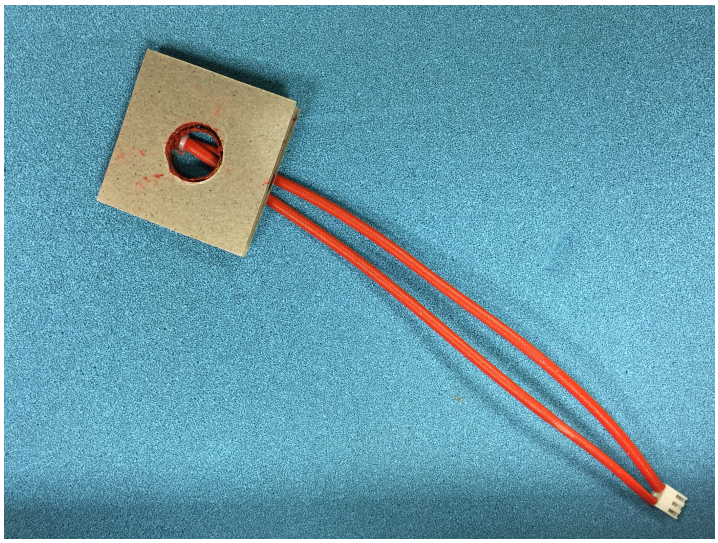

Figure 4.2: Photograph of a single coil designed as a repeating unit in the 3×3 coil array system from top view.

In our system the coils are placed as close as possible with 5 mm distances between them. The distance between the coils arises because of the constant side lengths of the hob surface. Heating surface is desired to be uniformly occupied by the coils but number of the coils is limited by the power circuitry. A steel plate (AISI 430) is placed above the coils. It is the same with that we used before in heating experiments. The plate has a cylindrical shape with 180 mm diameter and 1 mm thickness. It is important to set the plate's diameter to be equal to or larger than the side length of the repeating unit in the coil array, which is 80 mm (75 mm + 5 mm) here, for catching hot and cold spots. Hot and cold spots

occur as a result of constructive and destructive coupling of the coils, respectively. Also, the distance between the plate's bottom surface and the coil units is set to 8 mm to model the thermal isolation material (such as Silargan glass) on the hob surface. A schematic of the designed system from side view together with its geometrical parameters is illustrated in Figure 4.3.

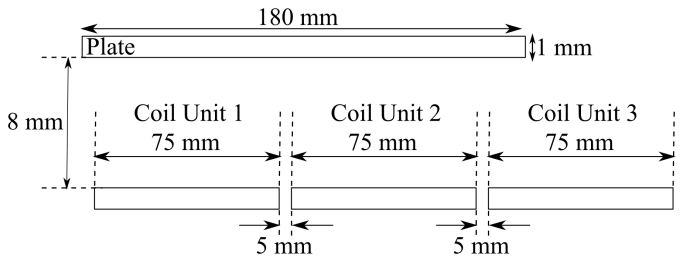

Figure 4.3: Schematic of the designed system from side view together with its geometrical parameters. To reflect ratio between the coils' and the plate's sizes more clearly, here plate is located to cover two coil units completely.

Projection coverage of the coils by steel plate depends on the plate position. Therefore, different coils might be powered up and heating of the plate may differ depending on its location on the hob surface. To observe these variations, measurements were conducted for the plate's six different placements. Positions of the plate's center with respect to coils for these six scenarios are shown in Figure 4.4.

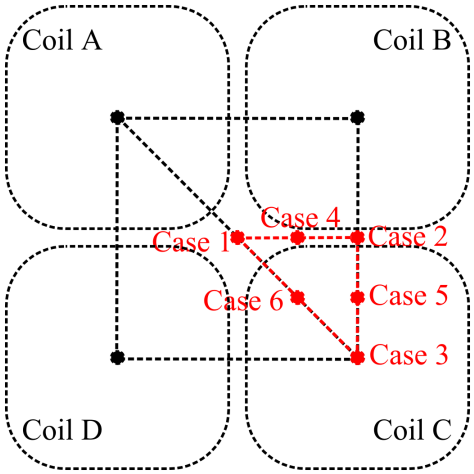

Figure 4.4: Plate's center positions with respect to coils for six different measurement scenarios.

In the figure, positions of the plate's center for six different cases are marked with red dots. In Case 1 and Case 2 plate is located to be in the middle of the Coil A - Coil C and Coil B - Coil C pairs, respectively. Also, in Case 3 plate's center and the center of the third coil (Coil C) are on top of each other. In other cases, i.e., Case 4, Case 5 and Case 6, plate's center is positioned to be at the middle of the positions in Case 1, Case 2 and Case 3. Because of symmetry only four coils are represented. Note that coils are aligned tangentially in square lattice thus coil centers construct a square. Similarly, points indicating positions of the plate's center for measurement cases construct a triangle. Again, because of symmetry other measurements outside the red triangular area would yield similar results. Here, the highest distance between two consecutive positions of the plate's center is approximately 28.28 mm (distances between Case 1 - Case 6 and Case 3 - Case 6). The number of measurement scenarios can be increased further. However, results obtained with the new scenarios would be amid the results of the six cases mentioned above (Case 1, Case 2, Case 3, Case 4, Case 5 and Case 6). Also, the distance between the plate's center positions in possible new scenarios and in the existing cases can be 14.14 mm at maximum. This distance is very small compared to the plate's diameter. Therefore, six measurement scenarios are enough to understand the plate's heating variation with its position. For

each case, areas of the coils covered by the plate were calculated. Based on L-R measurements data, which we obtained and reported in Sensors Journal [13] and explain in the next chapter, for vessel detection, coils whose at least 30% of the area is covered by the plate were decided to be powered up. Figure 4.5 shows placements of the coils and the plate for all the measurement cases showing turned-on and turned-off coils. In the figure, the plate's circumference and center are represented with black circle and x marker, respectively. Similarly, on- and off-coils are pointed out with red and blue colors, respectively.

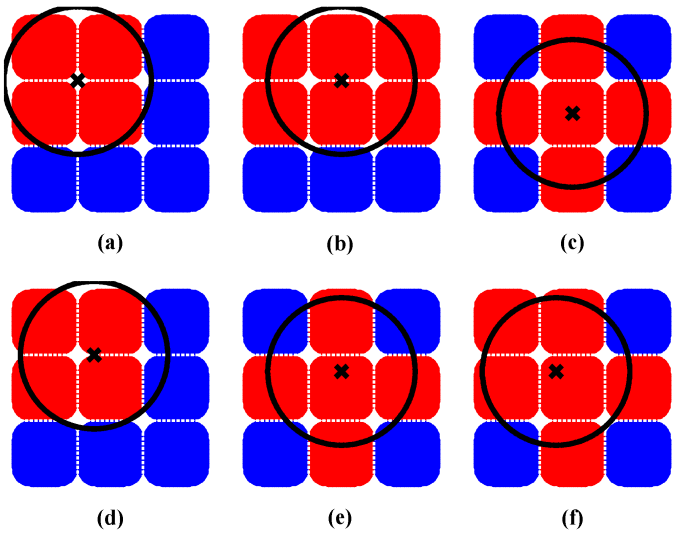

Figure 4.5: Placements of the plate and the coils that are on and off in six different scenarios. Here, (a), (b), (c), (d), (e) and (f) subtitles correspond to Case 1, Case 2, Case 3, Case 4, Case 5 and Case 6 in Figure 4.4, respectively. The red coils correspond to the turned-on ones, and the blue, to the turned-off ones.

For each case in Figure 4.5, measurements were repeated. Corresponding coils were driven by half bridge supply circuitry at a frequency of 50 kHz. Total real power supplied to the coils, which is the true power, was measured by means of an oscilloscope (Agilent DSOX3012A) on which current and voltage signals were recorded with help of a current clamp and a voltage probe, respectively. The

power calculation is given by equation (4.1).

$$P_{rms} = |V_{rms}||I_{rms}|cos(\phi) \tag{4.1}$$

Here P_{rms} is the true rms power (W), V_{rms} and I_{rms} are the rms voltage (V) and current (A), respectively. Also, ϕ is the phase difference between the voltage and current signals.

We calculated the plate's temperature change with total dissipated energy in the system. Total dissipated energy in the system is found by taking integral of the total instantaneous true power over time. Relation between the dissipated energy and the true power is given by equation (4.2)

$$E_{total} = \int P_{rms} \cdot dt \tag{4.2}$$

where E_{total} is the total dissipated energy in the system (J) and P_{rms} is the instantaneous true power supplied to the coils (W).

The plate's temperature was measured and recorded using a thermal camera (FLIR A655sc). Temperature distribution over the plate's top surface was instantaneously measured. Since temperature distribution is not uniform, we calculated the plate's average temperature by integrating the temperature distribution over the top surface and divided the result by the surface area. Because its thickness is so thin (1 mm), in the calculation temperature gradient between the plate's bottom and top surfaces is ignored.

4.3 Results and Discussion

Measurements were conducted for each case. In all experiments 180° phase difference was applied to consecutive coils. For instance, in Case 1 (Figure 4.5(a)) among four working coils two diagonally located coils have currents flowing in one (e.g., in clockwise) direction and the other two cross coils have currents flowing in the opposite (e.g., in counter clockwise) direction. Heating of the plate was observed with help of the thermal camera. As an exemplary, Figure 4.6 shows the

temperature distributions over the steel plate's top surface (at 55 s after power was turned on) for all the cases.

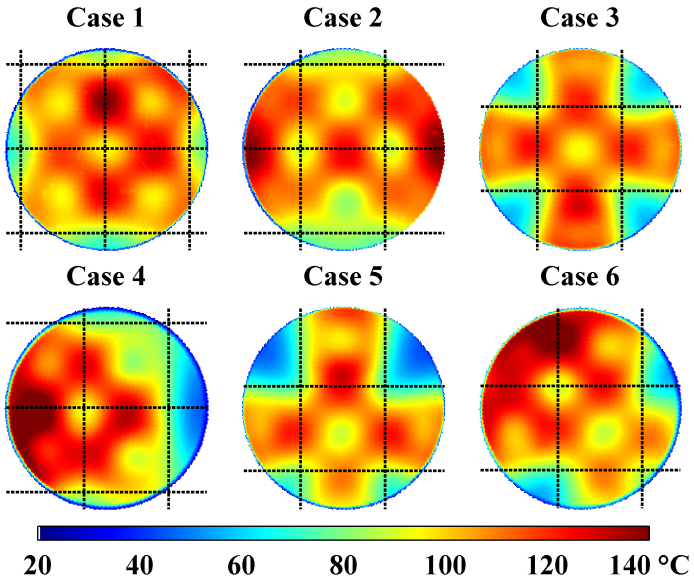

Figure 4.6: Temperature distributions over the plate's top surface at 55 s after the power was turned on for all the cases.

In the figure, to represent coil locations, boundaries between the coils are marked with dotted lines. As seen, the plate is heated starting from the regions above the adjacent coils' close sides. This is because of the 180° phase difference between the consecutive tangential coil currents. On the other hand, temperature increases are slower in areas above the coils' corners, where cross coils are being the closest. This is because of cross coils' having currents in the same direction, i.e., 0° phase difference between. This is one of the reasons why outer rim of the coils were selected to be squircle shape instead of square. By rounding corners of the square shape, destructive interaction between cross coils is aimed to be decreased. In the figure, temperature distributions obtained in Case 1, Case 2 and Case 3 are almost symmetric with respect to the plate's center. This is expected and based on the plate's placements with respect to the on-coils such that the plate is located in the middle of the four adjacent tangential on-coils in Case 1, six neighbor tangential on-coils in Case 2 and five symmetric and adjacent tangential

on-coils in Case 3 (see Figures 4.5(a), (b) and (c)). Small heating variations that violate complete symmetry, such as the high temperature area between the two adjacent tangential upper coils in Case 1, are due to measurement error of the plate's not being completely parallel to the coils' top surfaces. Coupling between a coil and a load is strongly related with their separation. In the system since coils and the plate are close to each other only with 8 mm distance, small changes in the coil-plate separations violate absolute symmetry.

Figure 4.7 shows changes of average temperature over the plate with time. The nonzero initial times in the figure are because of the time required for the thermal camera's connection and taking of the image.

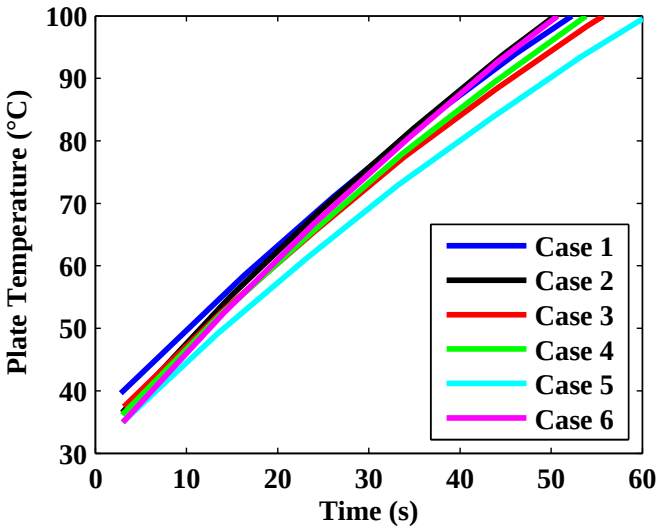

Figure 4.7: Average temperature changes over the plate with time for all the measurement cases.

In our measurements, the plate was heated up till its average temperature passes 100 $°C$. In the figure, at high temperatures more time is required to heat up the plate further. In other words, temperature increase decelerates as time goes on. This can be explained with high temperature gradient between the plate and the medium, which causes rapid cooling of the plate. In addition, in Figure 4.7 plate's heating speed is very similar for all the cases. It is important for comparison of the system's heating efficiencies with a plate at different positions.

However, heating speed depends on supplied power, too. Therefore, change of the plate's temperature with total dissipated energy in the system was calculated and is presented in Figure 4.8.

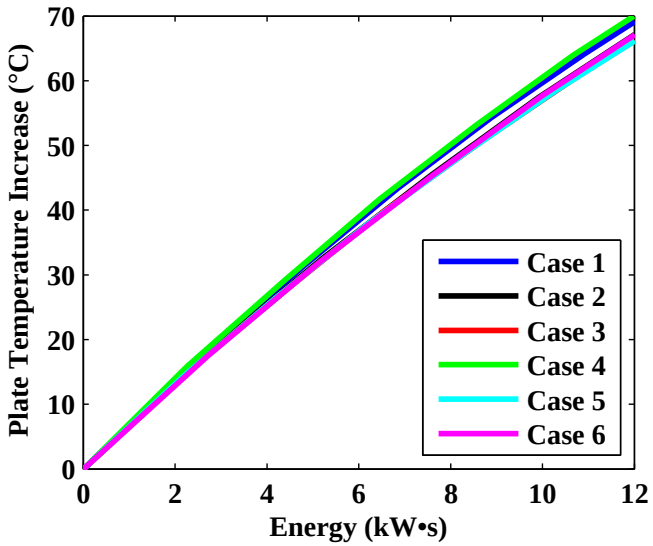

Figure 4.8: Average temperature changes over the plate with total dissipated energy in the system for all the measurement cases.

Heating is almost the same for all the cases in the figure. This is expected because real power was supplied to the coils in a close range in all the measurements. Also, in the figure decrease in the plate's heating speed is observed, too. Figure 4.9 shows change of the plate's heating speed with its temperature for all the measurement cases. Heating speed is calculated by taking slope of the curves in Figure 4.8.

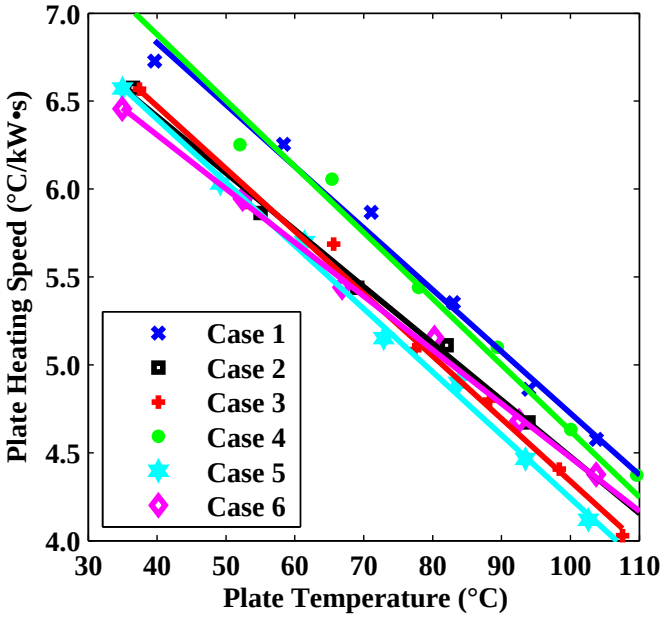

Figure 4.9: Change of the plate temperature increase speed in the system with the plate temperature for all the measurement cases.

Here markers denote the calculated heating speeds and lines are the corresponding first order fittings. In the figure, decrease in the plate's heating speed is clearly seen. For instance, with 1 $kW \cdot s$ input energy the plate's temperature increased more than 6.0 $^{\circ}C$ if its temperature was around 40 $^{\circ}C$, but if its temperature was around 110 $^{\circ}C$ than with 1 $kW \cdot s$ input energy the plate's temperature increased at most 4.5 $^{\circ}C$ in our system. In addition, in the figure at a constant plate temperature the difference between temperature increase speeds for the cases are at most 0.6 $^{\circ}C/(kW \cdot s)$. This is expected from Figure 4.8 and supports the result of space-invariant heating of the system.

Plate's similar heating for all the cases in Figure 4.8 indicates that the system's heating efficiency and speed are independent of the plate position. In other words, the proposed all-surface inductive heating system heats a vessel efficiently and quickly all over its surface.

We further investigated the power dissipation in our half-bridge supply circuitry by measuring real powers supplied to each coil and extracting their sum from the true power supplied to and dissipated in the whole system. The average real powers supplied to each coil and the power dissipated by the supply circuitry over 50 seconds are given in Table 4.1 together with total power dissipated in the system for the first three cases.

Table 4.1: Average real powers supplied to and dissipated by the coils, supply circuitry and the whole system.

	Case 1	Case 2	Case 3
Coil 1	33.14 W	20.50 W	X
Coil 2	32.31 W	38.20 W	21.96 W
Coil 3	X	15.71 W	X
Coil 4	35.45 W	19.36 W	21.95 W
Coil 5	32.02 W	39.28 W	42.66 W
Coil 6	X	18.05 W	20.37 W
Coil 7	X	X	X
Coil 8	X	X	19.84 W
Coil 9	X	X	X
Supply Circuitry	72.45 W	85.66 W	86.50 W
Whole System	205.37 W	236.76 W	213.28 W

In the table off-coils are indicated with X. Also, coils are called starting from left top towards the right bottom in ascending order. For instance, the left top coil in Figure 4.5 is called Coil 1. Similarly, the right top, the left bottom and the right bottom coils are called Coil 3, Coil 7 and Coil 9, respectively, in the table.

As seen, power loss in our supply circuitry was found around 80 W. This is almost 1/3 of the total power dissipated in the whole system. Therefore, system efficiency can be enhanced further with a developed supply circuit. Also, as expected, powers supplied to the coils in each case are proportional with their loadings. For example, in Case 1 supplied powers to the coils are almost the same because of their equal loading by the plate. Similarly, supplied powers to Coil 2

and Coil 5 are the highest in Case 2 because they were covered by the plate most largely. Again, Coil 5 was covered by the plate most largely and thus its supplied power is the highest in Case 3.

Experiments were repeated at different frequencies and similar results were obtained. However, at low frequencies circuit losses in the supply circuit are less. Therefore, low operation frequencies might be a better choice.

Furthermore, for comparison purpose we studied the system using full three-dimensional (3D) electromagnetic solutions. To construct the same setup in the numerical simulations with those in the measurement cases, we first found the average currents supplied to the coils from measured current signals. For the first three cases, i.e., Case 1, Case 2 and Case 3, variations of the measured currents on the coils are shown in Figure 4.10.

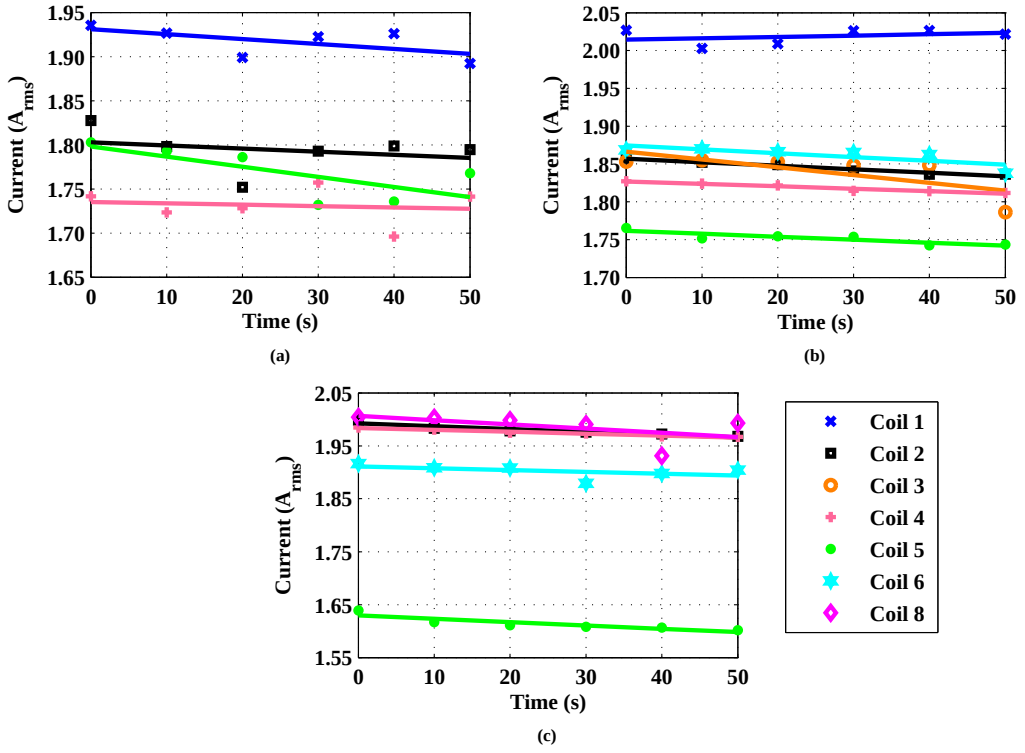

Figure 4.10: Variations of the measured currents on the coils with time for three different scenarios: (a) Case 1, (b) Case 2 and (c) Case 3.

In the figure, currents on the coils are almost constant in time. Therefore, the used supply circuitry behaves as a current source. The currents supplied to the coils on average are given in Table 4.2. Similar to Table 4.1, here off-coils are again indicated with X.

Table 4.2: Average currents supplied to the coils.

	Case 1	Case 2	Case 3
Coil 1	1.92 A	2.02 A	X
Coil 2	1.79 A	1.85 A	1.97 A
Coil 3	X	1.84 A	X
Coil 4	1.73 A	1.82 A	1.97 A
Coil 5	1.77 A	1.75 A	1.61 A
Coil 6	X	1.86 A	1.90 A
Coil 7	X	X	X
Coil 8	X	X	1.98 A
Coil 9	X	X	X

In our simulations, each coil was driven by a separate current source with the specific amplitude given in Table 4.2. Total power transferred to and dissipated on the plate was calculated as 130.37 W, 161.52 W and 148.49 W for Case 1, Case 2 and Case 3, respectively. On the other hand, in Table 4.1, total powers supplied to the coils, which are the total dissipated powers in the coils and the plate, were found as 132.92 W (205.37 W - 72.45 W), 151.10 W (236.76 W - 85.66 W) and 126.78 W (213.28 W - 86.50 W). As seen, the calculated powers in the simulations and the measured powers in the experiments are close to each other.

4.4 Summary

In this study a new all-surface induction hob design is introduced. In proposed system, an array of tangential outer squircle coils is aligned in a 2D square lattice. For plate's various placements heating speed of the design was measured and

results were compared. In experiments, plate's heating with an almost constant speed in time was obtained for the plate's various positions on the hob surface. In addition, plate's temperature increase speed was calculated as a function of dissipated energy in the system. Plate's temperature increase with total dissipated energy was found almost the same for all the cases, where difference between the temperature increase speeds for the used plate at a constant temperature was calculated to be at most 0.6 $^{\circ}C/(kW \cdot s)$. Results indicate that the heating speed and efficiency of the proposed system are independent from the plate's location on the hob surface. Moreover, in experiments, plate's heating speed was observed to be decelerated with its temperature, which is expected from the increased temperature gradient between the plate and the medium. Also, for different cases powers supplied to and dissipated on each coil were measured. In the system, true powers supplied to the coils are shown to be proportional with their loadings. The results were verified with full 3D electromagnetic simulations. This study is beneficial for all-surface induction hobs in terms of demonstrating its feasibility. Also, space-invariant heating all over the surface at a constant speed is one achievement that was not reported before.

Chapter 5

Wireless Metal Detection for All-Surface Inductive Heating

Another topic that we have interested in and have studies on is vessel detection process in induction hobs. In conventional induction heaters, proposed methods are able to determine presence of loading of a coil. These methods rely on the fact that coil's loading changes with vessel's size and placement. Therefore, according to changes in loading, coil is turned on and off. However, proposed methods are not able to determine vessel's exact location as well as its material. It is one of the issue important especially for all-surface inductive heating. In addition, there are no works in literature about vessel detection in all-surface induction hobs. In all-surface induction hobs, for efficient heating only the coils those are loaded by a vessel are necessary to be powered up with predetermined magnitudes. For this, in an induction hob vessel's location and its material should be identified. To overcome this problem, we have introduced a method that determines exact location of a vessel together with its material in an all-surface induction hob. We have conducted various measurements with conventional circular and our designed outer squircle-inner circular coils. Experiments and results are described below in detail. Validity of this process was approved by our partner Arcelik A.S., too. Part of this study that is about experiments using a circular coil, has been published in Sensors Journal [13]. Also, another part was submitted to AIP

Advances journal as a contributed paper, published as part of the Conference on Magnetism and Magnetic Materials to AIP Advances [14]. This chapter is partially taken from these reports of ours [13, 14].

5.1 Motivation

In regular induction hobs, large coils are placed beneath the hob surface at specified locations. In these heating systems, for efficient heating vessels should typically have similar sizes with those of the coils and they should be placed right on top of a coil. To overcome these issues, induction hobs with an array of small-area coils have been proposed. Thanks to the array structure, efficient heating of vessels with different shapes and sizes located anywhere on the hob might be possible. Therefore, a very recent important implementation in induction hobs is all-surface heating.

In all-surface induction hobs, location of the vessel should be identified together with its size in order to power up the corresponding coils for efficient, safe, and low-cost heating. In commercial induction hobs, pan detection is made using the damping factor measurement [50]-[52]. In these systems, if a coil is not loaded, then long oscillation signals are detected. On the other hand, if the coil is loaded with a metal vessel, then a few-cycle damped oscillation signal is observed. This method is useful for detecting the vessel presence. However, this approach cannot specify the vessel's exact position on the surface of the hob or its material.

Since an all-surface induction hob is a radically new topology, there are no previous reports in the literature addressing the problem of metal coverage sensing to identify which coils to be powered up in all-surface induction for efficient heating. To this end, we propose and demonstrate a simple and robust solution that provides us with the ability to detect the vessel presence while uniquely sensing its surface coverage and identifying its effective material type at the same time in all-surface inductive heating systems. Here, we systematically study variations in the inductance and resistance of an all-surface induction coil coupled

to a metal plate at different locations with different coverage areas. In this study, we obtain maps of the magnitude and angle variations in the coupled system's impedance. Although some previous reports discuss variations of inductance and resistance of a coil in an induction heater for heating measurements [53, 54], our work is the first account of the proof-of-concept demonstration of wireless metal detection and surface coverage sensing independent of the metallic vessel material type in all-surface inductive heating, which is essential to determining the vessel coverage by each coil for powering and obtaining the information of the vessel material and size for efficient heating.

5.2 Experimental Setup

In our experimental study, a plate was used to be placed over a conventional circular coil and a designed outer squircle-inner circular coil, respectively, and moved around horizontally without changing its perpendicular distance to the coil. Inductance and resistance values of the studied coil were measured for each position of the plate at two different frequencies (20 and 100 kHz) (by means of an LCR meter Agilent 4263B). Measurement setup is shown in Figure 5.1. In experiments while the coil was immobile, the plate was systematically shifted on the x-y plane with the help of a computer-controlled mechanical stage. As a result, the changes of inductance and resistance values with the coil-plate distance were measured and their changes with an area of the coil covered by the plate were calculated.

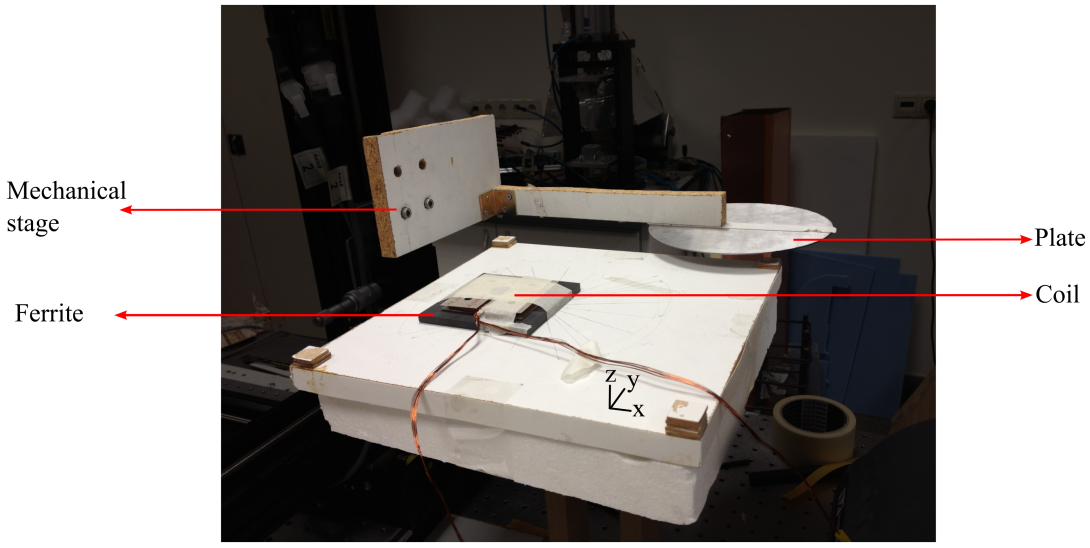

Figure 5.1: Measurement setup and its parts, where components are pointed out and indicated with red arrows.

Similarly, a side-view of coupled system is sketched with its geometrical parameters in Figure 5.2. As represented in the figure, the coupled system is constructed by a coil, a plate and a ferrite layer below the coil. The plate is a disk with a diameter of 180 mm and a thickness of 1 mm. They are the same with those of the plate we used in our heating experiments. The diameter of this plate is in the standard range of vessel dimensions, and it is selected to be larger than that of the coil to model coil array heating in all-surface application. The distance between the coil and the plate (h1) was set to 8 mm, which is similar to the typical thickness of a glass ceramic surface in conventional hobs. During characterization, the plate was scanned across the planar surface 8 mm above the coil. Similarly, the distance between the ferrite layer and the coil (h2) was set to 0.4 mm. This is because of the substrate (mica) layer used in the manufacturing of the coil. Another mica layer exists on top of the coil as well, but its thickness was included in h1.

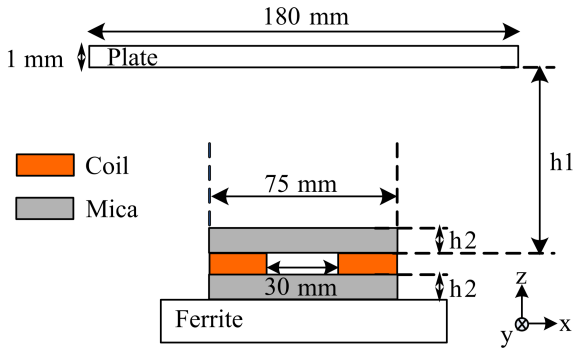

Figure 5.2: Coupled system from side-view together with its geometrical parameters.

Because vessels used in daily life are made of various materials, measurements were repeated with stainless steel (AISI 430) and aluminum plates. These materials were selected due to their opposite properties effective on the induction heating process. In contrast to aluminum's very low magnetic permeability and electrical resistivity, stainless steel has huge permeability and relatively high resistivity. Although aluminum is not a proper vessel material to be used in induction heating, stainless steel is one of the most appropriate vessel materials. Therefore, the measurements were done with one of the most and one of the least proper vessel materials.

5.3 Experiments with Circular Coil

We first had measurements with a circular coil. It has exactly the same structure with that of the circular coil used in heating measurements as a comparative structure for the designed outer squircle-inner circular coils. More precisely, the coil used in these measurements has a conventional circular shape with a 75 mm outer diameter and a 30 mm inner diameter. It consists of 44 circular turns in total and, in each turn, 13 copper wires with 0.25 mm diameter exist. Coil structure is shown in Figure 5.3.

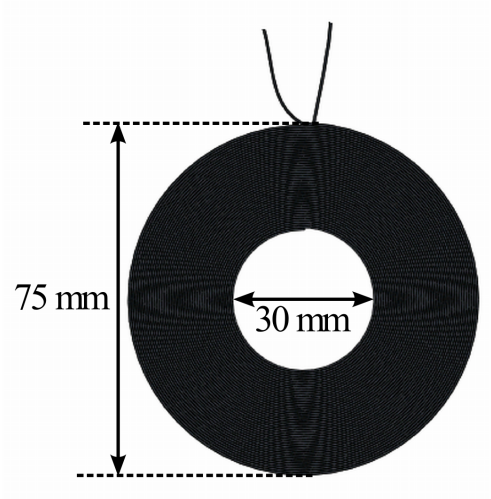

Figure 5.3: The circular coil structure used in measurements and its geometrical sizes.

First, the measurements were obtained using a stainless steel plate. Mappings of the system's inductance and resistance values while the plate is scanned across at 20 kHz are depicted in Figure 5.4. In the figure, each point represents the center-to-center distances between the plate and the coil projections on the plane and the color bar data correspond to the measured resistance and inductance values.

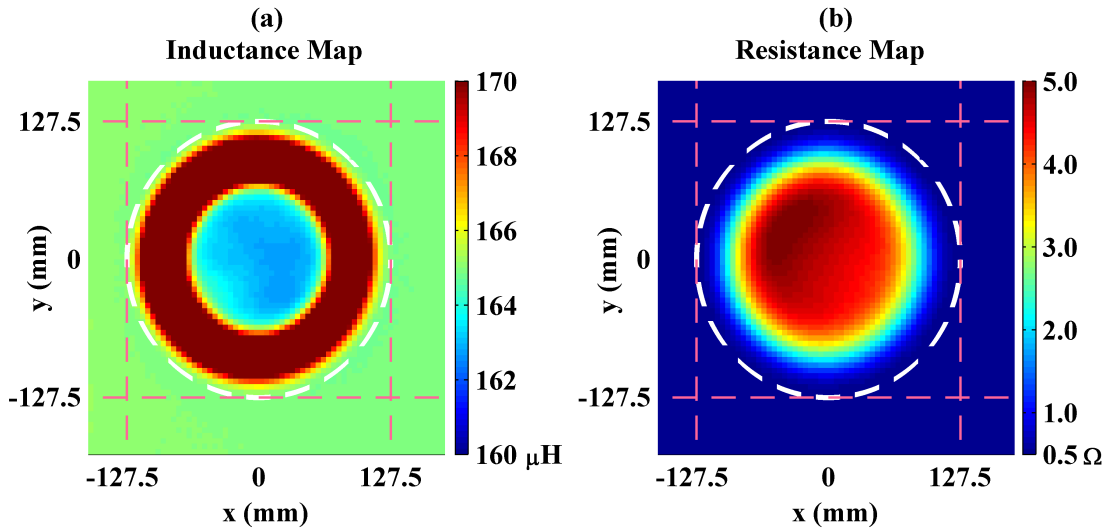

Figure 5.4: Measured inductance (a) and resistance (b) maps for the system where the coil is loaded by the steel plate as a function of its lateral position at a horizontal plane 8 mm above the coil. Here, the coil is centered at the (0,0) origin. In addition, the white dash circles represent the points where the coil and the plate projections are tangential. End points of the circles are pointed out with pink ticks at -127.5 mm and 127.5 mm on the x and y axis.

Inductance of the unloaded coil is around 165 μH (see Figure 5.4(a)). However, as the plate and the coil centers get closer, the system's equivalent inductance first increases and then decreases. Normally, monotonic decreasing with coverage area is expected because of enhancement in coupling. The reason for unexpected inductance increase is induced currents on the top surface of the plate that are in reverse direction with currents on the bottom surface. In the case where the coil is partially covered, looping magnetic fields produced by the coil create such reverse currents on the plate's top surface. In addition, bending of the induced currents on the bottom surface of the plate causes reverse currents. Since stainless steel has a huge permeability, the magnetic flux produced by the coil induces eddy currents not on the plate's top surface but on its bottom surface. However, as the plate moves out of the coil's projection, the induced currents on the bottom surface goes through the plate's side edges and flows on the top surface as well. These currents on the bottom and top surfaces are in reverse directions and thus they construct

a complete loop. The induced current distribution on the steel plate's bottom and top surfaces were calculated using 3D full electromagnetic solutions for the plate's various positions. Calculated tangential current amplitude distributions are shown in Figure 5.5, Figure 5.6 and Figure 5.7.

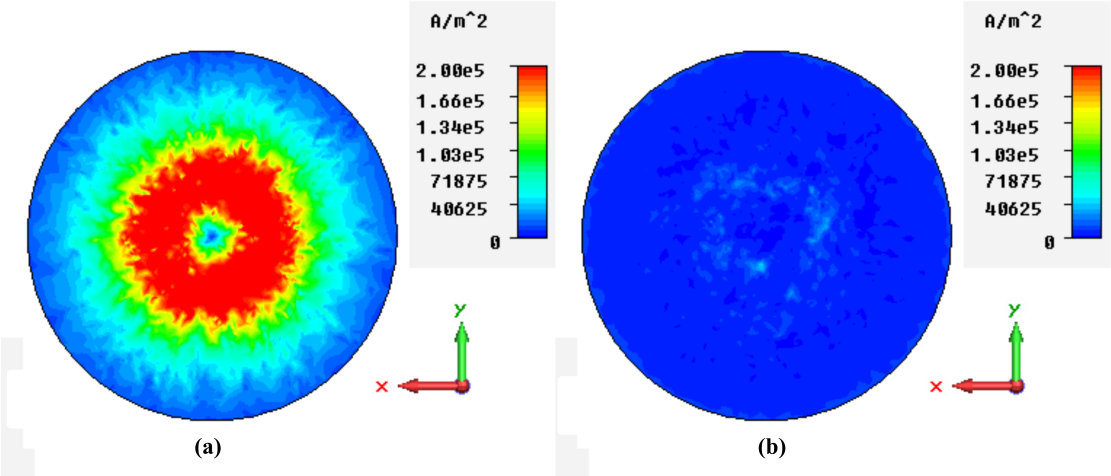

Figure 5.5: (a) Tangential current amplitude distribution on bottom surface of the steel plate; and (b) on top surface of the steel plate. Here, the plate and the coil centers coincide, i.e., the coil is covered by the plate's projection completely.

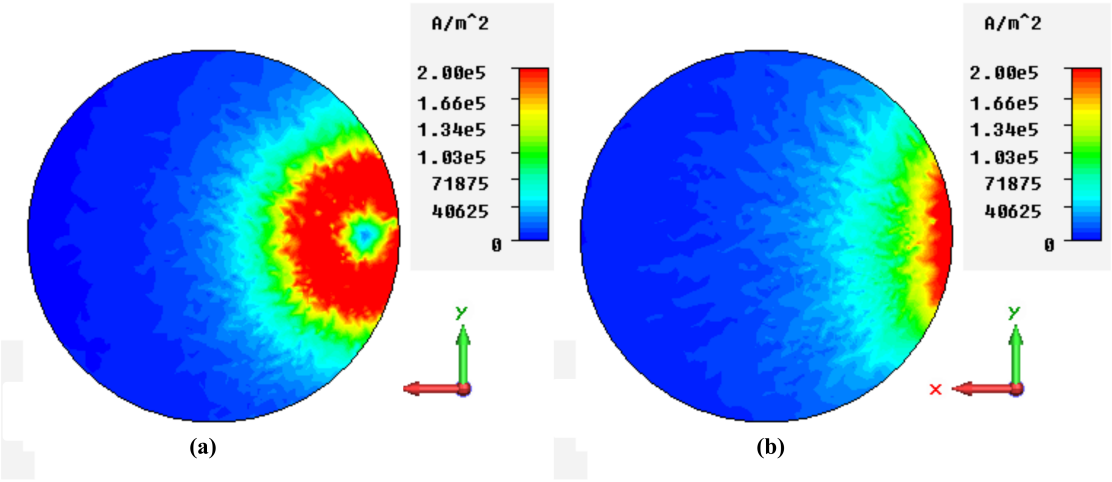

Figure 5.6: (a) Tangential current amplitude distribution on bottom surface of the steel plate; and (b) on top surface of the steel plate. Here, horizontal distance between the plate and the coil centers is 75 mm, i.e., approximately 70% of the coil is covered by the plate's projection.

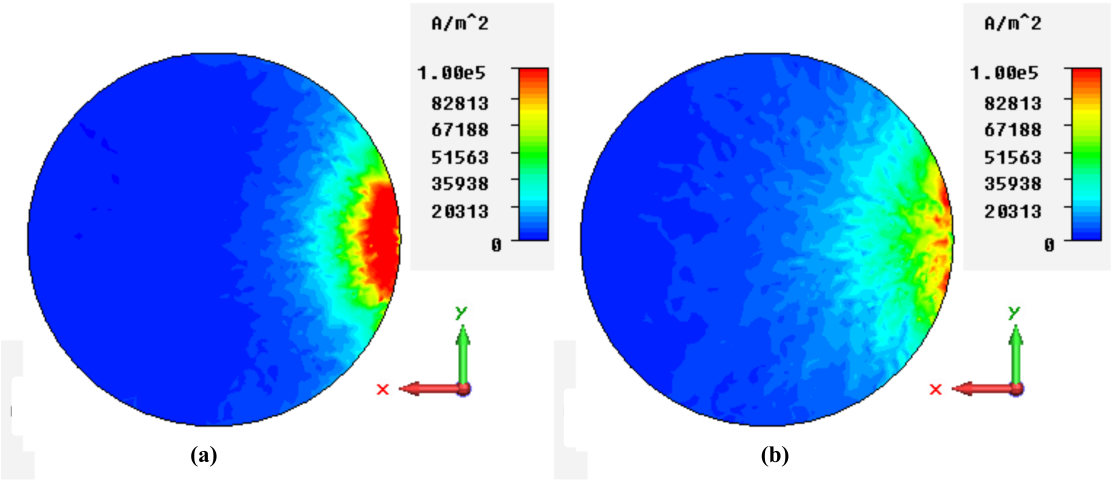

Figure 5.7: (a) Tangential current amplitude distribution on bottom surface of the steel plate; and (b) on top surface of the steel plate. Here, horizontal distance between the plate and the coil centers is 115 mm, i.e., approximately 10% of the coil is covered by the plate's projection.

In Figure 5.5 it is clear that the induced currents on the bottom surface do not

couple to the top surface. On the other hand, in Figure 5.6, the induced currents on the bottom surface goes through the plate side edges and flows on the top surface as well. As we explained above, these currents flow in the reverse directions to form a complete loop. Moreover, in Figure 5.7, the same phenomenon is observed. In the figure, additional currents on the top surface those arise due to looping magnetic fields produced by the coil are also seen. These currents are in reverse direction with those induced on the bottom surface by the generated magnetic flux of the coil. Since in Figure 5.7, most of the coil is uncovered by the plate, the latter currents have more effects. In the figure to observe currents more clearly, the color bar limit is decreased to $10^5 A/m^2$.

On the other hand, resistance of the unloaded coil is measured to be approximately 0.5 Ω and it increases monotonically with the plate's coupling (see Figure 5.4(b)). This is because of the fact that the induced eddy currents on the plate turn into heat and dissipate power to be independent from its direction. Moreover, in the figures it is observed that, in spite of their circular distribution, the inductance and the resistance plots are not purely symmetric. The reason for this measurement error is that the plate was not perfectly parallel to the coil plane.

Measurements were repeated at 100 kHz frequency. It was observed that the inductance values are lower at 100 kHz than those observed at 20 kHz. On the other hand, it was also seen that the system equivalent resistance increases with frequency. One of the effects for the enhancement in resistance is skin depth. Since the skin depth decreases with operational frequency, the resistance increases. These observations are clearly seen in Figure 5.8 where changes of the inductance and resistance values with a percentage area of the coil covered by the plate are presented.

The percentage area is simply ratio of the coil area covered by the plate to the coil's total area. The total area and the partial area covered by the plate are

calculated by equation (5.1) [55].

$$A_{coil} = \pi r^2$$

$$A_{covered} = \begin{cases} 0 & ; r + R < d \\ \pi r^2 & ; d < R - r \\ r^2 cos^{-1}\left(\frac{d^2 + r^2 - R^2}{2dr}\right) + R^2 cos^{-1}\left(\frac{d^2 + R^2 - r^2}{2dr}\right) & \\ -\frac{1}{2}\sqrt{[(d+r)^2 - R^2][R^2 - (d-r)^2]} & ; R - r \leq d \leq r + R \end{cases} \tag{5.1}$$

Here, A_{coil} and $A_{covered}$ are the coil's total area and the intersection area between the coil and the plate's projection, respectively. In addition, d is the distance between the centers of the plate (with radius R) and the coil (with radius r).

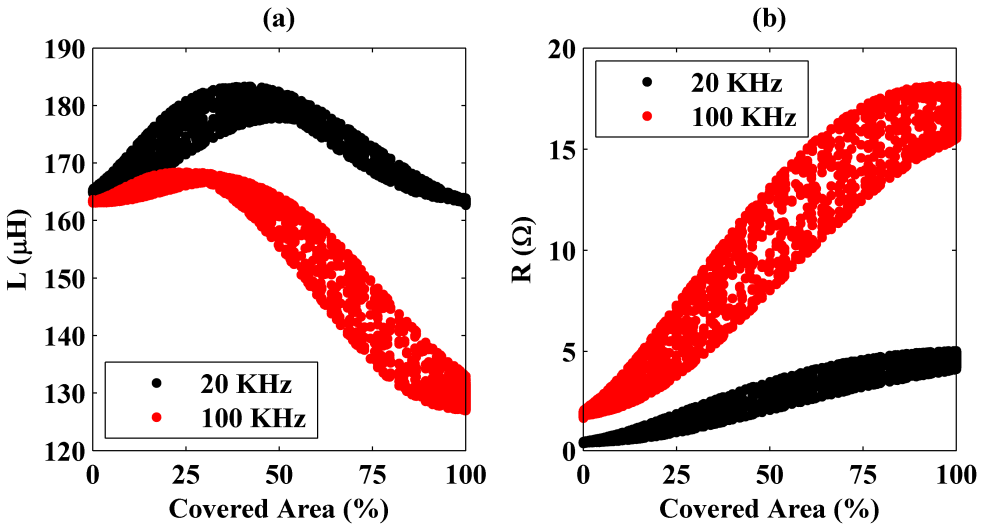

Figure 5.8: Variation of the measured inductance (a) and resistance (b) as a function of the coil area covered by the steel plate at 20 and 100 kHz frequencies.

In the figure, it is seen that the system's equivalent resistance has a monotonically increasing trend, but the same behavior is not observed for the inductance. In addition, variations in the inductance and resistance are higher at 100 kHz than those obtained at 20 kHz. Therefore, it can be deduced that, for the steel plate's detection, the resistance should be considered rather than the inductance,

and it is easier at high operation frequencies. In addition, in the figures, there exist multiple inductance and resistance values that correspond to constant covered area percentages. As explained previously, the reason for this measurement error is the plate's not being completely parallel to the coil.

Similar measurements were conducted using an aluminum plate whose geometry is the same with that of the steel plate. Variations of the inductance and the resistance values with the coil area covered by the aluminum plate are shown in Figure 5.9.

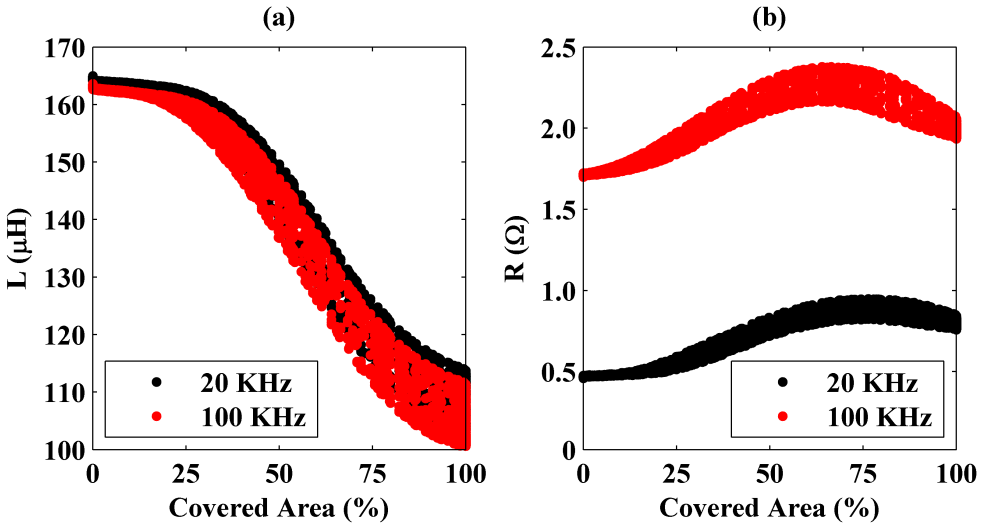

Figure 5.9: Variation of the measured inductance (a) and resistance (b) as a function of the coil area covered by the aluminum plate at 20 and 100 kHz frequencies.

In the figure, a behavior different from that observed with the steel plate is expressed. Here instead of the resistance, system's inductance has a monotonically decreasing trend with the covered area. Therefore, for the aluminum plate's coverage detection, the inductance value should be considered rather than the resistance but high operation frequencies do not make this procedure easier. In Figure 5.9, the inductance does not change considerably with frequency. This is because of low magnetic permeability of the aluminum at 20 kHz and 100 kHz frequencies. Magnetic flux produced by the coil couples less to the aluminum plate.

These different behaviors observed for the steel and the aluminum plates are because of their magnetic and electrical properties. For the aluminum plate (see Figure 5.9(b)), the measured resistance first increases and then decreases as the coil moves out of the plate's projection. Small increases initially observed are due to the plate's edges. Currents induced on the aluminum plate encounter discontinuities at the edges, which increases the equivalent resistance. However, at some point (at around 75% at 20 kHz and 60% at 100 kHz in Figure 5.9), the resistance decreases towards the level of unloaded coil's resistance. This is because of the fact that, after some point, decrease in coupling between the coil and the plate dominates the edge effects. Since the aluminum's resistivity is very low, this effect is seen here, but it is negligible for stainless steel because of its high resistance.

Moreover, the measured inductance has a monotonically decreasing trend, which is different from that observed previously in Figure 5.8 for the steel plate. Because of its low magnetic permeability, the induced currents on the bottom surface of the aluminum plate couple to the top surface considerably. In other words, because of the coil's magnetic fluxes, currents are induced on both bottom and top surfaces of the plate. These currents flow in the same direction. Although there still exist reverse currents on the top surface as a result of bending of the currents on the bottom surface near the plate edges and the looping magnetic fields, the total current on the top surface is in the same direction with the current on the bottom surface. Therefore, a continuous decrease in the measured inductance is observed with the covered area. Current distributions on the aluminum plate located at different positions were also calculated using 3D full electromagnetic solutions. Calculated tangential current amplitude distributions are represented in Figure 5.10, Figure 5.11 and Figure 5.12.

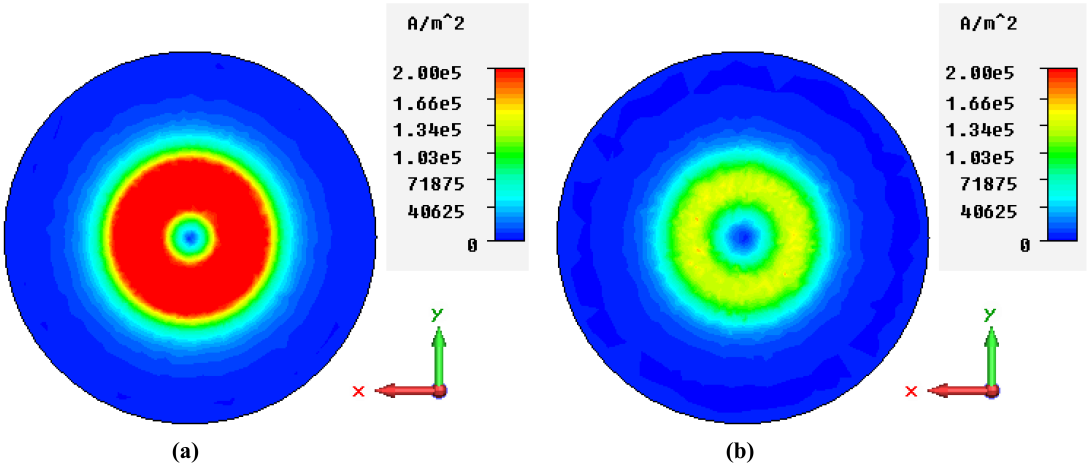

Figure 5.10: (a) Tangential current amplitude distribution on bottom surface of the aluminum plate; and (b) on top surface of the aluminum plate. Here plate and the coil centers coincide, i.e., coil is covered by the plate's projection completely.

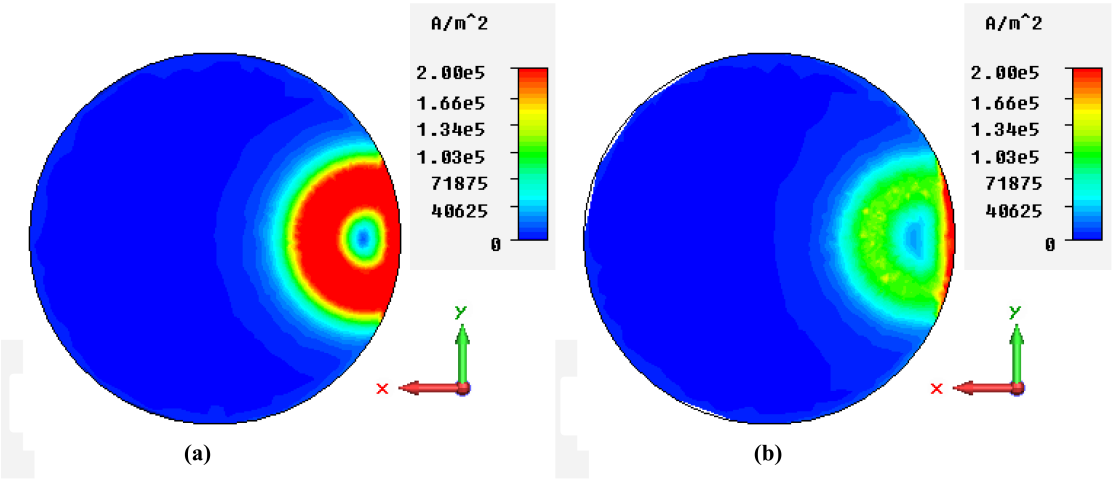

Figure 5.11: (a) Tangential current amplitude distribution on bottom surface of the aluminum plate; and (b) on top surface of the aluminum plate. Here horizontal distance between the plate and the coil centers is 75 mm, i.e., approximately 70% of the coil is covered by the plate's projection.

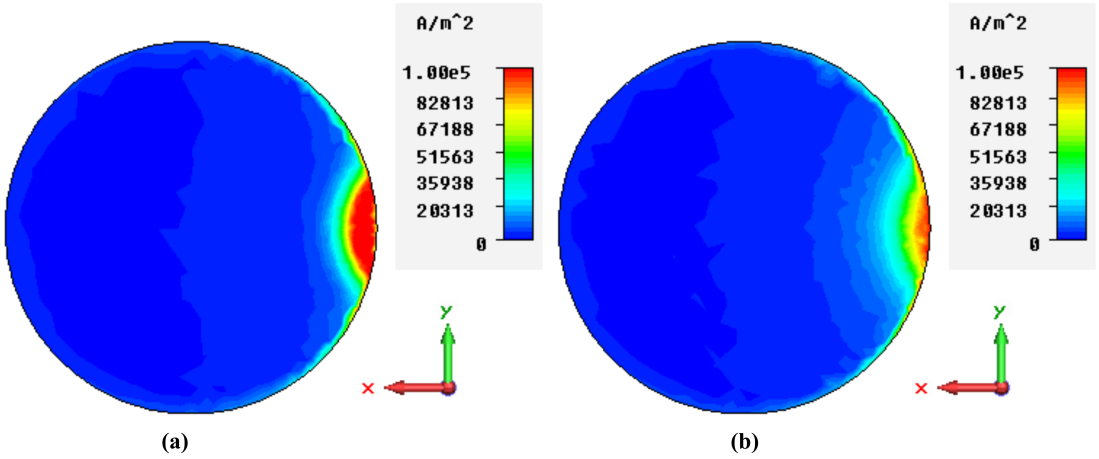

Figure 5.12: (a) Tangential current amplitude distribution on bottom surface of the aluminum plate; and (b) on top surface of the aluminum plate. Here horizontal distance between the plate and the coil centers is 115 mm, i.e., approximately 10% of the coil is covered by the plate's projection.

Different from Figure 5.5, in Figure 5.10 it is seen that the induced currents on the bottom surface couples to the top surface in considerable amounts. As we explained, this is because of low magnetic permeability of aluminum. Also, in Figure 5.11 additional currents around the plate edges on the top surface are observed. As in the case of the steel plate, these currents arise due to curling of induced currents on the bottom surface around the plate's edges. Moreover, in Figure 5.12 these currents around the edge are clearly seen, too. However, total current on the top surface of the aluminum plate is lower in the figure than that observed in Figure 5.7 for the steel plate. One of the reasons behind this is coupling of the induced currents on the bottom surface to the top surface. Since these currents are in reverse direction with currents arisen by curling of bottom surface currents around the plate edges and currents emerged with looping magnetic fields produced by the coil, currents on the top surface diminish.

As a result, by applying small signals at two different frequencies and measuring the system inductance and resistance, the fractional area of the coil covered by the vessel can be determined precisely. However, in all-surface heating, coils are located in an array architecture. To investigate its effect, another circular coil

was brought near the coil that is connected to the LCR meter. As expected, since measurements were obtained with small signals and the second coil's tips were open circuit, the inductance and resistance values were the same within those of the single coil measurements. Therefore, by applying small signals to each of the array coils individually at two different frequencies, in all-surface heaters, the location and the material of a vessel can be uniquely identified. To avoid a large database in the identification process, materials that have similar properties can be grouped together. Furthermore, measured data directly can be used to calculate power transmission from coils to the vessel. On the other hand, algorithms based on the coils' coverage can be created for easy determination of the vessel's location. For instance, the center of a vessel can be found by considering the coils' coverage by the vessel, which are placed side by side. By using distances of these coils to the identified center point, the vessel's size can be determined together with its approximate shape.

Since the inductance and resistance values cannot be measured directly from the coil's small signal response and their calculations require additional time and effort for the system, investigating other parameters that are directly measurable might be a better idea. To this end, we calculated magnitude and angle values of the coil's impedance from the measured inductance and resistance using equations (5.2) and (5.3), respectively. The magnitude and angle of the coil impedance can be found directly by the amplitude ratio of signal's voltage and current levels that is sent to the coil and the phase difference between them, respectively.

$$abs(Z) = abs(R + j\omega L) = \sqrt{(R^2 + \omega^2 L^2)} \tag{5.2}$$

$$angle(Z) = angle(R + j\omega L) = tan^{-1}(\frac{\omega L}{R}) \tag{5.3}$$

Here, Z is the coil's impedance. Its magnitude and angle are represented with $abs(Z)$ and $angle(Z)$, respectively. L and R denote the measured inductance and resistance values, respectively. In addition, ω is the angular frequency.

Changes in the magnitude and angle of the coil's impedance as a function of the steel plate's loading are shown in Figure 5.13. Similar plots are given in Figure 5.14 for the aluminum plate.

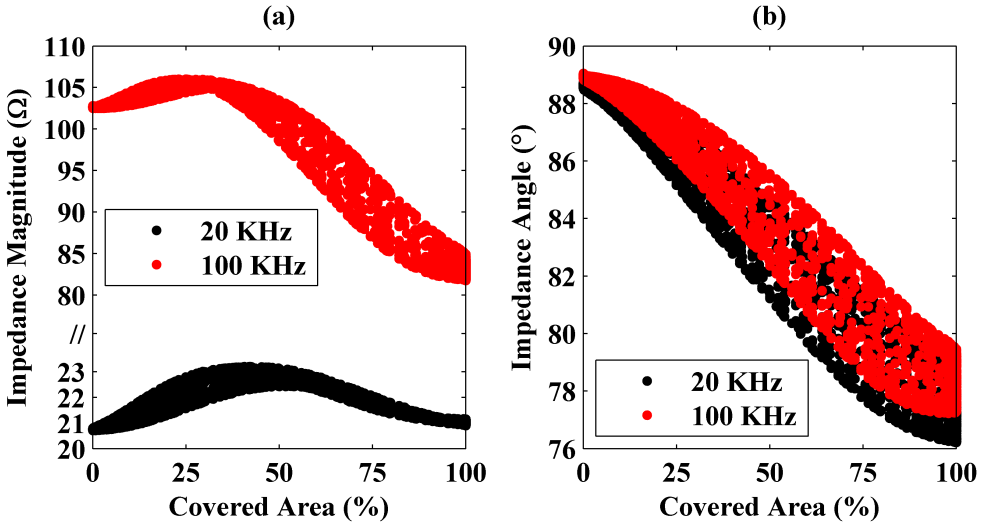

Figure 5.13: Changes of the impedance magnitude (a) and angle (b) at 20 and 100 kHz frequencies as a function of the coil area covered by the steel plate. Here, in part (a), the y axis is scaled nonuniformly for better representation of the calculated magnitudes at different frequencies.

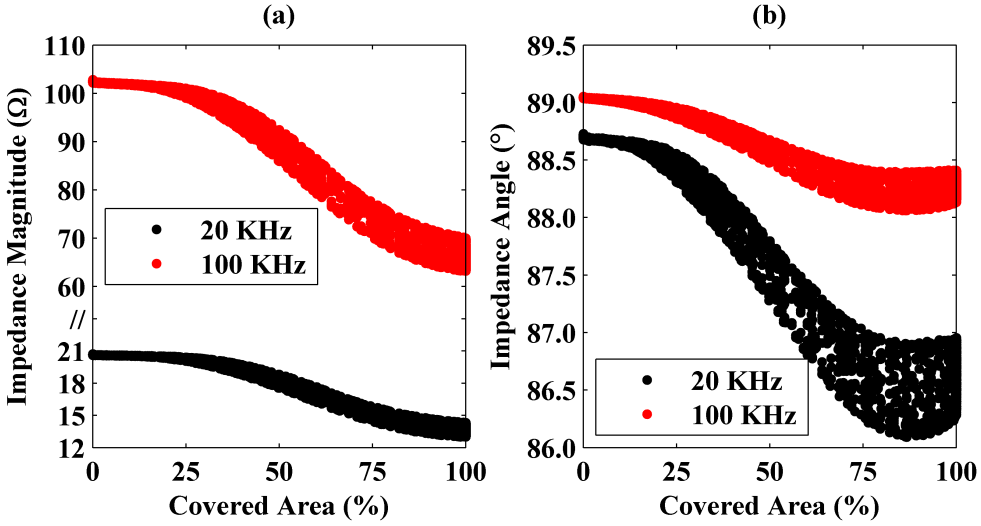

Figure 5.14: Changes of the impedance magnitude (a) and angle (b) at 20 and 100 kHz frequencies as a function of the coil area covered by the aluminum plate. Here, in part (a), the y axis is scaled nonuniformly for better representation of the calculated magnitudes at different frequencies.

From the figures, it is seen that the coverage of a plate and its material can be identified uniquely from the magnitude and angle of the coil's impedance. In addition, the impedance measurements should be carried out at different frequencies. Otherwise, identification would be hard especially for small covered area percentages because of the fact that impedance magnitudes are similar for both the steel and the aluminum plates while the impedance angles vary in small ranges at a single frequency.

5.4 Experiments with Outer Squircle-Inner Circular Coil

To verify validity of the proposed method for newly designed outer squircle coils, which enable efficient all-surface heating [11], experiments were repeated with an outer squircle-inner circular coil. The coil architecture is exactly the same with that we used in heating experiments in the previous chapters. Inner diameter of the coil is set to be 30 mm. Also, side length of the outer squircle-inner circular coil is equal to 75 mm. Structure of the outer squircle-inner circular coil is shown in Figure 5.15. Similar within circular coil measurements, inductance and resistance values of a coil having outer squircle-inner circular shape that is loaded by vessels made of different materials at different positions were successfully measured at different frequencies. The loading plates are made of stainless steel (AISI 430) and aluminum. They have cylindrical shapes with 1 mm thickness and 180 mm diameter. Measurement setup is the same with that illustrated in Figure 5.1.

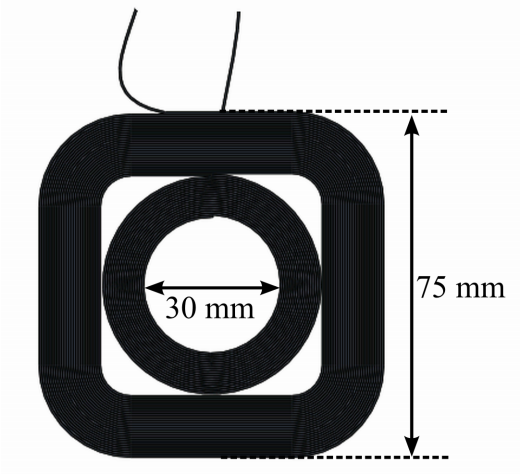

Figure 5.15: The outer squircle-inner circular coil structure used in measurements and geometrical sizes.

We first obtained measurements with the stainless steel (AISI 430) plate. Mapping of the inductance and resistance values measured at 20 kHz while the steel plate moves on the constant x-y plane is represented in Figure 5.16. As in Figure 5.4, here measured inductance and resistance values have almost symmetric distributions. This is because of the coil's symmetric outer squircle-inner circular architecture and the plate's cylindrical geometry. The small variations that violates perfect symmetry are again because of the plate's not being completely parallel to the coil during measurement.

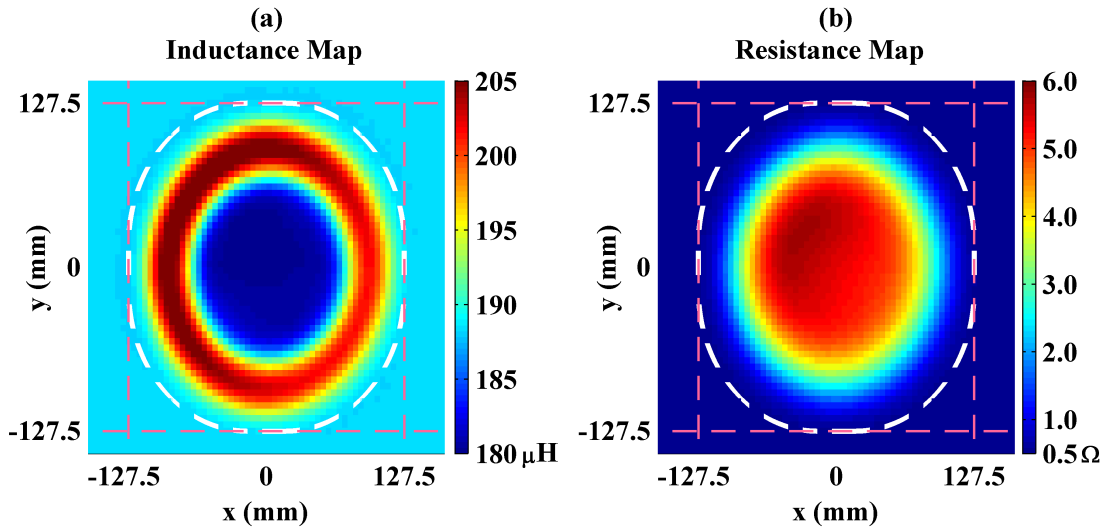

Figure 5.16: Maps of inductance and resistance values of the system measured at 20 kHz, where the outer squircle-inner circular shape coil is loaded by the steel plate that moves on the constant horizontal plane 8 mm above from the coil. Here, coil is fixed at its place such that its center is at (0,0) position. Also, the white dashed lines with squircle shape represent the points at which the plate projection and the coil are tangential. End points of these dashed lines are marked with pink dashed lines passing through x = +-127 mm and y = +-127.5 mm.

Inductance and resistance values of the unloaded outer squircle-inner circular coil were measured to be 188 μH and 0.5 Ω, respectively. As the plate projection starts to intersect with the coil, measured inductance value first increases and then decreases such that it eventually reaches a value lower than the inductance of the unloaded squircle coil. On the other hand, resistance of the coil monotonically increases as the intersection area of the plate's projection and the coil gets wider. These results are clearly seen in Figure 5.17, where change of the inductance and resistance values with the distance between the centers of the plate's projection and the coil are illustrated. Here variations are investigated as a function of distance between the plate's projection center and the coil's center because calculating the partial area of the outer squircle coil covered by the plate's projection is not as easy as calculation of the partial area of the circular coil covered by the plate's projection.

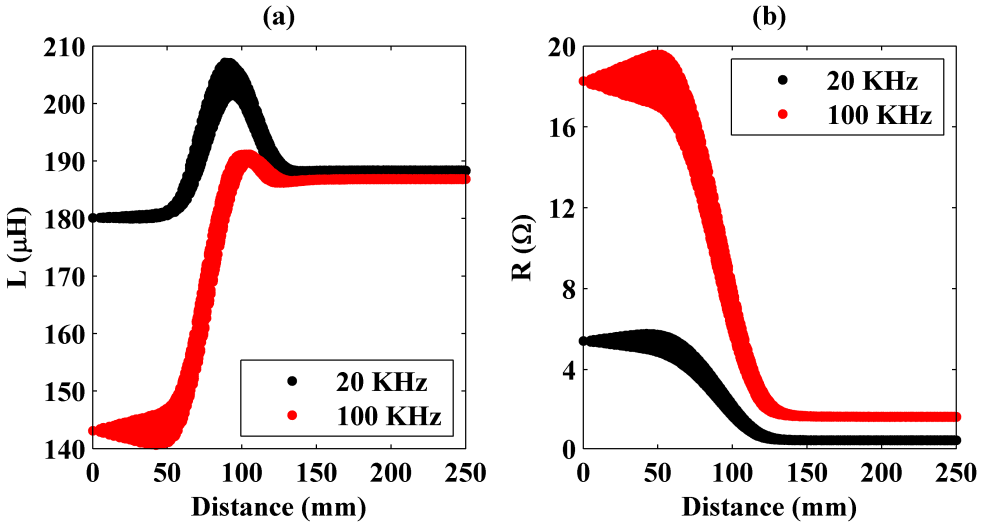

Figure 5.17: Measured inductance (a) and resistance (b) values of the system, where the steel plate is used, at 20 and 100 kHz vs. distance between the centers of the plate's projection and the coil.

Measurements were repeated with the aluminum plate. Change of the inductance and resistance values in the new system are presented in Figure 5.18.

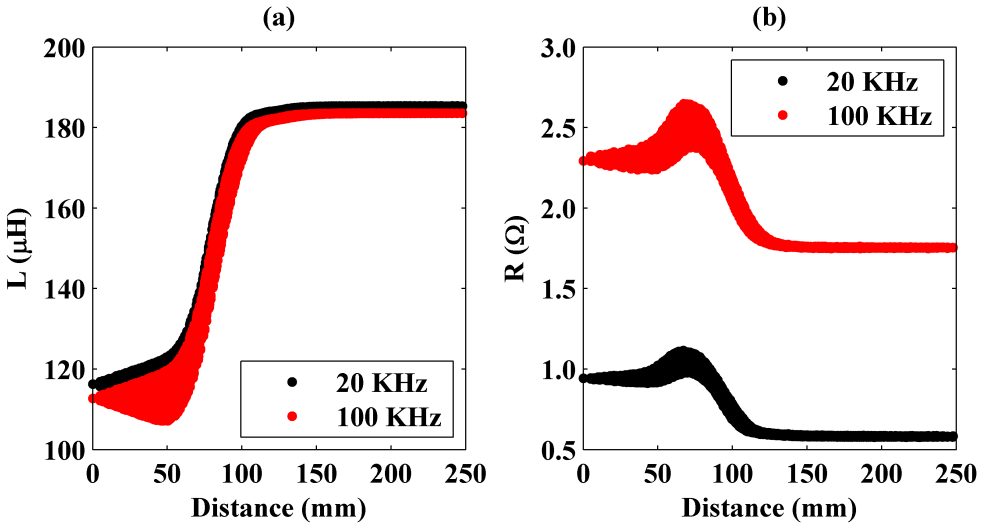

Figure 5.18: Measured inductance (a) and resistance (b) values of the system, in which the aluminum plate is used, at 20 and 100 kHz vs. distance between the centers of the plate's projection and the coil.

Similar behaviors with those obtained for the circular coil are observed in the figures. In the system, where the steel plate is used, inductance values first increase and then decrease as the plate gets closer to the coil (see Figure 5.17). On the other hand, there are monotonic increases in the resistance values. Monotonic increases are important to uniquely determine the plate's distance to the coil and so its position on the hob. Therefore, by measuring resistance values of a loaded coil at different frequencies one can determine position of the steel plate. However, this information is not enough to uniquely identify its material type. To uniquely identify the plate's material type inductance values should also be inspected. On the contrary, in the system, where the aluminum plate is used, resistance values first increase and then decrease as the pate's projection covers the coil more, whereas, inductance values decrease continuously as the plate projection gets closer to and covers more of the coil (see Figure 5.18). Again, to uniquely identify the plate material type and specify its position inductance and resistance values measured at various frequencies should be taken into account.

In addition, in the figures, measured resistance values are considerably higher at 100 kHz than those at 20 kHz. This is expected and because of the decrease in skin depth of the plate materials at high frequencies. On the other hand, inductance values are lower at 100 kHz than those at 20 kHz. Although, the difference between the measured inductance values is very clear in the system, where the steel plate is used, it is considerably smaller in the system, where the aluminum plate is placed. This distinction is due to the plate's material type. Decrease in the loaded coil's inductance occurs because of reverse eddy currents on the load, thus large decrease in equivalent inductance at high frequencies implies high coupling between the plate and the coil.

Since inductance and resistance values at a specific frequencies are related with magnitude and angle of the coil's impedance (see equations (5.2) and (5.3)), it is also possible to uniquely identify the plate material type and to determine its position by using magnitude and angle values of the coil's impedance at different frequencies. It might be preferred in a heating system because coil's impedance can directly be measured from voltage and current signals supplied to the coil. Moreover, from inductance and resistance mapping data it is possible to derive

inductance and resistance changes as a function of intersection area between the plate's projection and the coil.

5.5 Summary

In this work, a new wireless detection methodology for sensing metal coverage and identifying its material type in all-surface induction hobs is presented. Results show that, for a coupled system, one can determine accurately the partial area of a coil covered by a vessel and the distance and position of the vessel with respect to coils from inductance and resistance variations. Material properties of the vessel can also be identified. However, wireless detection is easier at higher frequencies because variations in the inductance and resistance increase with operating frequency. This method is proved to be useful not just for the conventional shape circular coils but also for the outer squircle-inner circular shape coils designed for efficient all-surface induction hobs.

Moreover, since inductance and resistance values are related with magnitude and angle of the coil's impedance, they were also shown to be used for identification and determination processes. By measuring voltage and current of each coil sequentially, identification of the plates coverage by coils and its position together with its material type is possible in all-surface heaters. In addition, measurements at different frequencies make this process easier. These results are beneficial for automatically detecting vessels and determining which coils to power up with predetermined current magnitudes in all-surface induction hobs.

Chapter 6

Conclusion

In this thesis, wireless induction systems have been introduced for high efficiency in heating and wireless energy transfer. New system and coil designs have been investigated for efficiency enhancement and to overcome problems in induction systems. These studies are beneficial for demonstrating highly efficient space-invariant all-surface induction hobs, in which a vessel is detected and corresponding coils are powered up automatically.

In conventional induction hobs vessels having sizes and shapes similar to those of the coils should be placed right on top of coils for efficient heating. To overcome these restrictions, array of small coils are placed beneath the hob surface. However, interaction between circular coils are not high enough. To increase interaction between coils and enhance system heating efficiency we propose outer squircle-inner circular shape coils. With their long tangential sides at their outer rims, side-by-side placed outer squircle-inner circular coils interact more with respect to circular shape coils. Our heating measurements and simulations demonstrate that for a simple inductive heating system composed of a pair of coils and a loading plate heating speed and energy transfer ratio are higher in the case where outer squircle-inner circular coils are used. In addition, we further investigated efficiency and heating variation in system with phase difference application. Both measurement and simulation results clearly show that side-by-side placed coils

couple constructively in regions above their close edges when 180° phase difference is applied. On the other hand, if coils are driven with 0° phase difference they interfere destructively in regions above their close edges and constructively in regions above their far sides. Also, it was proved that the system heating and power transfer efficiency increase further with phase difference application. Therefore, highest efficiency and power transfer ratio are found in systems where the outer squircle-inner circular coils are driven with the 180° phase difference. Moreover, we calculated enhancement in power transfer due to coupling between a pair of (side-by-side placed) outer squircle-inner circular coils for different outer squircle turn number. It was demonstrated that for the proposed outer squircle-inner circular coil architecture after a specific turn number (26 in our case) coupling between side-by-side placed coils does not change too much. Since production of squircle coils becomes more difficult as their side lengths reduce (especially for thick wires) and squircle coils consume more wires than circular coils to occupy the same region, we replaced squircle turns in the inner side of the coils with circular turns. Furthermore, it was shown that the inductance and resistance values of the proposed outer squircle-inner circular coils and the systems composed of these squircle coils are similar to those of the circular coils and the systems composed of these circular coils, respectively. Therefore, we proved that systems containing the proposed outer squircle-inner circular coils are available to use with power circuitry that is designed for and used with the circular coils. Enhancements in heating efficiency and power transfer ratio with the proposed outer squircle-inner circular coils and the phase difference application were demonstrated for vessels having different sizes, located at different positions and distances to include all possible induction hobs.

As a continuation of this study, we further investigated a system composed of a plate and four of the proposed outer squircle-inner circular or circular coils. Again we comparatively measured heating speed of the system with the 0° and 180° phase differences between consecutive coils. Similar within two coil measurements, in the system plate is heated up starting from regions above the furthermost corners of the coils when coils are driven with the 0° phase difference.

However, when coils are driven with the 180° phase difference plate's temperature becomes highest in areas above close sides of the adjacent coils. Our results show that heating efficiency enhancement observed in four outer squircle-inner circular coils measurements with respect to four circular coils measurements are higher than the heating efficiency enhancement calculated for a pair of the outer squircle-inner circular coils with respect to a pair of the circular coils. It was expected from the fact that in four coil alignment when 180° phase difference is applied, each coil interferes constructively with the other two coils that are next to it. On the other hand, in the system cross coils couple destructively with both the 0° and 180° phase difference applications. Temperature distributions over the plate that we obtained clearly show that. This is indeed the reason why we propose to use coils with outer squircle turns instead of rectangular or square shape coils. By rounding corners of the outer rims in the proposed outer squircle-inner circular coils, we make diagonally located coils to be farther away from each other, which decreases destructive coupling between these coils.

After showing efficiency enhancement in systems with the proposed outer squircle-inner circular coils and phase difference application, we modeled an all-surface inductive heating system with nine of the outer squircle-inner circular coils aligned tangentially in a 2D square lattice 3×3 array. System heating speed was measured for a plate located at various positions on the surface, where different coils are powered up depending on the plate position. Results show that with the proposed system composed of an array of the outer squircle-inner circular coils aligned tangentially in a 2D square lattice and driven by 180° phase difference between consecutive coils, efficient heating and power transfer is achieved independent from the vessel position. In all the cases, plate is heated with almost a constant speed and efficiency. In addition, it was demonstrated that true powers supplied to the coils in a system are proportional with their loadings. Depending on the plate position, coils' loadings change. Some coils are turned on and some coils are turned off with plate's various positions. True powers supplied to the coils might also be different in an inductive heating system because some coils might be covered and loaded by the vessel more, whereas some coils might be covered and loaded by the vessel less. The proposed inductive heating system is

beneficial for all-surface induction hobs in terms of demonstrating its feasibility, which has a space-invariant and efficient heating properties all over its surface at a constant speed.

To sum up, we proposed and designed all-surface inductive heating system consists of the outer squircle-inner circular coils aligned tangentially in a 2D square lattice with space-invariant and efficient heating properties all over its surface. However, in all-surface induction hobs vessel's presence should be detected and its position should be accurately determined for efficient and safe heating. In addition, identification of vessel material is important, too. These are issues encountered not just in all-surface induction hobs but also in conventional inductive heating systems. To this end, we proposed and investigated an easy and rigid method that allows automatic vessel detection together with identification of vessel material and determination of its position on the hob surface. Method is based on measuring inductance and resistance values of a coil loaded by a vessel at different frequencies. With simple inductance and resistance measurements in a system composed of a plate and a coil, it has been shown that inductance ad resistance values of a coil change with the plate's coverage over the coil, i.e., plate's position on the hob surface, and with the plate's material. It was observed that for some materials change of the inductance values as a function of the plate's coverage display monotonic behaviour, whereas the resistance values do not display monotonic behaviour and for some other materials it is vice versa. Therefore, inductance and resistance values were obtained at different frequencies to provide additional information. It was demonstrated that one can determine vessel's material type and its position on the hob surface by measuring inductance and resistance of the coil at various frequencies. Results show that the process is easier at high frequencies. Measurements with different coils proved that the proposed method is useful not just for conventional circular coils but also for the designed outer squircle-inner circular coils, which are proposed to be used and enable high heating efficiency in all-surface induction hobs. Moreover, because inductance and resistance values of a coil at a specific frequency is related with magnitude and angle of its impedance at the same frequency, it was proved that vessel's material type and its position on the hob surface can also be determined

by measuring magnitude and angle of the coils at different frequencies. However, for all these identification and determination process premeasured inductance and resistance (or magnitude and angle of impedance) data sets are required. The proposed method is beneficial for automatically detecting vessel's presence and identifying its material type together with determining its position and size on an induction hob surface, which yield powering on only the coils that are loaded by the vessel with predetermined current magnitudes.

Bibliography

[1] *www.arcelik.com.tr/built-in-electrik-hob-induction-hobs-OI-655-TS-Built-In-Hobs.html*.

[2] K. Toshihiro, "Induction heater," *European Patent Application*, no. EP 1811812 A1, 2007.

[3] I. Hirota, A. Fujita, T. Miyauchi, Y. Fujii, A. Kataoka, K. Aihara, and N. Makio, "Induction heating device," *United States Patent*, no. 7057144 B2, 2006.

[4] "Induction cooker with heating coil and electrical conductor," *United States Patent*, no. 7,049,563 B2, 2006.

[5] Renesas Technology Europe, "Induction cooking basics," 2008.

[6] Fairchild Semiconductor, "Induction heating system topology review," 2000.

[7] J. Acero, J. M. Burdio, L. A. Barragan, D. Navarro, R. Alonso, J. R. Garcia, F. Monterde, P. Hernandez, S. Llorente, and I. Garde, "Domestic induction appliances," *IEEE Ind. Appl. Mag.*, vol. 16, no. 2, pp. 39 – 47, Mar./Apr. 2010.

[8] H. V. Demir, E. Unal, E. Gonendik, V. T. Kilic, N. Yilmaz, M. Ozturk, and U. Oktay, "An inductive coil unit," *Turkish Patent Application*, 2015/15179.

[9] H. V. Demir, E. Unal, E. Gonendik, V. T. Kilic, N. Yilmaz, M. Ozturk, and U. Oktay, "An inductive coil unit," *Turkish Patent Application*, 2015/15188.

[10] H. V. Demir, E. Unal, E. Gonendik, V. T. Kilic, N. Yilmaz, M. Ozturk, and U. Oktay, "An inductive coil unit," *Turkish Patent Application*, 2015/15196.

[11] V. T. Kilic, E. Unal, E. Gonendik, N. Yilmaz, and H. V. Demir, "Strongly coupled outer squircle-inner circular coil architecture for enhanced induction over large areas," *IEEE Trans. Ind. Electron.*, vol. 63, no. 12, pp. 7478 – 7487, 2016.

[12] V. T. Kilic, E. Unal, and H. V. Demir, "Space-invariant all-surface inductive heating at a constant speed enabled by tangent squircle coils in square lattice," *IEEE Trans. Ind. Appl.*, (in submission).

[13] V. T. Kilic, E. Unal, and H. V. Demir, "Wireless metal detection and surface coverage sensing for all-surface induction heating," *Sensors*, vol. 16, no. 3:363, Mar. 2016.

[14] V. T. Kilic, E. Unal, and H. V. Demir, "Inductance and resistance measurement method for vessel detection and coil powering in all-surface inductive heating systems composed of outer squircle coils," *AIP Adv.*, (accepted to be published).

[15] D. K. Cheng, "Fundamentals of engineering electromagnetics," *Addison-Wesley*, 1993.

[16] R. A. McCoy, T. Creek, and W. C. Moreland, "Cooking vessel for use with induction heating cooking unit," *United States Patent*, no. 3966426, 1976.

[17] M. Hediehloo and M. Akhbari, "New approach in design of planar coil of induction cooker based on skin and proximity effects analysis," *IEEE International Conference on Industrial Technology*, 2009.

[18] J. Acero, P. J. Hernandez, J. M. Burdio, R. Alonso, and L. A. Barragan, "Simple resistance calculation in litz-wire planar windings for induction cooking appliances," *IEEE Trans. Magn.*, vol. 41, no. 4, pp. 1280 – 1288, 2005.

[19] O. Lucia, J. M. Burdio, J. Acero, L. A. Barraga, and J. R. Garcia, "Educational activities and results obtained from a university-industry collaborative framework experience," *IEEE-Promotion and Innovation with New Technologies in Engineering Education (FINTDI)*, 2011.

[20] S. Cetin, B. S. Sazak, and H. Bodur, "A comparative study of dual half-bridge inverter topologies used in induction cooking," *Electrical Engineering/Electronics, Computer, Telecommunications and Information Technology (ECTI-CON)*, 2009.

[21] C. Carretero, O. Lucia, J. Acero, and J. M. Burdio, "Phase-shift control of dual half-bridge inverter feeding coupled loads for induction heating purposes," *IET Electronics Letters*, vol. 47, no. 11, pp. 670 – 671, 2011.

[22] D. Puyal, C. Bernal, J. M. Burdio, J. Acero, and I. Millan, "Methods and procedures for accurate induction heating load measurement and characterization," *IEEE International Symposium on Industrial Electronics (ISIE)*, pp. 805 – 810, 2007.

[23] J. Acero, O. Lucia, C. Carretero, I. Lope, and C. Diez, "Efficiency improvement of domestic induction appliances using variable inductor-load distance," *Applied Power Electronics Conference and Exposition (APEC)*, pp. 2153 – 2158, 2012.

[24] J. Acero, C. Carretero, I. Millan, R. Alonso, O. Lucia, and J. M. Burdio, "Experimental setup for inductive efficiency measurements of domestic induction systems based on energy balance," *36^{th} Annual Conference on IEEE Industrial Electronics Society*, pp. 114 – 119, 2010.

[25] J. Acero, C. Carretero, O. Lucia, and J. M. Burdio, "Analysis of the coupling between small ring-type coils used in adaptable-size burners for domestic induction heating hobs," *Applied Power Electronics Conference and Exposition (APEC)*, pp. 2000 – 2006, 2011.

[26] J. Acero, R. Alonso, J. M. Burdio, and L. A. Barragan, "Enhancement of induction heating performance by sandwiched planar windings," *IET Electronic Letters*, vol. 42, no. 4, pp. 241 – 242, 2006.

[27] W. A. Roshen and D. E. Turcotte, "Planar inductors on magnetic substrates," *IEEE Trans. on Magn.*, vol. 24, no. 6, pp. 3213 – 3216, 1988.

[28] K. Leidig and M. Herzog, "Induction cooking hob," *European Patent*, no. EP 2265088 B1, Jun. 27, 2012.

[29] D. Puyal, C. Bernal, J. M. Burdio, I. Millan, and J. Acero, "Dual 1.5-mhz 3.5-kw versatile half-bridge series-resonant inverter module for inductive load charaterization," *Applied Power Electronics Conference*, pp. 1133 – 1139, 2007.

[30] A. Fujita, H. Sadakata, I. Hirota, H. Omori, and M. Nakaoka, "Latest developments of high-frequency series load resonant inverter type built-in cooktops for induction heated all metallic appliances," *Power Electronics and Motion Control Conference*, pp. 2537 – 2544, 2009.

[31] H. Okatsuka, K. Taniguchi, and T. Kakizawa, "Electromagnetic induction heating aparatus capable of heating nonmagnetic cooking vessels," *United States Patent*, no. 4,549,056, 1985.

[32] K. Matsushita and H. Ishida, "Electromagnetic induction heating cooking utensil," *United States Patent*, no. 4,614,852, 1986.

[33] C. Carretero, J. Acero, R. Alonso, J. M. Burdio, and F. Monterde, "Modeling mutual impedances of loaded non-coaxial inductors for induction heating applications," *IEEE Trans. on Magn.*, vol. 44, no. 11, pp. 4115 – 4118, 2008.

[34] J. Acero, R. Alonso, J. M. Burdio, L. A. Barragan, and D. Puyal, "Analytical equivalent impedance for a planar circular induction heating system," *IEEE Trans. on Magn.*, vol. 42, no. 1, pp. 4115 – 4118, 2006.

[35] L. C. Meng, K. W. E. Cheng, and W. M. Wang, "Thermal impacts of electromagnetic proximity effects in induction cooking system with distributed planar multicoils," *IEEE Trans. on Magn.*, vol. 47, no. 10, pp. 3212 – 3215, 2011.

[36] P. Hernandez, F. Monterde, J. M. Burdio, and J. R. Garcia, "Loss optimisation of foil coils for induction cooking," *24th Annual Conference of the IEEE Industrial Electronics Society*, pp. 371 – 374, 1998.

[37] J. Acero, C. Carretero, I. Millan, O. Lucia, R. Alonso, and J. M. Burdio, "Analysis and modeling of planar concentric windings forming adaptable-diameter burners for induction heating appliances," *IEEE Trans. Power Electron.*, vol. 26, no. 5, pp. 1546 – 1558, 2011.

[38] I. Millan, J. M. Burdio, J. Acero, O. Lucia, and D. Palacios, "Resonant inverter topologies for three concentric planar windings applied to domestic induction heating," *IET Electron. Lett.*, vol. 46, no. 17, pp. 1225 – 1226, 2010.

[39] F. Forest, S. Faucher, J. Y. Gaspard, D. Montloup, J. J. Huselstein, and C. Joubert, "Frequency-synchronized resonant converters for the supply of multiwinding coils in induction cooking appliances," *IEEE Trans. Ind. Electron.*, vol. 54, no. 1, pp. 441 – 452, 2007.

[40] J. Acero, C. Carretero, O. Lucia, R. Alonso, and J. M. Burdio, "Mutual impedance of small ring-type coils for multiwinding induction heating appliances," *IEEE Trans. Power Electron.*, vol. 28, no. 2, pp. 1025 – 1035, 2013.

[41] D. Fournier, E. Merliot, and A. Roux, "Assembling module of induction coils of a induction heating cooking area and cooking area including the said modules," *European Patent*, no. EP 1575336 B1, Jan. 27, 2010.

[42] A. Roux, "Induction device comprising multiple individual coils for induction heating plates," *United States Patent Application*, no. US 2009/0020526 A1, Jan. 22, 2009.

[43] W. A. Roshen, "Effect of finite thickness of magnetic substrate on planar inductors," *IEEE Trans. on Magn.*, vol. 26, no. 1, pp. 270 – 275, 1990.

[44] J. R. Davis, "Properties of stainless steels," *in ASM Speciality Handbook: Stainless Steels, Materials Park, Ohio*, pp. 489 – 495, 1994.

[45] M. Enokizono, "Numerical analysis of high-frequency induction heating including temperature dependence of material characteristics," *IEEE Trans. Magn.*, vol. 31, no. 4, pp. 2438 – 2444, 1995.

[46] O. Lucia, J. M. Burdio, L. A. Barragan, C. Carretero, and J. Acero, "Series resonant multiinverter with discontinuous-mode control for improved light-load operation," *IEEE Trans. Ind. Electron.*, vol. 58, no. 11, pp. 5163 – 5171, 2011.

[47] O. Lucia, C. Carretero, J. M. Burdio, J. Acero, and F. Almazan, "Multiple-output resonant matrix converter for multiple induction heaters," *IEEE Trans. Ind. Applicat.*, vol. 48, no. 4, pp. 1387 – 1396, 2012.

[48] O. Lucia, H. Sarnago, and J. M. Burdio, "Soft-stop optimal trajectory control for improved performance of the series resonant multi-inverter for domestic induction heating applications," *IEEE Trans. Ind. Electron.*, vol. 62, no. 10, pp. 6251 – 6259, 2015.

[49] J. Acero, C. Carretero, O. Lucia, R. Alonso, and J. M. Burdio, "Mutual impedance of small ring-type coils for multiwinding induction heating appliances," *IEEE Trans. Power Electron.*, vol. 28, no. 2, pp. 1025 – 1035, 2013.

[50] W. Essig, F. Bogdanski, G. Fettig, and J. Horn, "Inductive based cooking system," *United States Patent*, no. 5,428,207, 1995.

[51] M. E. Tulu and D. Yildirim, "Induction cooker design with quasi resonant topology using jitter drive method," *In Proceedings of the International Conference on Environment and Electrical Engineering (EEEIC)*, pp. 1 – 6, May 2013.

[52] Holtek Semiconductor Inc., "Using the HT45R38 for pan detection in induction cookers."

[53] C. Franco, J. Acero, R. Alonso, C. Sagues, and D. Paesa, "Inductive sensor for temperature measurement in induction heating applications," *IEEE Sens. J.*, vol. 12, no. 5, pp. 996 – 1003, 2012.

[54] O. Jimenes, O. O. Lucia, L. A. Barragan, D. Navarro, J. I. Artigas, and I. Urriza, "Fpga-based test-bench for resonant inverter load characterization," *IEEE Trans. Ind. Inform.*, vol. 9, no. 3, pp. 1645 – 1654, 2013.

[55] E. W. Weisstein, "Circle-circle intersection," *http://mathworld.wolfram.com/Circle-CircleIntersection.html*.

Appendix A

Simulation Results of Outer Squircle-Inner Circular and Circular Coils with Plates Made of Different Materials, Located at Different Positions and Have Various Sizes

The proposed outer squircle-inner circular coil shows better performances than conventional circular coils as they placed side by side in all-surface heating. This is because of enhanced interaction based on their long tangential outer rims. Also, their rounded corners are unique for all-surface application because they decrease destructive interaction between diagonally located coils. These properties of the proposed coil geometry are explained in Chapter 3. To understand and explain the proposed coil and the system better, we have numerical studies. With full 3D electromagnetic simulations, we have investigated the proposed outer squircle and the conventional circular coils. Also, with numerical simulations we have

examined system heating efficiencies and performances under loads made of different materials, located at different positions and have various sizes. Although rigid theoretical analysis can be another method to investigate the system, it is not an easy approach.

The commonly used setups for inductive heating construct coupled systems. In our case, the side-by-side placed coils are also coupled both among themselves and with the load plate. There also exists a ferrite layer below the coils. Current flowing on each coil produces magnetic flux, which couples to the plate and the other coil. Therefore, eddy currents are induced on the plate and the coils. These induced eddy currents affect magnetic field distributions in the whole system. A rigid theoretical analysis of such multi-element coupled system is not easy and requires approximations as well as numerical solutions of these large equations. Since all the dimensions and lengths are too small compared to the operational wavelength, approximations that are similar to far-field approximations generally made in high-frequency calculations are not possible here, either. This is one of the fundamental challenges in such a near-field low-frequency system analysis.

On the other hand, by covering the entire range of loading parameters possible in a typical inductive heating system, we systematically demonstrated that the proposed coil architecture exhibit better performance than that of conventional circular coils. In all cases, the highest efficiency is obtained using a pair of the proposed outer squircle-inner circular coils driven with the 180° phase difference.

The critical loading parameters defining an inductive heating system are vessel material, vessel size and vessel distance to the coils. Fully covering the ranges of these listed parameters, as is given and explained in detail in the following paragraphs, we show that the proposed coil exhibits better performance for all loading conditions including possible different materials to be heated in different possible size at different distances.

In induction hobs, heating vessels are desired to be as close as possible to the coils for high efficiency. Therefore, in conventional induction hobs, one of the highest distance between the heating vessels and the coils, i.e., the total thickness

of the separating material such as silargan glass, is around 20 mm. However, this separating material should still be thick enough to prevent heat transfer from the vessel to the heating system. For that reason, in conventional induction hobs, the possible minimum thickness of the separating material between the coils and the heating vessel is typically 5 mm.

Another load parameter is the vessel size. Our proposed outer squircle-inner circular coils have 75 mm side lengths and are designed to match the minimum vessel dimensions (such as a coffee pot), which is commonly set to be 75 mm by most of the manufacturers. Since vessels with sizes larger than 75 mm completely cover the coils, the designed coils show better performances for plates that have sizes larger than 75 mm. In addition, in many induction cooktops burners are employed to heat up vessels with diameters of 7 inches (approximately 180 mm) and 8 inches (approximately 200 mm) at maximum. Since both plates cover side-by-side placed coils completely and overflow them, transferred powers calculated for the plates that have diameters of 180 mm and 240 mm are the same (We indeed demonstrated this with 3D EM simulations but to not make the thesis too long and more complicated these simulation results are not involved in the thesis). Therefore, here power transfer results of the plates with diameters larger than 180 mm are not represented. Instead, systems with plates that have diameters between 75 mm and 180 mm are investigated.

On the other hand, efficient heating of a vessel with very large dimensions is possible with the proposed coil array. For such vessel's heating, more than 2 coils might be necessary to be powered up. However, if we think each 4 coils placed in square lattice as a unit cell then heating efficiency enhancement would be much higher than that obtained with double coils. Total coupling of the four coils unit cell, i.e., coil's coupling in this unit cell and the unit cells' coupling among themselves, are higher with the proposed coil architecture and applied phase difference than the couplings observed in traditional induction heaters, in which circular coils are driven without phase difference. With constructed simple all-surface inductive heating system setup that consists of 9 of the outer squircle-inner circular coils aligned in a 2D 3×3 square lattice, it has been proved that efficient and almost constant speed heating of vessels with any size and placed

anywhere on the hob is achievable with the proposed outer squircle-inner circular coils. Measurements and results are given in detail in the fourth chapter of this thesis.

Moreover, the other load parameter is vessel material. Because of its high permeability and high resistivity (low conductivity) stainless steel (AISI 430) is one of the best vessel materials to be used for inductive heating. On the other hand, because of its low magnetic permeability and low resistivity (high conductivity) aluminum is one of the most inappropriate vessel materials to be used in inductive heating. Here, we have systematical studies with stainless steel and aluminum plates. To further investigate heating effect of plate material parameter, we also have simulations with plates that are made of materials having relative permeability (μ_r) of 10000 and 1, electrical conductivity (σ) of $1{\times}10^6$ S/m and $1{\times}10^8$ S/m. The minimum and the maximum relative permeabilities were selected to be lower and higher than those of the vessel materials such as aluminum, copper, stainless steel types, etc. Similarly, electrical conductivity range was set to contain electrical conductivity values of the commonly used metal and metal alloys.

We first investigated the system with stainless steel (AISI 430) plate having 180 mm, 120 mm and 75 mm diameters and being located 20 mm, 14 mm and 5 mm above the coils. As we explained above, these parameters were selected to be specific for inductive heating hob system applications. Simulation parameters were set to be equal to the minimum and maximum of the ranges together with a value within the ranges. Powers transferred to the plate were calculated and the results are illustrated in Figure A.1. In Table A.1, these calculated transferred powers (P_{plate}) and the increases in the system's equivalent resistance due to plate's loading (R_{plate}), which are related with power transferred to the plates, are given. Note that in the tables, to indicate them better, the highest calculated power and resistance values are typed bold.

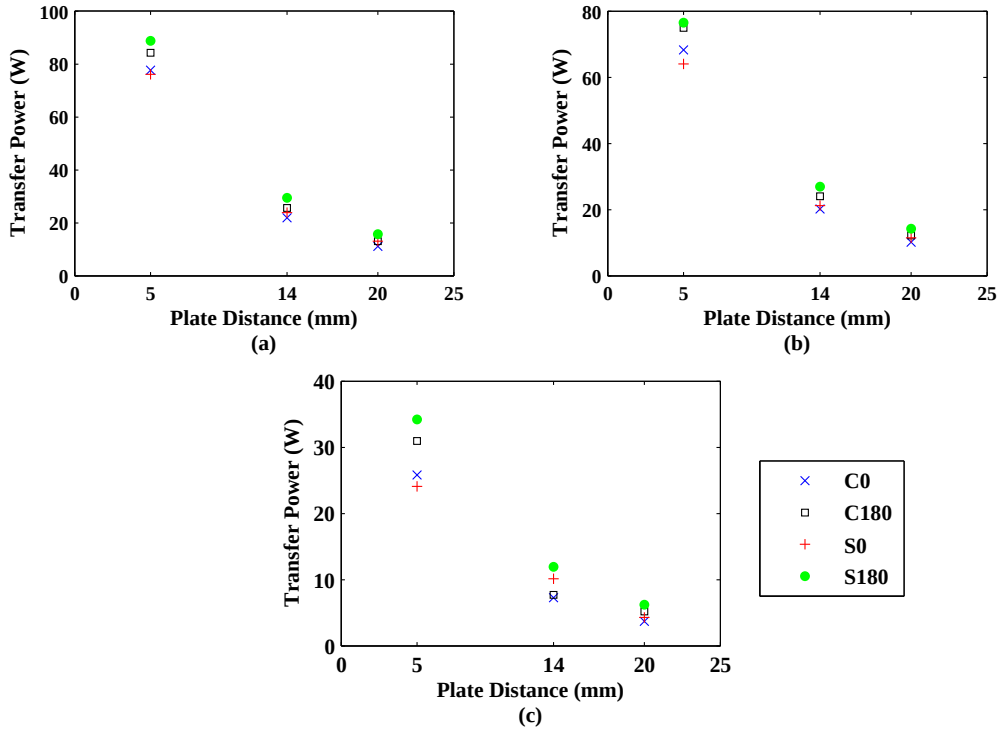

Figure A.1: Power transfer as a function of plate distance for systems in which pair of circular and squircle coils are driven with the 0° and 180° phase differences and steel (AISI 430) plate with diameter of (a) 180 mm, (b) 120 mm, and (c) 75 mm is located. Here labels S0 and S180 correspond to the systems in which squircle coils are driven with the 0° and 180° phase differences, respectively. Similarly, C0 and C180 represent the systems where circular coils are driven with the 0° and 180° phase differences.

Table A.1: Calculated power transferred to the plate (P_{plate}) and increase in the system's equivalent resistance due to plate's loading (R_{plate}) for systems with steel (AISI 430) plate having 180 mm, 120 mm and 75 mm diameters and being located 20 mm, 14 mm and 5 mm above the coils.

Plate Diameter (mm)	Plate-Coil Distance (mm)	Phase Difference ($^{\circ}C$)	Outer Squircle-Inner Circular		Circular	
			P_{plate} (W)	R_{plate} (Ω)	P_{plate} (W)	R_{plate} (Ω)
180 [Figure A.1(a)]	20	0	13.050	2.088	11.128	1.780
		180	**15.784**	**2.525**	13.125	2.100
	14	0	23.917	3.827	21.869	3.499
		180	**29.505**	**4.721**	25.589	4.094
	5	0	76.100	12.176	77.710	12.434
		180	**88.743**	**14.199**	84.231	13.477
120 [Figure A.1(b)]	20	0	11.470	1.835	10.158	1.625
		180	**14.229**	**2.277**	12.197	1.952
	14	0	21.226	3.396	20.224	3.236
		180	**26.925**	**4.308**	24.062	3.850
	5	0	64.029	10.245	68.275	10.924
		180	**76.491**	**12.239**	74.906	11.985
75 [Figure A.1(c)]	20	0	4.279	0.685	3.698	0.592
		180	**6.232**	**0.997**	5.183	0.829
	14	0	10.156	1.625	7.283	1.165
		180	**11.930**	**1.909**	7.693	1.231
	5	0	24.116	3.859	25.827	4.132
		180	**34.231**	**5.477**	30.954	4.953

In the systems, as expected, the highest power transfer values are obtained with the proposed outer squircle-inner circular coil pairs driven by the 180° phase difference. In addition, in all cases efficiency enhancement with the 180° phase difference application is seen, too. For instance, the calculated power for the 75 mm plate located 5 mm above the circular coils that are driven with the 180°

phase difference is larger than that calculated for the plate located 5 mm above the circular coils that are driven with the 0° phase difference. Also, in the systems transferred power decreases as the plate gets smaller and is located further away from the coils.

We repeated simulations with the aluminum plate. Calculated power transfer values are shown in Figure A.2 and they are given in Table A.2 together with the corresponding resistance enhancement values.

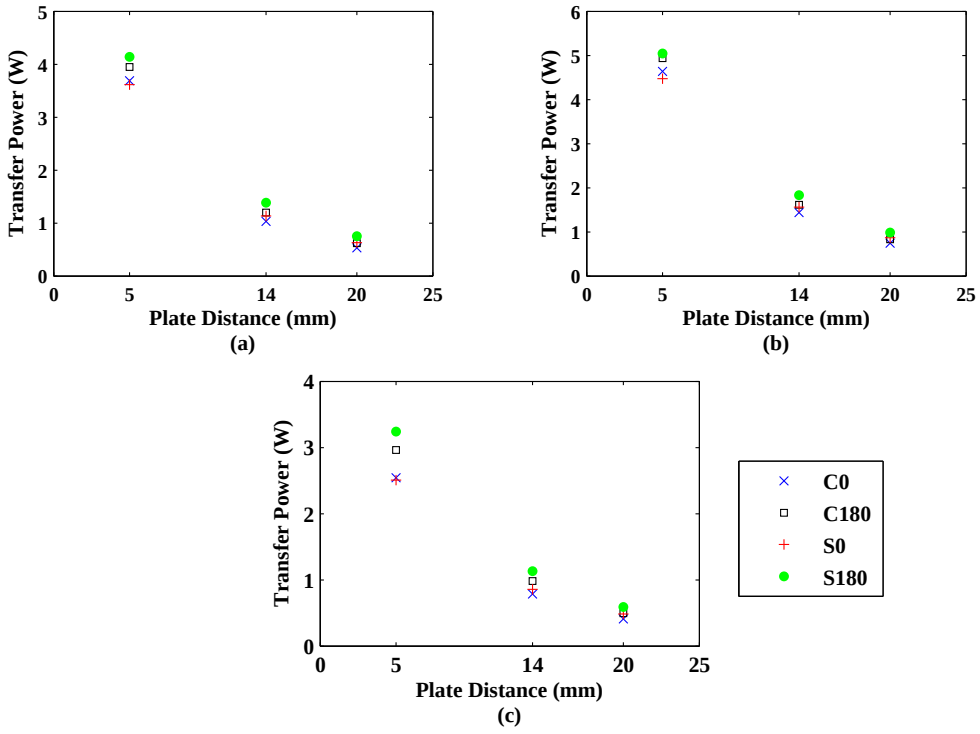

Figure A.2: Power transfer as a function of plate distance for systems in which pair of circular and squircle coils are driven with the 0° and 180° phase differences and aluminum plate with diameter of (a) 180 mm, (b) 120 mm, and (c) 75 mm is located. Here labels S0 and S180 correspond to the systems in which squircle coils are driven with the 0° and 180° phase differences, respectively. Similarly, C0 and C180 represent the systems where circular coils are driven with the 0° and 180° phase differences.

Table A.2: Calculated power transferred to the plate (P_{plate}) and increase in the system's equivalent resistance due to plate's loading (R_{plate}) for systems with aluminum plate having 180 mm, 120 mm and 75 mm diameters and being located 20 mm, 14 mm and 5 mm above the coils.

Plate Diameter (mm)	Plate-Coil Distance (mm)	Phase Difference ($^\circ C$)	Outer Squircle-Inner Circular		Circular	
			P_{plate} (W)	R_{plate} (Ω)	P_{plate} (W)	R_{plate} (Ω)
180 [Figure A.2(a)]	20	0	0.6320	0.1011	0.5329	0.0853
		180	**0.7533**	**0.1205**	0.6211	0.0994
	14	0	1.134	0.181	1.034	0.165
		180	**1.385**	**0.222**	1.200	0.192
	5	0	3.613	0.578	3.689	0.590
		180	**4.140**	**0.662**	3.950	0.632
120 [Figure A.2(b)]	20	0	0.8675	0.1388	0.7453	0.1192
		180	**0.9881**	**0.1581**	0.8340	0.1334
	14	0	1.561	0.250	1.436	0.230
		180	**1.830**	**0.293**	1.614	0.258
	5	0	4.472	0.716	4.636	0.742
		180	**5.046**	**0.807**	4.937	0.790
75 [Figure A.2(c)]	20	0	0.4845	0.0775	0.4111	0.0658
		180	**0.5893**	**0.0943**	0.4971	0.0795
	14	0	0.8583	0.1373	0.7871	0.1259
		180	**1.131**	**0.181**	0.9811	0.1570
	5	0	2.506	0.401	2.543	0.407
		180	**3.240**	**0.518**	2.963	0.474

Here similar observations within the steel plate simulations are made. For example, the highest power transferred to the plate is found for the systems where the proposed outer squircle-inner circular coil pairs are driven with the 180° phase difference. In addition, efficiency enhancement with the 180° phase difference application is observed, too. In each case, power transferred to the

plate is larger when 180° phase difference is applied than that obtained for the 0° phase difference. Also, power transfer values increase as the plate gets closer to the coils.

Although transferred power was expected to be increased with the plate size, it is found to be smaller in systems where aluminum plate with 180 mm diameter is used than that calculated in systems where aluminum plate with 120 mm diameter is located. However, as we stated the highest power transfer values are still obtained with pair of the proposed outer squircle-inner circular coils that are driven with the 180° phase difference.

Simulations were further carried out at 20 kHz and 100 kHz frequencies. They are the highest and the lowest frequencies at which conventional induction hobs operate. As in 50 kHz simulations, the highest power transfer is obtained in systems where the proposed outer squircle-inner circular coils are driven by 180° phase difference.

Moreover, we had simulations with plates that have electrical conductivities (σ) and relative magnetic permeabilities (μ_r) different from those of aluminum and AISI 430 steel. As it is explained above, relative permeabilities are set 10000 and 1. Similarly, electrical conductivities are decided to be $1{\times}10^6$ S/m and $1{\times}10^8$ S/m. We first systematically studied the systems with plate that have relative permeability and electrical conductivity equal to 1 and $1{\times}10^6$ S/m, respectively. Powers transferred to the plate are calculated and shown in Figure A.3. Also, power transfer values (P_{plate}) and increases in the system's equivalent resistance due to plate's loading (R_{plate}) are given in Table A.3.

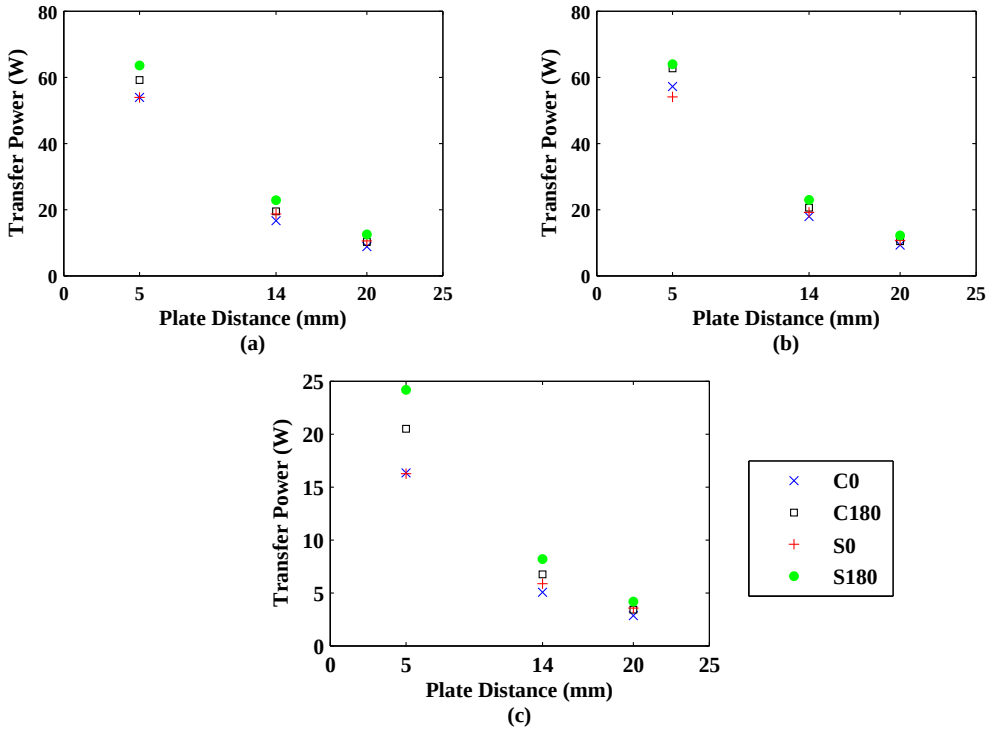

Figure A.3: Power transfer as a function of plate distance for systems in which pair of circular and squircle coils are driven with the 0° and 180° phase differences and plate made of a newly defined material that has relative permeability (μ_r) and electrical conductivity (σ) equal to 1 and $1{\times}10^6$ S/m, respectively, with diameter of (a) 180 mm, (b) 120 mm, and (c) 75 mm is located. Here labels S0 and S180 correspond to the systems in which squircle coils are driven with the 0° and 180° phase differences, respectively. Similarly, C0 and C180 represent the systems where circular coils are driven with the 0° and 180° phase differences.

Table A.3: Calculated power transferred to the plate (P_{plate}) and increase in the system's equivalent resistance due to plate's loading (R_{plate}) for systems with the plate made of a newly defined material having 180 mm, 120 mm and 75 mm diameters and being located 20 mm, 14 mm and 5 mm above the coils. Here, the newly defined material has relative permeability (μ_r) equals to 1 and electrical conductivity (σ) equals to 1×10^6 S/m.

Plate Diameter (mm)	Plate-Coil Distance (mm)	Phase Difference ($^\circ C$)	Outer Squircle-Inner Circular		Circular	
			P_{plate} (W)	R_{plate} (Ω)	P_{plate} (W)	R_{plate} (Ω)
180 [Figure A.3(a)]	20	0	10.588	1.694	8.806	1.409
		180	**12.507**	**2.001**	10.244	1.639
	14	0	18.716	2.995	16.694	2.671
		180	**22.870**	**3.659**	19.526	3.124
	5	0	53.960	8.634	53.904	8.625
		180	**63.593**	**10.175**	59.147	9.464
120 [Figure A.3(b)]	20	0	10.711	1.714	9.303	1.488
		180	**12.190**	**1.950**	10.473	1.676
	14	0	19.156	3.065	17.917	2.867
		180	**22.959**	**3.673**	20.563	3.290
	5	0	54.061	8.650	57.214	9.154
		180	**63.937**	**10.230**	62.737	10.038
75 [Figure A.3(c)]	20	0	3.577	0.572	2.845	0.455
		180	**4.176**	**0.668**	3.422	0.548
	14	0	5.875	0.940	5.072	0.812
		180	**8.189**	**1.310**	6.755	1.081
	5	0	16.265	2.602	16.340	2.614
		180	**24.184**	**3.869**	20.494	3.279

We also investigated the system with plate made of another newly defined material that has relative permeability equals to 1 and electrical conductivity equals to 1×10^8 S/m. Calculated power transfer values are illustrated in Figure A.4 for

various plate sizes, which are given in Table A.4 together with the corresponding resistance enhancement values.

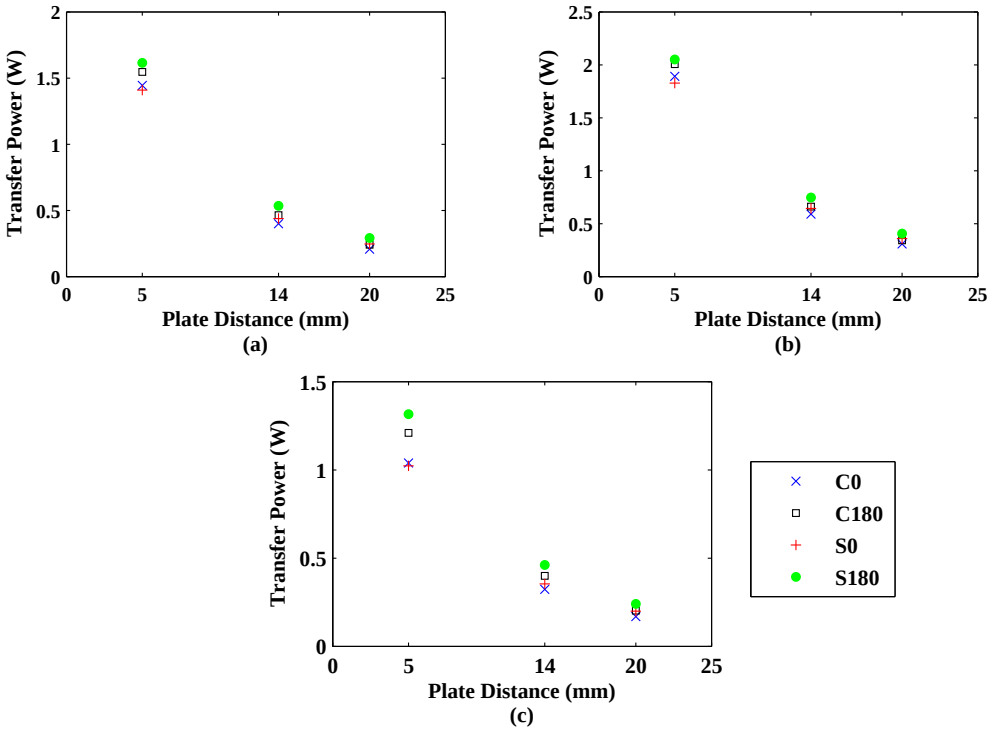

Figure A.4: Power transfer as a function of plate distance for systems in which pair of circular and squircle coils are driven with the 0° and 180° phase differences and plate made of another newly defined material that has relative permeability (μ_r) and electrical conductivity (σ) equal to 1 and $1{\times}10^8$ S/m, respectively, with diameter of (a) 180 mm, (b) 120 mm, and (c) 75 mm is located. Here labels S0 and S180 correspond to the systems in which squircle coils are driven with the 0° and 180° phase differences, respectively. Similarly, C0 and C180 represent the systems where circular coils are driven with the 0° and 180° phase differences.

Table A.4: Calculated power transferred to the plate (P_{plate}) and increase in the system's equivalent resistance due to plate's loading (R_{plate}) for systems with the plate made of another newly defined material having 180 mm, 120 mm and 75 mm diameters and being located 20 mm, 14 mm and 5 mm above the coils. Here, the newly defined material has relative permeability (μ_r) equals to 1 and electrical conductivity (σ) equals to 1×10^8 S/m.

Plate Diameter (mm)	Plate-Coil Distance (mm)	Phase Difference ($^\circ C$)	Outer Squircle-Inner Circular		Circular	
			P_{plate} (W)	R_{plate} (Ω)	P_{plate} (W)	R_{plate} (Ω)
180 [Figure A.4(a)]	20	0	0.2452	0.0392	0.2063	0.0330
		180	**0.2920**	**0.0467**	0.2403	0.0384
	14	0	0.4380	0.0701	0.3994	0.0639
		180	**0.5351**	**0.0856**	0.4632	0.0741
	5	0	1.409	0.225	1.445	0.231
		180	**1.615**	**0.258**	1.546	0.247
120 [Figure A.4(b)]	20	0	0.3599	0.0576	0.3085	0.0494
		180	**0.4059**	**0.0649**	0.3423	0.0548
	14	0	0.6429	0.1029	0.5904	0.0945
		180	**0.7471**	**0.1195**	0.6594	0.1055
	5	0	1.826	0.292	1.890	0.302
		180	**2.050**	**0.328**	2.007	0.321
75 [Figure A.4(c)]	20	0	0.1995	0.0319	0.1687	0.0270
		180	**0.2398**	**0.0384**	0.2021	0.0323
	14	0	0.3534	0.0565	0.3225	0.0516
		180	**0.4603**	**0.0736**	0.3990	0.0638
	5	0	1.023	0.164	1.039	0.166
		180	**1.315**	**0.210**	1.209	0.193

Furthermore, we systematically studied the system with plate made of newly defined material that has relative permeability equals to 10000 and electrical conductivity equals to 1×10^6 S/m. Calculated power transfer results are represented

in Figure A.5 and the values are given in Table A.5.

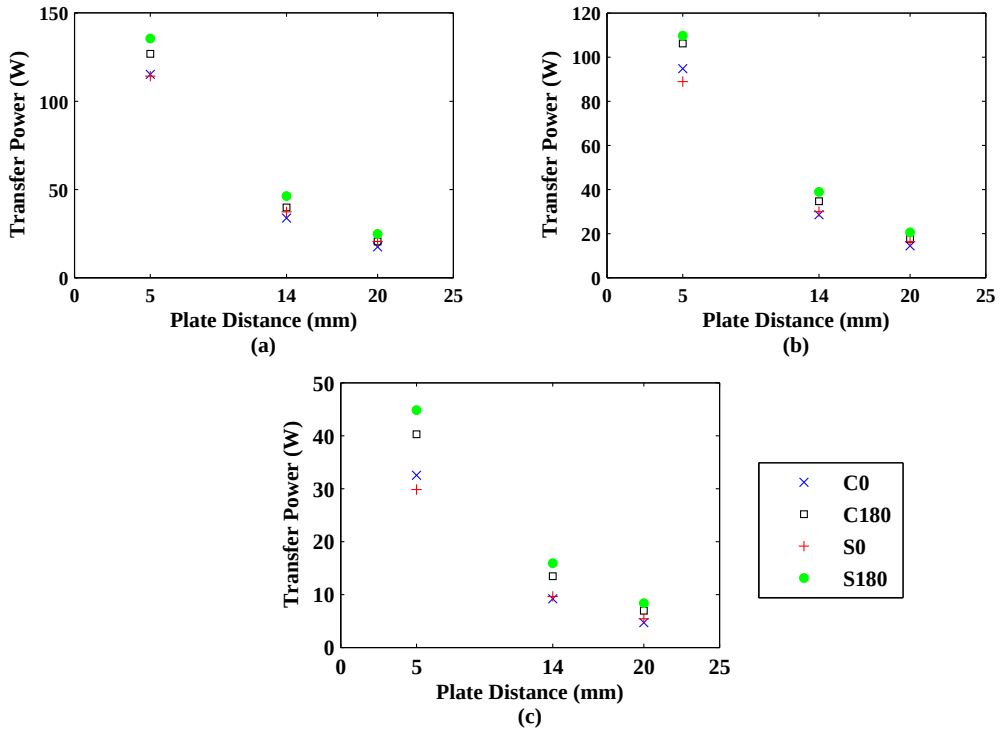

Figure A.5: Power transfer as a function of plate distance for systems in which pair of circular and squircle coils are driven with the 0° and 180° phase differences and plate made of newly defined material that has relative permeability (μ_r) and electrical conductivity (σ) equal to 10000 and $1{\times}10^6$ S/m, respectively, with diameter of (a) 180 mm, (b) 120 mm, and (c) 75 mm is located. Here labels S0 and S180 correspond to the systems in which squircle coils are driven with the 0° and 180° phase differences, respectively. Similarly, C0 and C180 represent the systems where circular coils are driven with the 0° and 180° phase differences.

Table A.5: Calculated power transferred to the plate (P_{plate}) and increase in the system's equivalent resistance due to plate's loading (R_{plate}) for systems with the plate made of newly defined material having 180 mm, 120 mm and 75 mm diameters and being located 20 mm, 14 mm and 5 mm above the coils. Here, the newly defined material has relative permeability (μ_r) equals to 10000 and electrical conductivity (σ) equals to 1×10^6 S/m.

Plate Diameter (mm)	Plate-Coil Distance (mm)	Phase Difference ($^\circ C$)	Outer Squircle-Inner Circular		Circular	
			P_{plate} (W)	R_{plate} (Ω)	P_{plate} (W)	R_{plate} (Ω)
180 [Figure A.5(a)]	20	0	20.556	3.289	17.401	2.784
		180	**24.830**	**3.973**	20.569	3.291
	14	0	37.333	5.973	33.773	5.404
		180	**46.212**	**7.394**	39.802	6.368
	5	0	114.164	18.266	115.214	18.434
		180	**135.547**	**21.688**	126.843	20.295
120 [Figure A.5(b)]	20	0	16.286	2.606	14.383	2.301
		180	**20.553**	**3.288**	17.586	2.814
	14	0	29.969	4.795	28.502	4.560
		180	**38.867**	**6.219**	34.619	5.539
	5	0	88.901	14.224	94.709	15.153
		180	**109.649**	**17.544**	106.225	16.996
75 [Figure A.5(c)]	20	0	5.401	0.864	4.676	0.748
		180	**8.353**	**1.336**	6.912	1.106
	14	0	9.647	1.544	9.193	1.471
		180	**15.884**	**2.541**	13.445	2.151
	5	0	29.845	4.775	32.535	5.206
		180	**44.838**	**7.174**	40.247	6.440

Lastly, we repeated simulations with plate made of another newly defined material that has relative permeability equals to 10000 and electrical conductivity equals to 1×10^8 S/m. Calculated power transferred to the plates are illustrated

in Figure A.6. Also, power values (P_{plate}) and enhancements in the system's equivalent resistance due to plates' loadings (R_{plate}) are given in Table A.6.

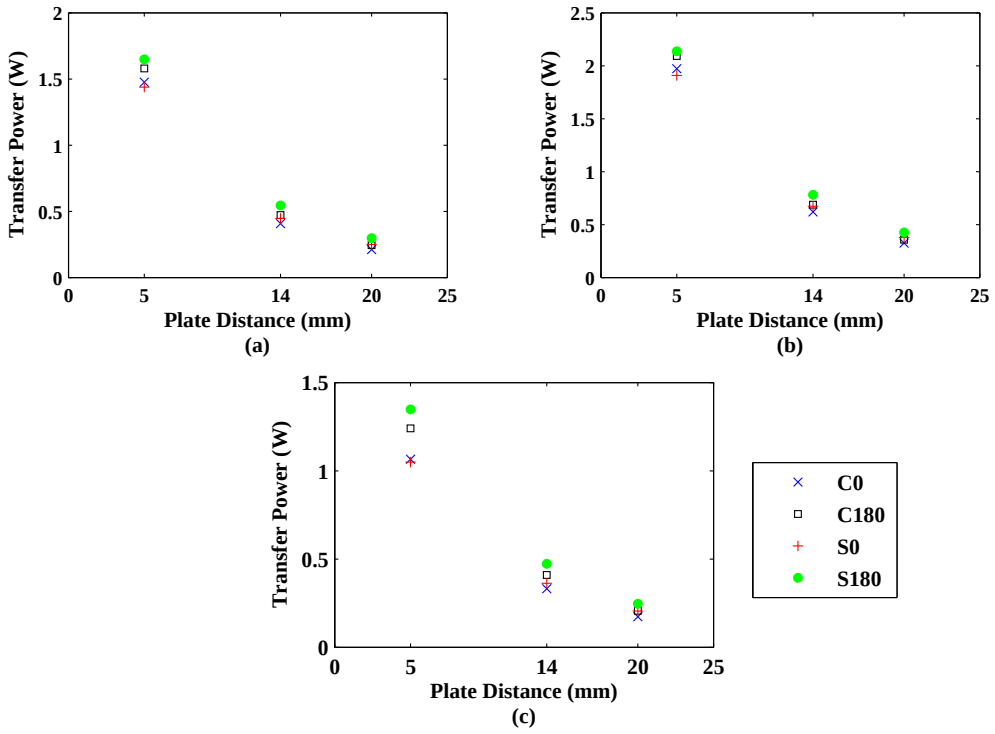

Figure A.6: Power transfer as a function of plate distance for systems in which pair of circular and squircle coils are driven with the 0° and 180° phase differences and plate made of another newly defined material that has relative permeability (μ_r) and electrical conductivity (σ) equal to 10000 and 1×10^8 S/m, respectively, with diameter of (a) 180 mm, (b) 120 mm, and (c) 75 mm is located. Here labels S0 and S180 correspond to the systems in which squircle coils are driven with the 0° and 180° phase differences, respectively. Similarly, C0 and C180 represent the systems where circular coils are driven with the 0° and 180° phase differences.

Table A.6: Calculated power transferred to the plate (P_{plate}) and increase in the system's equivalent resistance due to plate's loading (R_{plate}) for systems with the plate made of another newly defined material having 180 mm, 120 mm and 75 mm diameters and being located 20 mm, 14 mm and 5 mm above the coils. Here, the newly defined material has relative permeability (μ_r) equals to 10000 and electrical conductivity (σ) equals to $1{\times}10^8$ S/m.

Plate Diameter (mm)	Plate-Coil Distance (mm)	Phase Difference ($^\circ C$)	Outer Squircle-Inner Circular		Circular	
			P_{plate} (W)	R_{plate} (Ω)	P_{plate} (W)	R_{plate} (Ω)
180 [Figure A.6(a)]	20	0	0.2499	0.0400	0.2101	0.0336
		180	**0.2975**	**0.0476**	0.2447	0.0392
	14	0	0.4458	0.0713	0.4064	0.0650
		180	**0.5447**	**0.0872**	0.4713	0.0754
	5	0	1.438	0.230	1.476	0.236
		180	**1.649**	**0.264**	1.580	0.253
120 [Figure A.6(b)]	20	0	0.3778	0.0604	0.3236	0.0518
		180	**0.4244**	**0.0679**	0.3578	0.0572
	14	0	0.6737	0.1078	0.6181	0.0989
		180	**0.7799**	**0.1248**	0.6884	0.1101
	5	0	1.907	0.305	1.973	0.316
		180	**2.136**	**0.342**	2.093	0.335
75 [Figure A.6(c)]	20	0	0.2051	0.0328	0.1733	0.0277
		180	**0.2460**	**0.0394**	0.2072	0.0332
	14	0	0.3632	0.0581	0.3310	0.0530
		180	**0.4721**	**0.0755**	0.4090	0.0654
	5	0	1.050	0.168	1.066	0.171
		180	**1.348**	**0.216**	1.240	0.198

In all the calculations, where plates have relative permeabilities and electrical conductivities different from those of the stainless steel and aluminum but contain all the possible permeability and conductivity values of vessel materials

appropriate to be used for inductive heating, the highest power transfer values are found in systems where the proposed outer squircle-inner circular coil pairs are driven with the 180° phase difference. The same observation was previously made with stainless steel (AISI 430) and aluminum plates, too. In addition, it is also seen that the transferred power to the plates increases as the plate gets closer to the coils. This was again seen in stainless steel and aluminum plate simulations, too.

In conclusion, all the results illustrated in the figures and given in the tables show that the proposed outer squircle-inner circular coils that are driven with the 180° phase difference display better performances than those of the conventional circular coils for the possible loading conditions that are specific to inductive heating applications. In other words, in inductive heating hob systems loading parameters, i.e., size, distance and material, have specific ranges for efficient heating, and for all the possible loadings that have parameters within these ranges specific to inductive heating systems the proposed outer squircle-inner circular coils exhibit better performance than that of the circular coils. The proposed outer squircle-inner circular coils might exhibit worse efficiency under some load parameters. However, these parameters are not in the range of common inductive heating applications.

We have further investigated power transfer efficiencies of systems with plates placed at different positions. In the previously examined systems, plate was located such that its center was right on the midpoint of the two side-by-side placed coils. We have repeated calculations for the systems in which plate was displaced by 12.5 mm, 25 mm, and 37.5 mm on constant planes that are 5 mm, 14 mm and 20 mm above the coils. The maximum displacement was chosen as 37.5 mm because with 37.5 mm displacement, plate's center and center of one of the two side-by-side placed coils coincide, i.e., they are on top of each other. In all-surface designs array of coils are used. In all-surface systems if plate's center have distance larger than 37.5 mm on constant horizontal plane with respect to two side-by-side placed coils' midpoint then there is another pair of side-by-side placed coils whose midpoint is closer than 37.5 mm to the plate's center on constant horizontal plane. It means, in our proposed all-surface heating system

each repeating cell has 75 mm side lengths and thus plate's 37.5 mm displacement is the length enough to cover each unit cell.

Simulations were conducted for aluminum and stainless steel (AISI 430) plates that have 180 mm, 120 mm, and 75 mm diameters and being located 20 mm, 14 mm, and 5 mm above the coils. We first studied the system with the stainless steel (AISI 430) plate that was displaced by 12.5 mm with respect to midpoint of the two side-by-side placed coils. Calculated powers transferred to the plate are represented in Figure A.7 and given in Table A.7 together with increases in the system's equivalent resistance due to plate's loading.

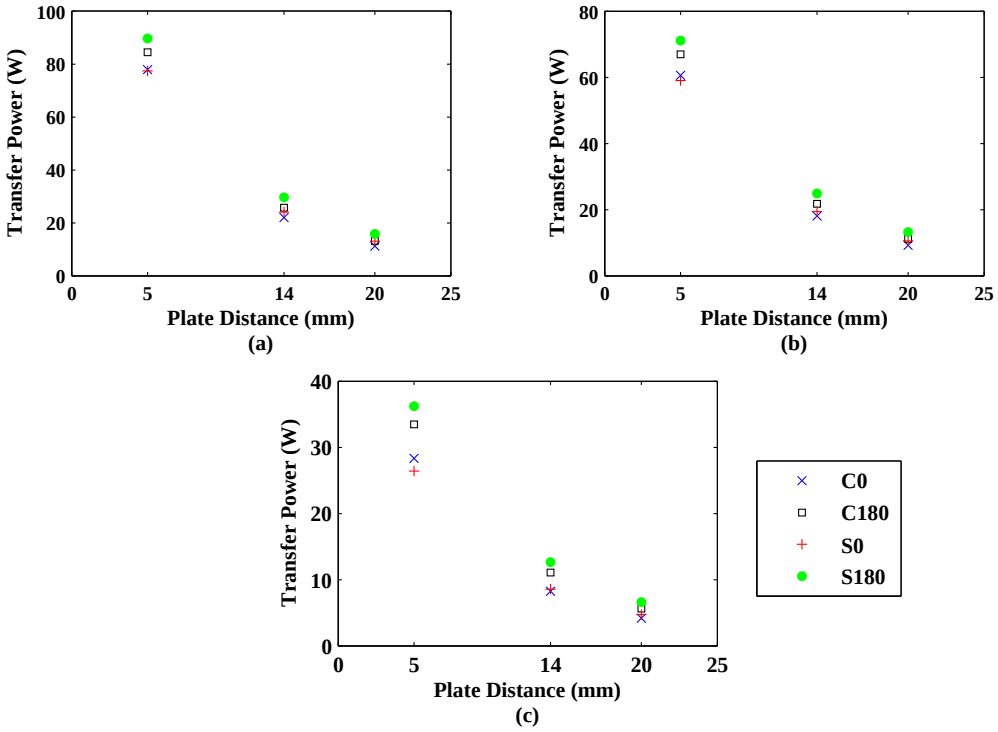

Figure A.7: Power transfer as a function of plate distance for systems in which pair of circular and squircle coils are driven with the 0° and 180° phase differences and steel plate with diameter of (a) 180 mm, (b) 120 mm, and (c) 75 mm is located. Here, the distance between the plate's center and the side-by-side placed coils' midpoint is 12.5 mm on a constant horizontal plane. In the figure, labels S0 and S180 correspond to the systems in which squircle coils are driven with the 0° and 180° phase differences, respectively. Similarly, C0 and C180 represent the systems where circular coils are driven with the 0° and 180° phase differences.

Table A.7: Calculated power transferred to the plate (P_{plate}) and increase in the system's equivalent resistance due to plate's loading (R_{plate}) for systems with stainless steel (AISI 430) plate having 180 mm, 120 mm and 75 mm diameters and being located 20 mm, 14 mm and 5 mm above the coils. Here, the distance between the plate's center and the side-by-side placed coils' midpoint is 12.5 mm on a constant horizontal plane.

Plate Diameter (mm)	Plate-Coil Distance (mm)	Phase Difference ($^{\circ}C$)	Outer Squircle-Inner Circular		Circular	
			P_{plate} (W)	R_{plate} (Ω)	P_{plate} (W)	R_{plate} (Ω)
180 [Figure A.7(a)]	20	0	13.087	2.094	11.182	1.789
		180	**15.808**	**2.529**	13.170	2.107
	14	0	24.055	3.849	21.991	3.519
		180	**29.621**	**4.739**	25.705	4.113
	5	0	77.387	12.382	77.904	12.465
		180	**89.681**	**14.349**	84.488	13.518
120 [Figure A.7(b)]	20	0	10.577	1.692	9.187	1.470
		180	**13.221**	**2.115**	11.148	1.784
	14	0	19.445	3.111	18.068	2.891
		180	**24.931**	**3.989**	21.754	3.481
	5	0	59.000	9.440	60.587	9.694
		180	**71.088**	**11.374**	66.956	10.713
75 [Figure A.7(c)]	20	0	4.719	0.755	4.172	0.668
		180	**6.593**	**1.055**	5.615	0.898
	14	0	8.569	1.371	8.243	1.319
		180	**12.653**	**2.024**	11.060	1.770
	5	0	26.426	4.228	28.323	4.532
		180	**36.208**	**5.793**	33.475	5.356

Simulations were repeated with the aluminum plate. Power transfer results of the new system are shown in Figure A.8. Also, the power transfer results and the corresponding resistance enhancement values are given in Table A.8.

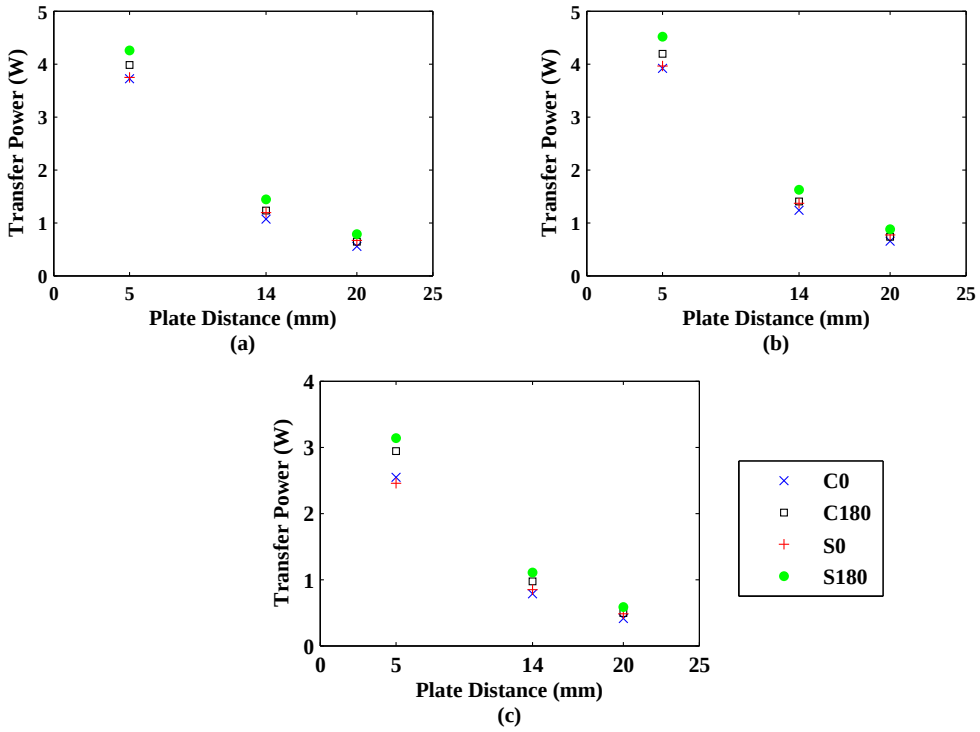

Figure A.8: Power transfer as a function of plate distance for systems in which pair of circular and squircle coils are driven with the 0° and 180° phase differences and aluminum plate with diameter of (a) 180 mm, (b) 120 mm, and (c) 75 mm is located. Here, the distance between the plate's center and the side-by-side placed coils' midpoint is 12.5 mm on a constant horizontal plane. In the figure, labels S0 and S180 correspond to the systems in which squircle coils are driven with the 0° and 180° phase differences, respectively. Similarly, C0 and C180 represent the systems where circular coils are driven with the 0° and 180° phase differences.

Table A.8: Calculated power transferred to the plate (P_{plate}) and increase in the system's equivalent resistance due to plate's loading (R_{plate}) for systems with aluminum plate having 180 mm, 120 mm and 75 mm diameters and being located 20 mm, 14 mm and 5 mm above the coils. Here, the distance between the plate's center and the side-by-side placed coils' midpoint is 12.5 mm on a constant horizontal plane.

Plate Diameter (mm)	Plate-Coil Distance (mm)	Phase Difference ($^{\circ}C$)	Outer Squircle-Inner Circular		Circular	
			P_{plate} (W)	R_{plate} (Ω)	P_{plate} (W)	R_{plate} (Ω)
180 [Figure A.8(a)]	20	0	0.6673	0.1068	0.5570	0.0891
		180	**0.7853**	**0.1256**	0.6431	0.1029
	14	0	1.195	0.191	1.071	0.171
		180	**1.442**	**0.231**	1.234	0.197
	5	0	3.748	0.600	3.721	0.595
		180	**4.258**	**0.681**	3.985	0.638
120 [Figure A.8(b)]	20	0	0.7711	0.1234	0.6548	0.1048
		180	**0.8809**	**0.1409**	0.7354	0.1177
	14	0	1.372	0.220	1.240	0.198
		180	**1.624**	**0.260**	1.404	0.225
	5	0	3.965	0.634	3.919	0.627
		180	**4.515**	**0.722**	4.195	0.671
75 [Figure A.8(c)]	20	0	0.4843	0.0775	0.4118	0.0659
		180	**0.5855**	**0.0937**	0.4959	0.0793
	14	0	0.8479	0.1357	0.7858	0.1257
		180	**1.107**	**0.177**	0.9730	0.1557
	5	0	2.455	0.393	2.548	0.408
		180	**3.141**	**0.503**	2.943	0.471

Next, we investigated the systems with the stainless steel and the aluminum plates that were displaced by 25 mm with respect to midpoint of the two side-by-side placed coils. For the stainless steel plate simulations, calculated power

transferred to the plates are shown in Figure A.9. Also, these power transfer (P_{plate}) values and increases in the system's equivalent resistance due to plate's loading (R_{plate}) are given in Table A.9.

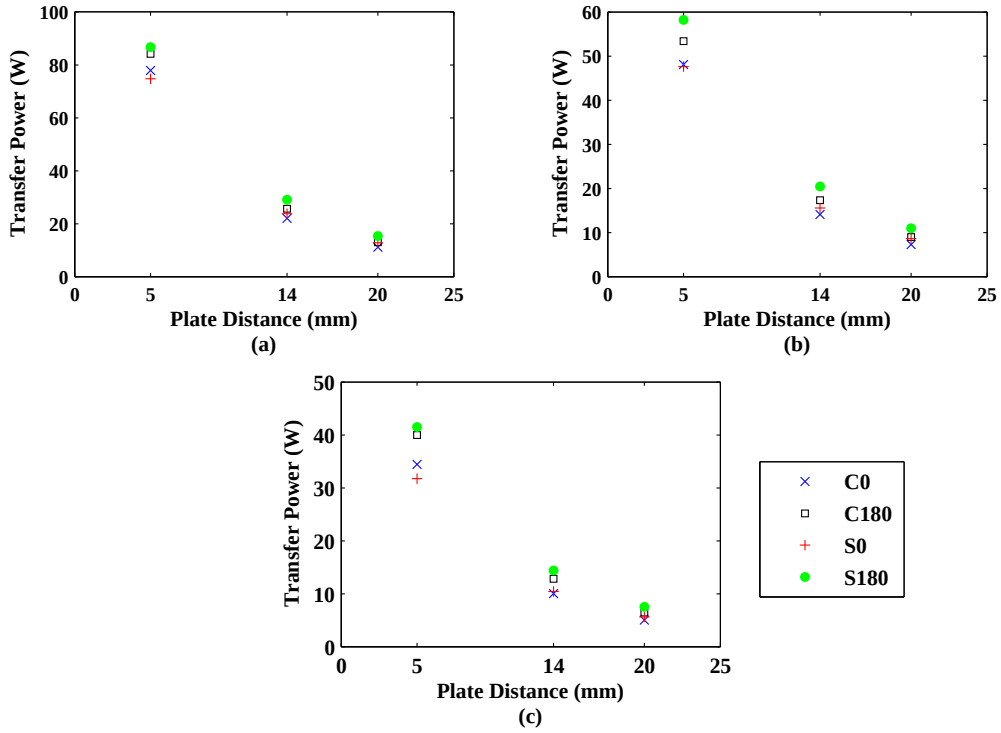

Figure A.9: Power transfer as a function of plate distance for systems in which pair of circular and squircle coils are driven with the 0° and 180° phase differences and steel plate with diameter of (a) 180 mm, (b) 120 mm, and (c) 75 mm is located. Here, the distance between the plate's center and the side-by-side placed coils' midpoint is 25 mm on a constant horizontal plane. In the figure, labels S0 and S180 correspond to the systems in which squircle coils are driven with the 0° and 180° phase differences, respectively. Similarly, C0 and C180 represent the systems where circular coils are driven with the 0° and 180° phase differences.

Table A.9: Calculated power transferred to the plate (P_{plate}) and increase in the system's equivalent resistance due to plate's loading (R_{plate}) for systems with stainless steel (AISI 430) plate having 180 mm, 120 mm and 75 mm diameters and being located 20 mm, 14 mm and 5 mm above the coils. Here, the distance between the plate's center and the side-by-side placed coils' midpoint is 25 mm on a constant horizontal plane.

Plate Diameter (mm)	Plate-Coil Distance (mm)	Phase Difference ($^\circ C$)	Outer Squircle-Inner Circular		Circular	
			P_{plate} (W)	R_{plate} (Ω)	P_{plate} (W)	R_{plate} (Ω)
180 [Figure A.9(a)]	20	0	12.794	2.047	11.116	1.779
		180	**15.372**	**2.460**	13.006	2.081
	14	0	23.726	3.796	22.049	3.528
		180	**29.087**	**4.654**	25.620	4.099
	5	0	74.772	11.964	77.889	12.462
		180	**86.732**	**13.877**	84.194	13.471
120 [Figure A.9(b)]	20	0	8.601	1.376	7.237	1.158
		180	**10.962**	**1.754**	8.998	1.440
	14	0	15.548	2.488	14.069	2.251
		180	**20.427**	**3.268**	17.345	2.775
	5	0	47.597	7.616	48.077	7.692
		180	**58.195**	**9.311**	53.408	8.545
75 [Figure A.9(c)]	20	0	5.605	0.897	5.019	0.803
		180	**7.501**	**1.200**	6.457	1.033
	14	0	10.411	1.666	10.026	1.604
		180	**14.410**	**2.306**	12.823	2.052
	5	0	31.743	5.079	34.436	5.510
		180	**41.492**	**6.639**	39.973	6.396

Similarly, in systems with the aluminum plates whose centers are 25 mm away from the side-by-side placed coils' midpoint, power transferred to the plates were calculated. The results are illustrated in Figure A.10 and the values are given in

Table A.10 together with the increases in the system's equivalent resistance due to plate's loading.

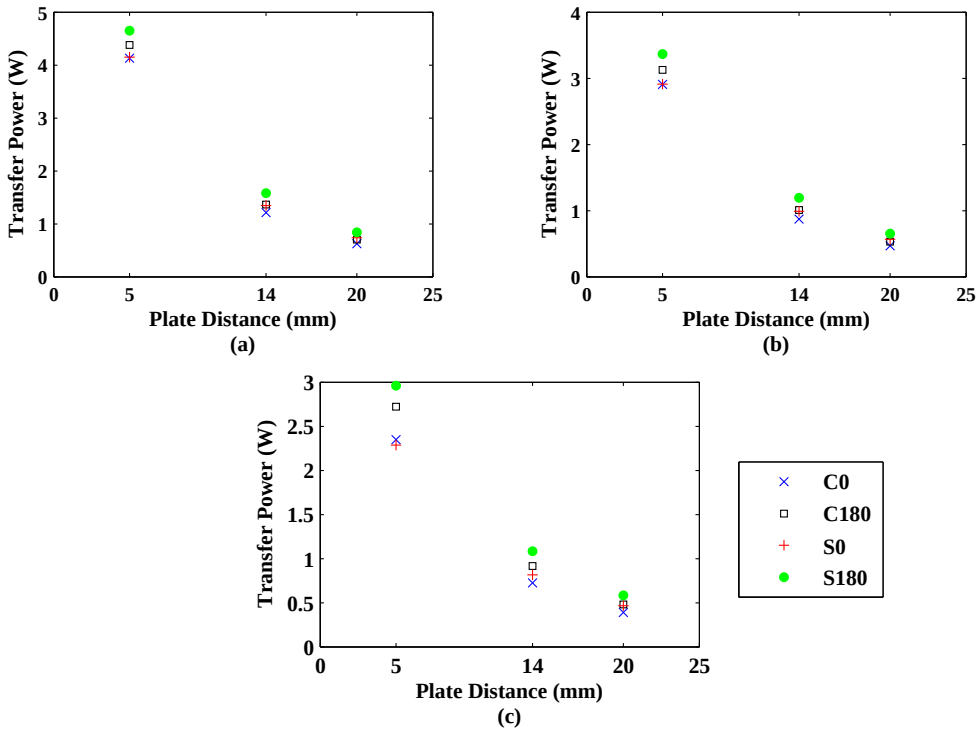

Figure A.10: Power transfer as a function of plate distance for systems in which pair of circular and squircle coils are driven with the 0° and 180° phase differences and aluminum plate with diameter of (a) 180 mm, (b) 120 mm, and (c) 75 mm is located. Here, the distance between the plate's center and the side-by-side placed coils' midpoint is 25 mm on a constant horizontal plane. In the figure, labels S0 and S180 correspond to the systems in which squircle coils are driven with the 0° and 180° phase differences, respectively. Similarly, C0 and C180 represent the systems where circular coils are driven with the 0° and 180° phase differences.

Table A.10: Calculated power transferred to the plate (P_{plate}) and increase in the system's equivalent resistance due to plate's loading (R_{plate}) for systems with aluminum plate having 180 mm, 120 mm and 75 mm diameters and being located 20 mm, 14 mm and 5 mm above the coils. Here, the distance between the plate's center and the side-by-side placed coils' midpoint is 25 mm on a constant horizontal plane.

Plate Diameter (mm)	Plate-Coil Distance (mm)	Phase Difference ($^\circ C$)	Outer Squircle-Inner Circular		Circular	
			P_{plate} (W)	R_{plate} (Ω)	P_{plate} (W)	R_{plate} (Ω)
180 [Figure A.10(a)]	20	0	0.7370	0.1179	0.6264	0.1002
		180	**0.8415**	**0.1346**	0.7029	0.1125
	14	0	1.348	0.216	1.214	0.194
		180	**1.579**	**0.253**	1.366	0.219
	5	0	4.150	0.664	4.128	0.660
		180	**4.648**	**0.744**	4.379	0.701
120 [Figure A.10(b)]	20	0	0.5665	0.0906	0.4669	0.0747
		180	**0.6510**	**0.1042**	0.5309	0.0849
	14	0	0.9889	0.1582	0.8721	0.1395
		180	**1.194**	**0.191**	1.008	0.161
	5	0	2.911	0.466	2.909	0.465
		180	**3.365**	**0.538**	3.126	0.500
75 [Figure A.10(c)]	20	0	0.4674	0.0748	0.3899	0.0624
		180	**0.5824**	**0.0932**	0.4821	0.0771
	14	0	0.8157	0.1305	0.7262	0.1162
		180	**1.084**	**0.173**	0.9175	0.1468
	5	0	2.286	0.366	2.349	0.376
		180	**2.960**	**0.474**	2.723	0.436

Last, simulations with the plates that are displaced by 37.5 mm on constant horizontal planes with respect to midpoint of the two side-by-side placed coils were conducted. For the steel plate simulations, calculated power transferred to

the plates are shown in Figure A.11. Transfer power values and increases in the system's equivalent resistance due to plates' loadings are given in Table A.11.

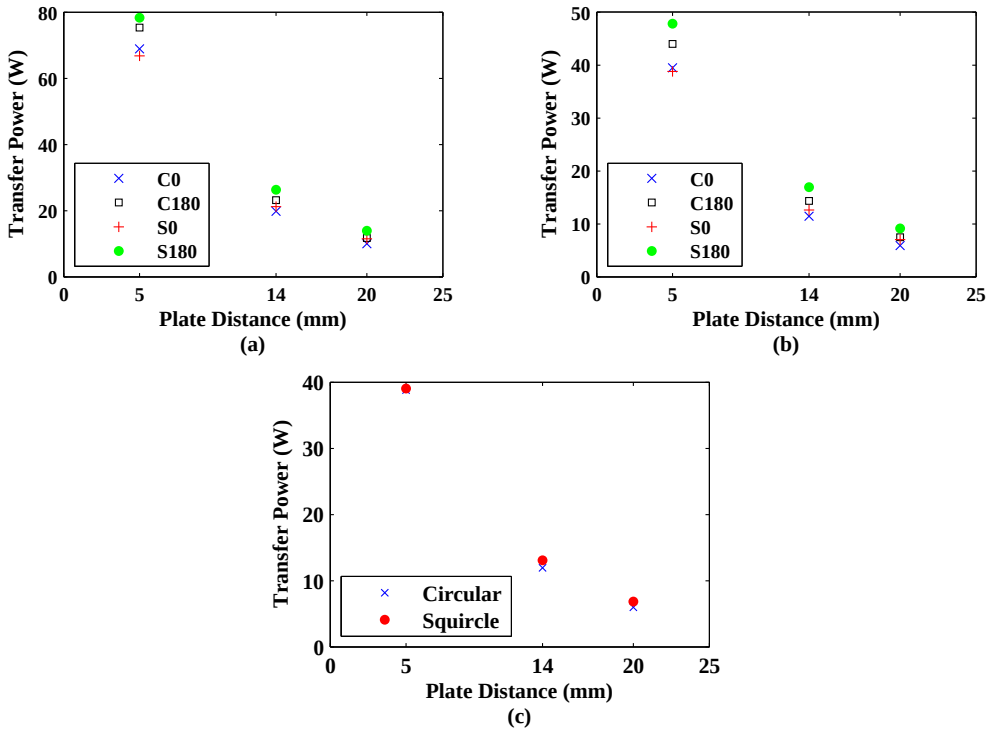

Figure A.11: Power transfer as a function of plate distance for systems in which pair of circular and squircle coils are driven with the 0° and 180° phase differences and steel plate with diameter of (a) 180 mm, (b) 120 mm, and (c) 75 mm is located. Here, the distance between the plate's center and the side-by-side placed coils' midpoint is 37.5 mm on a constant horizontal plane. In subfigures (a) and (b), labels S0 and S180 correspond to the systems in which squircle coils are driven with the 0° and 180° phase differences, respectively. Similarly, C0 and C180 represent the systems where circular coils are driven with the 0° and 180° phase differences. In subfigure (c), on the other hand, labels circular and squircle represent the systems in which single circular and single squircle coil is driven.

Table A.11: Calculated power transferred to the plate (P_{plate}) and increase in the system's equivalent resistance due to plate's loading (R_{plate}) for systems with stainless steel (AISI 430) plate having 180 mm, 120 mm and 75 mm diameters and being located 20 mm, 14 mm and 5 mm above the coils. Here, the distance between the plate's center and the side-by-side placed coils' midpoint is 37.5 mm on a constant horizontal plane.

Plate Diameter (mm)	Plate-Coil Distance (mm)	Phase Difference ($^\circ C$)	Outer Squircle-Inner Circular		Circular	
			P_{plate} (W)	R_{plate} (Ω)	P_{plate} (W)	R_{plate} (Ω)
180 [Figure A.11(a)]	20	0	11.504	1.841	9.999	1.600
		180	**13.905**	**2.225**	11.756	1.881
	14	0	21.218	3.395	19.819	3.171
		180	**26.327**	**4.212**	23.196	3.711
	5	0	66.769	10.683	68.932	11.029
		180	**78.345**	**12.535**	75.333	12.053
120 [Figure A.11(b)]	20	0	7.051	1.128	5.903	0.944
		180	**9.134**	**1.461**	7.467	1.195
	14	0	12.631	2.021	11.459	1.833
		180	**16.922**	**2.708**	14.351	2.296
	5	0	38.818	6.211	39.506	6.321
		180	**47.839**	**7.654**	43.980	7.037
75 [Figure A.11(c)]	20	X	**6.857**	**1.097**	5.981	0.957
	14	X	**13.092**	**2.095**	11.942	1.911
	5	X	**39.052**	**6.248**	38.812	6.210

Note that in the systems where the plate having 75 mm diameter is displaced by 37.5 mm on a constant horizontal plane with respect to midpoint of the two side-by-side placed coils, only one coil is powered up. Since coils have 75 mm side lengths, plate with 75 mm diameter does not extend a coil if it is right on top of the coil. This is the reason why in Figure A.11(c) and Figure A.12(c), instead of four legends, there are only two legends that indicate the coil geometry. Similarly,

in the last three rows in Table A.11 and Table A.12, the column indicating the applying phase difference is assigned with X.

Similarly, for the aluminum plate simulations, calculated powers transferred to the plate are represented in Figure A.12. Also, the transferred powers to the plate (P_{plate}) and increases in the system's equivalent resistance due to plate's loading (R_{plate}) are given in Table A.12.

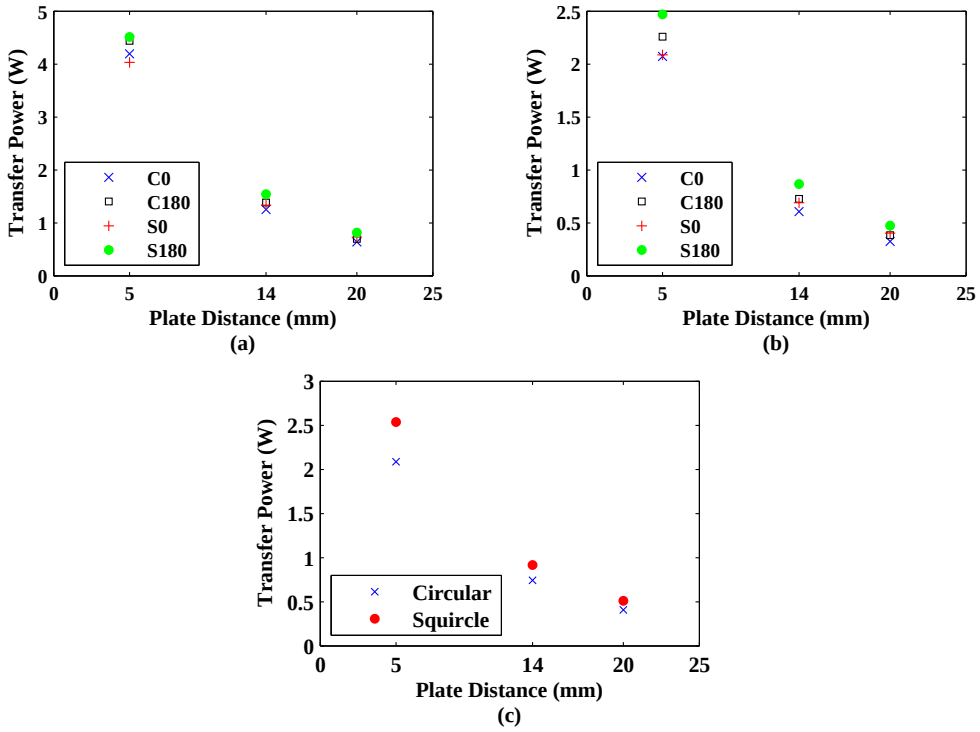

Figure A.12: Power transfer as a function of plate distance for systems in which pair of circular and squircle coils are driven with the 0° and 180° phase differences and aluminum plate with diameter of (a) 180 mm, (b) 120 mm, and (c) 75 mm is located. Here, the distance between the plate's center and the side-by-side placed coils' midpoint is 37.5 mm on a constant horizontal plane. In subfigures (a) and (b), labels S0 and S180 correspond to the systems in which squircle coils are driven with the 0° and 180° phase differences, respectively. Similarly, C0 and C180 represent the systems where circular coils are driven with the 0° and 180° phase differences. In subfigure (c), on the other hand, labels circular and squircle represent the systems in which single circular and single squircle coil is driven.

Table A.12: Calculated power transferred to the plate (P_{plate}) and increase in the system's equivalent resistance due to plate's loading (R_{plate}) for systems with aluminum plate having 180 mm, 120 mm and 75 mm diameters and being located 20 mm, 14 mm and 5 mm above the coils. Here, the distance between the plate's center and the side-by-side placed coils' midpoint is 37.5 mm on a constant horizontal plane.

Plate Diameter (mm)	Plate-Coil Distance (mm)	Phase Difference ($^\circ C$)	Outer Squircle-Inner Circular		Circular	
			P_{plate} (W)	R_{plate} (Ω)	P_{plate} (W)	R_{plate} (Ω)
180 [Figure A.12(a)]	20	0	0.7307	0.1169	0.6389	0.1022
		180	**0.8162**	**0.1306**	0.7005	0.1121
	14	0	1.334	0.213	1.251	0.200
		180	**1.544**	**0.247**	1.386	0.222
	5	0	4.034	0.645	4.195	0.671
		180	**4.511**	**0.722**	4.439	0.710
120 [Figure A.12(b)]	20	0	0.4044	0.0647	0.3247	0.0520
		180	**0.4732**	**0.0757**	0.3825	0.0612
	14	0	0.6907	0.1105	0.6058	0.0969
		180	**0.8652**	**0.1384**	0.7279	0.1165
	5	0	2.088	0.334	2.073	0.332
		180	**2.470**	**0.395**	2.258	0.361
75 [Figure A.12(c)]	20	X	**0.5104**	**0.0817**	0.4069	0.0651
	14	X	**0.9151**	**0.1464**	0.7433	0.1189
	5	X	**2.537**	**0.406**	2.086	0.334

It is seen that in all the cases, where the distances between the plate's center and the side-by-side placed coils' midpoint are 0 mm, 12.5 mm, 25 mm, and 37.5 mm on a constant horizontal plane, the highest power transfer (and the corresponding resistance enhancement) values are achieved in systems where the proposed outer squircle-inner circular coils are driven with the 180° phase difference.